Strangeness Production in Selected Proton-Induced Processes at COSY-ANKE

by

Qiujian Ye

Department of Physics
Duke University

Date: _____

Approved:

_____
Haiyan Gao, Supervisor

_____
Steffen A. Bass

_____
Albert Chang

_____
Mark C. Kruse

_____
Kate Scholberg

Dissertation submitted in partial fulfillment of the requirements for the degree of
Doctor of Philosophy in the Department of Physics
in the Graduate School of Duke University
2013

Abstract

Strangeness Production in Selected Proton-Induced Processes at COSY-ANKE

by

Qiujian Ye

Department of Physics
Duke University

Date: _____

Approved:

_____
Haiyan Gao, Supervisor

_____
Steffen A. Bass

_____
Albert Chang

_____
Mark C. Kruse

_____
Kate Scholberg

An abstract of a dissertation submitted in partial fulfillment of the requirements for the degree of Doctor of Philosophy in the Department of Physics in the Graduate School of Duke University
2013

Abstract

In recent years, the strangeness production reactions in NN collisions have attracted a considerable amount of interest. These reactions are expected to provide valuable information on the manifestation of Quantum chromodynamics (QCD) in the non-perturbative region. For example, the ϕ meson is expected to probe the admixture of $s\bar{s}$ quark pairs in the nucleon wave function. The near-threshold reactions are expected to provide valuable information about the meson-meson, meson-baryon, and hyperon-nucleon interactions.

We report the differential and total cross sections for the $pp \rightarrow ppK^+K^-/\phi$ reaction at T_p= 2.567 (below the ϕ meson threshold) and 2.83 GeV (above the ϕ meson threshold). We use detailed model descriptions to fit a variety of one-dimensional distributions in order to separate the $pp \rightarrow pp\phi$ cross section from that of non-ϕ production. The differential spectra show that higher partial waves represent the majority of the $pp \rightarrow pp\phi$ total cross section at an excess energy of 76 MeV, whose energy dependence would then seem to require some s-wave ϕp enhancement near threshold. On the other hand, strong preferences to the low Kp and Kpp invariant masses are observed in non-ϕ kaon pair productions. The cusp effect in the K^+K^- distribution at the $K^0\bar{K}^0$ threshold is clear and some evidence is also found for coupling between the K^-p and $\bar{K}^0n$ channels. Beside of the mentioned reactions, we also show the preliminary results for the search for a possible K^-pp bound state in the $pp \rightarrow pK^+\Lambda$ reaction at Tp =2.567 GeV.

To my parents and Jian Chen

Contents

List of Tables

List of Figures

List of Abbreviations and Symbols

QCD	Quantum Chromodynamics
χPT	Chiral Perturbation Theory
ANKE	Apparatus for Studies of Nucleon and Kaon Ejectiles
COSY	COoler SYncrotron
OZI	Okubo-Zweig-Iizuka
Pd	Positive detector
Nd	Negative detector
Fd	Forward detector
TOF	time of flight
MWPC	Multi-wire proportional chambers
FSI	final state interaction
DAQ	Data acquisition system
TDC	time to digital
CFD	constant fraction discriminators

Acknowledgements

This thesis could never have been completed without the help of many people. I would like to express my deepest gratitude to all of them.

The first person I have to thank is my advisor, Prof. Haiyan Gao, for her excellent guidance, support, patience, and providing me with many opportunities. She always encouraged me to not only grow as a physicist sitting in front of the computer but also as an physicist working in the lab. I am truly and deeply impressed by her enthusiasm and insights in physics. I really appreciate that she always replied to my emails immediately in late nights.

I also want to thank all the members in our group, especially George, who as a good friend, was always willing to help and give his best suggestions. Many thanks also go to other group members. They always lend a hand when I need help.

I really enjoyed working with many people at ANKE. I would like to thank all the members of the ANKE collaboration: Prof. Dr. H. Stroher for providing the possibility to work at COSY-ANKE; Dr. M. Hartmann for helping setting up almost everything, spending a lot of time for valuable discussions with data analysis, and explaining to me everything related to ANKE; Prof. C. Wilkin for a lot of proof reading and correcting my writing and valuable advice in physical topics; Dr. S. Dymov for the analysis codes and useful discussions of the Forward detection, and Dr. D. Chiladze for discussions of luminosity determinations. I also want to thank my friends Dr. H. Xu, B. Gou and X. Kan for their support of my living in Germany.

Finally, I would also like to thank my family and my wife for their endless support and inspiration.

1

Introduction

1.1 Strong interaction

Quantum Chromodynamics (QCD), as the well-accepted theory of strong interactions, provides very accurate predictions in the high energy region where perturbative calculations can be carried out, and well tested by experiments. However, at low energy the coupling constant becomes larger, and perturbative calculations no longer work. The fact that particles with isolated strong charge (color) have never been observed is just one prominent example of the non-perturbative character of QCD at low energy. Furthermore, our inability to solve QCD Lagrangian analytically making the study of this (non perturbative) region particularly important and challenging. A promising description of the QCD in this region could be achieved through lattice QCD that provides the most promising approach for the theoretical predictions of the properties of hadrons. However, lattice QCD calculations are still far from being amiable to solutions for low and intermediate energy scattering reactions. On the other hand, methods like effective field theories (i.e. Chiral Perturbation Theory χPT) employing effective degrees of freedom have had tremendous success in describing the non-perturbative processes. For instance, baryons such as

proton are considered to consist of three quarks, and mesons to consist of a quark and an anti-quark pair. Furthermore, it is more practical to consider the interactions between hadrons (baryons and mesons) rather than quarks and gluons in the non-perturbative regime.

Experimental data of high quality and precision on hadronic processes at low and intermediate momenta are necessary in order to verify the systematic low energy expansion of the χPT, which has already enforced an important insight into the structure and dynamics of nucleons and mesons in the non-perturbative regime. Therefore it is very important to know the properties of the mesons, their structure and interactions in the hadronic environment. Although a large amount of data are available from measurements with electromagnetic probes, there are still many things to learn about the physics with hadronic probes at intermediate energies, i.e. the investigation of production, decay, and interaction of hadrons. An important class of experiments in this context is related to meson production in nucleon-nucleon and nucleon-nucleus collisions close to the production thresholds.

1.2 Strangeness production close to threshold

The study of near threshold meson production in NN collision has several features. Firstly, the theoretical descriptions of such reactions are simplified since a very limited part of the phase space is available for the reaction products and, hence, only a few partial waves contribute to the observables. Additionally, it is difficult to study the unstable particle final state interactions with nucleons due to the lack of such beams in nature. However, because of the low relative momentum between final particles, meson production close to threshold in nucleon-nucleon collisions offers an excellent tool to study meson-meson and baryon-meson interactions. One prominent example is the investigation of the hyperon-nucleon interaction in the reaction $pp \to pYK$, where Y denotes a hyperon (Λ, Σ etc.) and K represents a kaon.

From the invariant mass distributions of the YN system, information about the on-shell YN interaction can be extracted. Another example is the ϕ meson production, which provides valuable information about ϕN interactions and the existence of a possible ϕN bound state. Furthermore, the near threshold nucleon-nucleon and nucleon-nucleus collisions also allow for studies of particular resonances. One example is the $N^\star(1535)$ resonance, which couples strongly to the ηN channel. But a large $N^\star(1535)K\Lambda$ coupling has also been deduced from γp and pp reactions [1]. Moreover, recent theoretical calculation [1] shows that the $N^\star(1535)$ also has a significant coupling to the ϕN channel.

The study of strangeness production reactions in NN collisions is expected to provide valuable information on the manifestation of QCD in the non-perturbative regime. The ϕ meson is expected to probe the admixture of $s\bar{s}$ quark pairs in the nucleon wave function [2] and provide information on the interaction of strange quarks with the surrounding non-perturbative environment. Furthermore, the enhancement in the strangeness production has been proposed as a signature for the formation of the quark-gluon plasma in high energy nucleus-nucleus collisions [3, 4].

1.3 Overview

The proton-proton and proton-nucleus data presented in this thesis consists of part of the experimental programs of the ANKE (Apparatus for Studies of Nucleon and Kaon Ejectiles) Collaboration at COoler-SYncrotron (COSY) at Forschungszentrum Jülich. The details of the selected channels in pp collisions are presented in Table. 1.1.

A search for a possible ϕN bound state in proton-nucleus reaction with different targets C, Cu, Ag, Au at $T_p = 2.83$ GeV is also discussed. This thesis is organized as follows:

The basic properties of strange hadrons and physics motivations for the reaction channels are discussed in Chapter. 2. In this chapter existing theoretical models and

Table 1.1: The selected strangeness productions in pp collisions. The $\phi(1020)$ meson was identified via the decay channel $\phi \to K^+K^-$, and Λ was detected by $\Lambda \to p\pi^-$ channel.

Reaction Channel	Beam Energy GeV
$pp \to pp\phi$	$T_p = 2.83$
$pp \to ppK^+K^-$	$T_p = 2.57, 2.83$
$pp \to pK^+\Lambda$	$T_p = 2.57, 2.83$

experimental data are presented. The experimental apparatus of COSY-ANKE is discussed in Chapter. 3. The main features of the apparatus including the COSY accelerator, the ANKE magnetic spectrometer and the target are described in great details. In Chapter. 4 the main procedures of data analysis such as event reconstruction, particle identifications, detection efficiency corrections and luminosity determinations are presented, followed by the detector acceptance corrections based on different parameterizations for different reactions. Chapter. 6 presents the experimental results and discussions. The total and differential cross section results are presented separately. Finally, the results are summarized in Chapter. 7, which also contains an outlook for future experiments and theoretical calculations.

2

Physics motivations

2.1 Quark Model

With the discovery of the kaons in cosmic rays in 1947, a new class of particles was found. Due to their unusual properties, these hadrons were initially named strange particles. In 1964, Gell-Mann and Zweig proposed that all hadrons, particles interacting with strong forces, are built out of elementary objects with a spin value of $\frac{1}{2}$ (called quarks). Quarks are proposed to have both electric and color charges, which are responsible for the electromagnetic and strong interactions, respectively. Later, the heavy quarks c, b, t were discovered and included in the quark model. Within this model, hadrons consist of either three quarks (baryons) or a quark-antiquark pair (mesons). In low energy, hadrons are combinations of the two lightest quarks u, d or their anti-particles $\bar{u}$, $\bar{d}$. With increasing energy, quark-antiquark pairs of the next heavier flavor s are produced, thus generating the so-called strange hadrons that include one or more s or $\bar{s}$ quark. In the quark model, the lightest mesons are formed from the quark triplet u, d, s (the SU(3) flavor symmetry nonet). The nonets categorize the various quark-antiquark combinations in a relative S wave state (i.e.

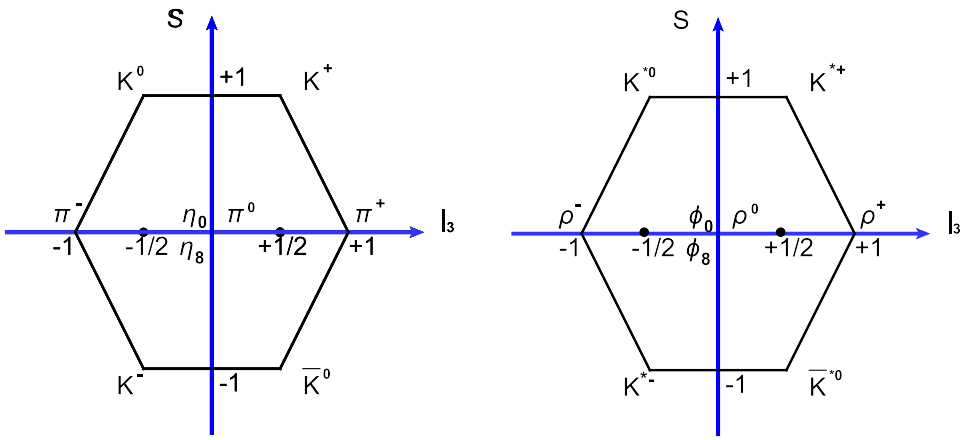

FIGURE 2.1: Strangeness S versus isospin I_3 for the pseudo-scalar (left) and vector (right) meson nonets [5].

Table 2.1: Flavor wave function and quantum numbers of the ground state pseudo-scalar ($J^P = 0^-$) and vector ($J^P = 1^-$) meson nonets [5].

Flavor Wave Function	I	I_3	S	$J^P = 0^-$	$J^P = 1^-$
$\|u\bar{d}>$	1	+1	0	π^+	ρ^+
$\|\bar{u}d>$	1	-1	0	π^-	ρ^-
$1/\sqrt{2}(\|u\bar{u}> - \|d\bar{d}>)$	1	0	0	π^0	ρ^0
$\|u\bar{s}>$	1/2	+1/2	+1	K^+	$K^{\star+}$
$\|\bar{u}s>$	1/2	-1/2	-1	K^-	$K^{\star-}$
$\|d\bar{s}>$	1/2	-1/2	+1	K^0	$K^{\star0}$
$\|\bar{d}s>$	1/2	+1/2	-1	$\bar{K}^0$	$\bar{K}^{\star0}$
$1/\sqrt{6}(\|u\bar{u}> + \|d\bar{d}> - 2\|s\bar{s}>)$	0	0	0	η_8	ϕ_8
$1/\sqrt{3}(\|u\bar{u}> + \|d\bar{d}> + \|s\bar{s}>)$	0	0	0	η_0	ϕ_0

$L = 0$) with either parallel or anti-parallel spins, coupling to total angular momenta $J = 0, 1$, respectively. The parity of these states is given by $P = (+1)(-1)(-1)^l$, and all these states are characterized by either $J^P = 0^-$ (pseudo-scalar meson nonet) or $J^P = 1^-$ (vector meson nonet). The pseudo-scalar and vector meson nonets are plotted in Fig. 2.1 as a function of the strangeness quantum number S and the z component of the isospin I_3. The corresponding flavor wave functions of the pseudo-scalar and vector meson nonets are summarized in Tab. 2.1. The physically observed vector mesons ϕ and ω are linear combinations of the singlet ϕ_0 and octet ϕ_8 states,

which have the same isospin and the hypercharge ($Y = B + S$, where B represents the baryon number) quantum numbers.

$$\begin{pmatrix} \omega \\ \phi \end{pmatrix} = \begin{pmatrix} cos\theta_v & sin\theta_v \\ sin\theta_v & -cos\theta_v \end{pmatrix} \begin{pmatrix} \phi_0 \\ \phi_8 \end{pmatrix} \tag{2.1}$$

where θ_v is the mixing angle. For ideal mixing, the mixing angle would be $\theta_v^{ideal} \approx 35^\circ$ ($sin\theta_v^{ideal} = \sqrt{1/3}$), and the corresponding ϕ and ω ideal mixing states are:

$$\phi = |s\bar{s}>, \omega = \frac{1}{2}(|u\bar{u}> + |d\bar{d}>) \tag{2.2}$$

If $\theta_v = \theta_v^{ideal}$, the ϕ meson must consist of only strange quarks and the ω meson only u, d quarks and their antiquarks. Therefore according to Okubo-Zweig-Iizuka (OZI) rule [6, 7, 8, 9] (see sec.2.2), the decay channel $\phi \to \pi^+\pi^-\pi^\circ$ should be strongly suppressed. However, using a Gell-Maan-Okubo empirical mass formula [10, 11, 12], one can determine the value of $\theta_v = 39^\circ$. This value is also in good agreement with the results from ϕ and ω radiative decay [5, 13], which means the ϕ meson is not a purely $s\bar{s}$ state. The deviation from the ideal mixing angle $\delta = \theta_v - \theta_v^{ideal}$ determines the corresponding contribution of light quarks (u, d) in the ϕ wave function:

$$\phi = cos\delta|s\bar{s}> - sin\delta|q\bar{q}> \tag{2.3}$$

where $|q\bar{q}> = 1/\sqrt{2}(u\bar{u} + d\bar{d})$. With such a small deviation δ from ideal mixing, one is able to explain the branching ratio for the decay of ϕ and ω mesons [5]:

$$\begin{array}{llll} \phi \to K^+K^- & 49\% & \omega \to \pi^+\pi^-\pi^0 & 90\% \\ \to K^\circ\bar{K}^\circ & 34\% & \to \pi^+\pi^- & 1.7\% \\ \to \pi^+\pi^-\pi^0 & 15\% & \to \pi^\circ\gamma & 8.9\% \end{array} \tag{2.4}$$

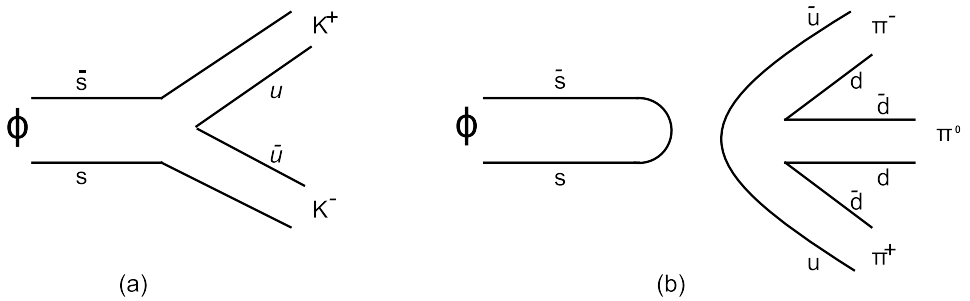

FIGURE 2.2: (a) ϕ meson decays into two kaons. (b) ϕ meson decays into three pions.

2.2 ϕ meson production

2.2.1 Motivations

As mentioned already, the decay channel of ϕ meson into non-strange mesons (i.e. $\phi \rightarrow \pi^+\pi^-\pi^\circ$) is suppressed compared to that of strange final states. This can be explained by the OZI rule, which states that processes with disconnected quark lines in the initial and final state are suppressed. This rule is based on the assumption that such processes proceed via a multi-gluon intermediate state. Suppression of the decays to three pions is due to that they require the $s\bar{s}$ pair to annihilate first into high energy gluons, which must be energetic enough to produce the decay products; then the gluons couple to several $q\bar{q}$ pairs as the quarks (u, d) of the final state mesons; However, at high energy the coupling of the gluons to quarks is weak (the QCD asymptotic freedom), therefore such decays are suppressed. While decays of the ϕ meson into kaons are the OZI rule allowed processes, since all the initial state quarks exist also in the final states. In addition, due to the fact that mass of the ϕ meson is very close to that of a K^+K^- pair, all virtual gluons are of low momentum and strongly couple to the final states. The exchange of gluons between hadrons, which plays a substantial role at high energy interactions, is harder to study at low energies because diagrams including quark exchange play a more important role [14]. However, ϕ meson being a nearly pure $s\bar{s}$ state is considered as

a great tool to study gluon exchanges. According to the OZI rule: quark exchanges in the reaction between ϕ meson with ordinary (non-strange) baryonic matter are suppressed [15] because there are no common quarks between the particles. The multigluon exchange is therefore expected to dominate ϕN scattering at all energies. It has been suggested [16] that the QCD van der Waals interaction, mediated by multi-gluon exchanges, is strong enough to form a nuclear bound state of η_c with ^3He. Similarly, one can expect that the attractive QCD van der Waals force also dominates the ϕN interaction. Hence, a bound state of ϕN is also possible [15]. Using the variational method and a non-relativistic Yukawa type attractive potential $V_{(s,\bar{s}),N} = -\alpha e^{\mu r}/r$, Gao, Lee and Marinov [15] find that a bound state of ϕ-N with a binding energy of about 1.8 MeV is possible. Such a bound state was also predicted by Huang, Zhang, and Yu [17] using a chiral SU(3) quark model and the extended chiral SU(3) quark model solving the Resonating Group Method (RGM) equation. The model parameters used by the authors in [17] provided good descriptions of baryon bound states, the deuteron binding energy and NN scattering phases shifts [18, 19]. Sub-threshold production kinematics have also been proposed as being advantageous for the search of ϕN bound states in γA and pA reactions [15, 20]. In order to have a reliable prediction of the possible formation of a bound state in the ϕN system, information about the ϕN interaction is crucial and important.

However, direct measurement of the ϕN reaction is not possible due to the lack of a ϕ meson beam. Up to now, most of the total cross sections $\sigma_{\phi N}$ are extracted from photo-production experiments. An upper limit of $\sigma_{\phi N} \approx 11$ mb [21, 22] is obtained using the ϕ photo-production data on the proton and a vector meson dominance (VMD) model, which is in agreement with the estimate from the additive quark model [23]. However, a large in-medium ϕN absorption cross section of about 35 mb was inferred by the LEPS collaboration [24] from measurements of K^+K^- pairs photoproduced on Li, C, Al and Cu targets at SPring-8. This large ϕN cross

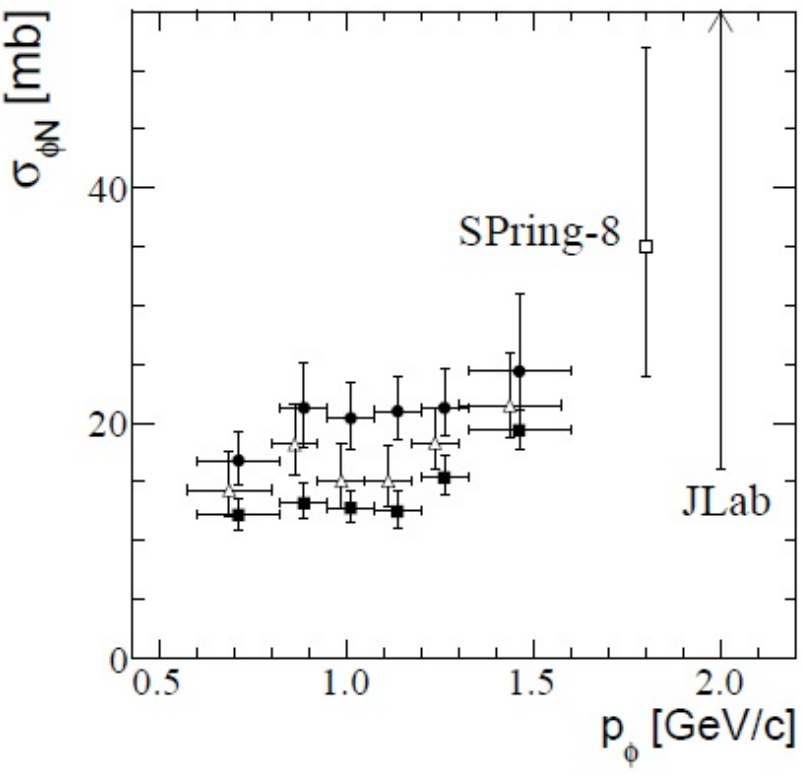

FIGURE 2.3: The ϕN absorption cross section measured from nuclei targets at ANKE [25], SPring-8 [24] and JLab [26]. The full squares, full circles and open triangles are model-dependent cross section extracted from ANKE data [25].

section was also confirmed by Boltzmann-Uehling-Uhlenbeck (BUU) transport model calculations [28], which are based on binary collisions and the propagation of particles in a self-consistent mean eld. Recently, values of the in-medium $\sigma_{\phi N}$ were also determined by the CLAS collaboration [26] from transparency ratio measurements at JLab. In this experiment, the photo-productions of the ϕ meson on H, C, Ti, Fe, Pb targets were measured via e^+e^- decay mode. Using a Glauber model, values of $\sigma_{\phi N}$ in the range of 16-70 mb were extracted. In addition, the JLab measurements of coherent [14] and incoherent ϕ meson [29] photo-production from deuterium suggest that $\sigma_{\phi N} > 20$ mb. On the other hand, the ϕ mesons productions in proton collisions with C, Cu, Ag and Au targets have been studied via the $\phi \rightarrow K^+K^-$ decay at

ANKE [25]. An effective ϕN absorption cross section in the range of 14-21 mb has been extracted, which is consistent with these measurements from photo-production, as shown in Fig. 2.3. The models [30, 31, 32] used are sensitive to the relative strength of ϕ production in pp and pn collisions. The sizable excesses in the ϕN cross section might suggest some enhancements in the ϕN systems or even a possible ϕN bound state.

In order to study such enhancements in ϕN cross sections and search for a possible ϕN bound state in the sub-threshold pA reaction, one should have a full understanding of the near threshold ϕ meson production in pp collisions. Here, the threshold is defined when the lowest available energy in the center of mass system is sufficient to create the final state particles. It is more convenient to use the notation of the excess energy ε, defined as:

$$\varepsilon = \sqrt{s} - (2m_p + m_\phi), \tag{2.5}$$

where $\sqrt{s}$ is the total center-of-mass energy, m_p and m_ϕ are the proton and ϕ meson mass, respectively.

Moreover, the study of the near threshold meson production can help us gain insight about the strong interaction physics [33, 34, 35]. For instance, near threshold heavy meson productions in nucleon-nucleon collisions are sensitive to interactions of nucleons at short distances [34]. When the momenta of the nucleons in the entrance channel are large but the momenta of the final state particles are small (they are almost at rest near threshold), the process results in large momentum transfer at short distance. For example, the $NN \to NN\phi$ reaction at its threshold energy probes distances between the two colliding nucleons of about 0.2 fm [36, 37]. This distance corresponds to the overlapping region of the two interacting nucleons, in contrast to the distance of about 0.5 fm probed by much lighter pion production (see [36] and references therein). The analysis of such data in the short-range limit permits a

quantitative comparison of productions leading to two- and three-body final states and provides relevant information for testing QCD-based NN interactions.

On the other hand, the near threshold ϕ meson production is crucial to address the question of whether there is a non-negligible amount of strange quarks in the proton flavor wave function, because the ϕ meson is considered to mainly consist of strange quarks with a rather small amount of the light quarks u, d. Under the assumption that the OZI rule is exactly fulfilled, the production of the ϕ meson is expected to be strongly suppressed (compare to that of the ω meson) in hadronic reactions and the ratio of the production cross sections for the ϕ and ω mesons was calculated as [38, 39]:

$$R_{\phi/\omega} = \frac{g^2_{\phi\rho\pi}}{g^2_{\omega\rho\pi}} = \frac{\sigma(A+B \to \phi X)}{\sigma(A+B \to \omega X)} = f \times tan^2(\delta) = f \times 4.2 \cdot 10^{-3} \qquad (2.6)$$

where f is the correction factor for the available phase space for ϕ and ω production, and $\delta \sim 3.7^\circ$ is the deviation from the ideal mixing angle. Since the OZI rule has been well-tested in many experiments, a significantly higher value of $R_{\phi/\omega}$ than estimated from the OZI rule may indicate a large amount of hidden strangeness inside the nucleon [40, 41].

Indeed, measurements on antiproton-proton ($p\bar{p}$) annihilation at CERN [42] show that the ratios of $\sigma(p\bar{p} \to \phi X)/\sigma(p\bar{p} \to \omega X)$ exceed the estimate from the OZI rule by more than one order of magnitude. These observed large ϕ production cross sections were interpreted as hints for an intrinsic $s\bar{s}$ component inside the proton. However, the data can also be explained by the strong re-scattering effects in the final state without any strangeness content of nucleon [43, 44]. Here it is important to find the possible OZI violations in other reactions. Further investigations show that strong violations of the OZI rule were also observed in the reactions $pd \to {}^3He\phi$ [45, 46], $pp \to pp\phi$ [47, 48] and $\pi p \to \phi\pi p$ [49]. The discrepancy with the OZI rule in these

reactions was found by a factor of 10-100. Moreover, a very recent analysis of ϕ and ω photoproduction from the proton shows that the ratio $R_{\phi/\omega}$ is 0.8 ± 0.2 at photon energies above 30 GeV [50]. These observations in the γp, $p\bar{p}$ and πN reactions provide a strong motivation to further search for substantial OZI rule violations at low energies. The DISTO Collaboration reported the first near threshold $pp \to ppV$ measurement at $T_p = 2.85$ GeV also indicating a substantial OZI violation [47]. Later, the ANKE collaboration found the violation of OZI rule and the $R_{\phi/\omega}$ is about eight times larger than the OZI predication at $T_p = 2.65, 2.70$ and 2.83 GeV (only data at $T_p = 2.65$ GeV has high statistics) [48]. It is interesting that DISTO has observed also the differences between the angular distributions of the ϕ and ω mesons produced. This may contradict to the OZI rule postulate that the ϕ could be formed in pp interactions only via $\omega - \phi$ mixing, and indicates that the difference in the ϕ and ω meson production might be due to the difference in the production mechanisms instead of kinematics. Moreover, the analysis of the near threshold data suggest that the $pp \to pp\phi$ amplitude exhibits a significantly stronger variation with energy than that of the ω production. This characteristic energy dependence could be a sign for additional reaction mechanisms in the ϕ production reaction, and especially it might be caused by the excitation of a resonance or bound state in the ϕp system [51]. Clearly future measurements should take data at different energies above the production threshold of the ϕ and ω mesons for further investigations.

2.2.2 Models

Various theoretical models have been developed to describe the experimental data of the $NN \to NN\phi$ reaction. Sibirtsev *et al.* [52] have studied the ϕ meson production in NN collisions within the framework of a one-pion exchange model. In this model, the reaction is treated as the emission of a virtual pion from one nucleon with the subsequent reaction $\pi N \to \phi N$ on the other nucleon. This calculation entails a

folding of the pion propagator in free space with the pion form factor to account for off shell modifications of the vertex as well as a parameterization of the cross section for the reaction $\pi N \to \phi N$. Furthermore, the coupling constant $f_{\pi NN}$ as well as a cut-off parameter $\Lambda = 1$ GeV are required. The results of these calculations, which describe the higher energy data well, have been fit using the following parameterization:

$$\sigma(pp \to pp\phi) = a(1 - \frac{s_0}{s})^b(\frac{s_0}{s})^c, \tag{2.7}$$

where the threshold energy squared $s_0 = 8.38$ GeV^2, and the parameters are given as $a = 0.06$ mb, $b = 2.24$ and $c = 2.7$ [52]. However, these calculations that have an energy dependence similar to a phase-space predication, underestimate the low energy data point [47, 48] by about a factor of three. Furthermore, the improved calculation [53], which includes the S-wave proton-proton final state interaction (FSI), results in significant rises of the near threshold total cross sections.

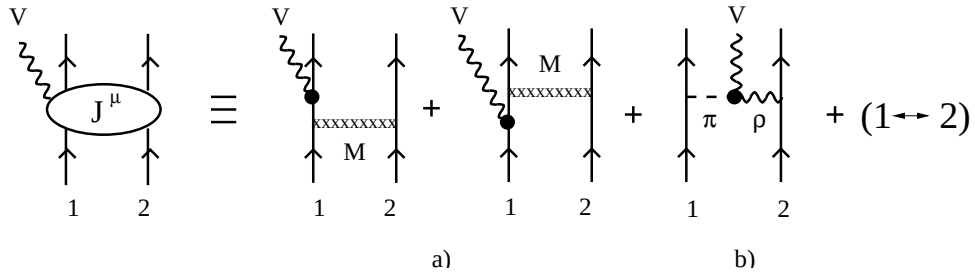

FIGURE 2.4: Vector meson (ω or ϕ) production currents, J^μ, included in the present studies [27, 55]: a) nucleonic current, b) mesonic exchange current. $V = \omega$ or ϕ and M $= \pi, \eta, \rho, \omega, \sigma, a_0(= \delta)$.

The calculations described above are based on the premise that the reaction is completely dominated by pion exchanges. Another approach proposed by Nakayama *et al.* [27, 36] explicitly includes not only the mesonic current due to the $\pi\rho \to \phi$ coupling, but also the nucleonic current, as shown in Fig. 2.4. For the nucleonic current, the exchange of the following mesons has been considered: $\pi, \eta, \rho, \omega, \sigma, a_0$. The calculations use a relativistic effective Lagrangian at the hadronic level. The

reaction amplitude is calculated within the distorted wave with Born approximation [54], including both the initial and final pp interactions. Although the nucleonic current is expected to be suppressed relative to the mesonic current, the relative magnitude of the contributions can not be determined from the total cross section data alone. However, they claimed that the angular distribution of the produced ϕ meson in the c.m. frame provides a clear signature to disentangle these two reaction mechanisms. Within this model the observed angular distribution, which is nearly isotropic, indicates a dominance of the mesonic current in contrast to the $cos^2\theta$ distribution expected for the nuclenoic current. As a result, measurements of this observable can yield valuable information on the magnitude of the nucleonic current and, specifically, on the $NN\phi$ coupling constant. Further calculations show that the strength of the $NN\phi$ coupling constant is directly associated with the amount of hidden strangeness inside the nucleon [36].

Within a similar approach by Titov *et al.* [55], they have calculated total cross sections as well as the beam-target asymmetry. Their results show that the total cross section is dominated by the $\pi\rho \rightarrow \phi$ process and not sensitive to a small amount of admixture of $s\bar{s}$ in the nucleon's flavor wave function. For example, a 1% admixture of $s\bar{s}$ results in a two orders of magnitude smaller contribution to the total cross section than the meson exchange process. Without including the $s\bar{s}$ in the nucleon wave function, they predict the total cross section ratio $\sigma(pn \rightarrow pn\phi)/\sigma(pp \rightarrow pp\phi) \approx 5$. This is in strong contrast to the intrinsic strangeness model proposed by Ellis *et al.* [56], in which the ratio is given as $\frac{1}{4}$. Experimental data are required to distinguish between these models. The beam-target asymmetry (C_{zz}^{BT}) has also been analyzed with this model. It is further claimed that the elements of the decay density matrix are $\rho_{00} = 0, \rho_{\pm1\pm1} = 1/2$ [57]. Furthermore, the results show that a 5% admixture of $s\bar{s}$ modifies the density matrix to $\rho_{00} = 0.22, \rho_{\pm1\pm1} = 0.39$. The elements of the density matrix are extracted directly from the decay angular distribution of the ϕ

meson, and thus can be useful to help determine the intrinsic strangeness in the nucleon.

The models described above are based on one-boson-exchange (OBE) model, they did not consider the possibility of nucleon resonances. Faessler *et al.* [58] claim that nucleon resonances become important at high energies, and thus propose a resonance model to describe the ϕ meson production in pp collisions. In their model, the ϕ meson is produced by a two-step reaction: the excitation of nucleon resonances and their subsequent decay $pp \rightarrow pR \rightarrow pp\phi$. The calculations show that the ϕ meson data can be explained by the dominance of $N^*(2090)\frac{1}{2}^-$. Another calculation from [1] shows that the total and differential cross sections can be reproduced with the $N^*(1535)$ resonance. Within the resonance model, the production mechanism is due to the excitation of the sub-$N\phi$ threshold $N^*(1535)$ resonance following $\pi^0-, \eta-$ and ρ^0- meson exchanges between two protons [59, 27, 60]. The significant coupling of the $N^*(1535)$ resonance to ϕN is compatible with previous indications (see Ref. [1] and reference therein) of a large $s\bar{s}$ component in the quark wave function of the $N^*(1535)$ resonance which may explain the significant enhancement of the ratio R_ϕ/R_ω.

2.2.3 Partial waves and selection rules

Since in the near threshold region only a few partial waves would contribute to the final states, which makes the reactions easier to treat in theory. In a non-relativistic approximation, the total cross section for the ϕ meson production in nucleon-nucleon collisions can be written as [34]:

$$\sigma \propto \int_0^{q_{max}} kq^2 |M_{NN\rightarrow NN\phi}|^2 dq, \tag{2.8}$$

where q is the momentum of the ϕ meson in the center-of-mass (c.m.) frame, and k the momentum of either nucleon in the rest frame of the nucleon-nucleon system. Here we denote that L and l as the relative angular momentum of the nucleon-nucleon pair and the ϕ meson relative to the NN system, respectively. Assuming that the final state particles are non-interacting so that they can be described by non-distorted plane waves, whose radial parts $\psi_l(q,r)$ are given by the spherical Bessel functions:

$$\psi_l(q,r) \propto j_l(qr) \overset{qr\to 0}{\to} \frac{(qr)^l}{(2l+1)!}, \tag{2.9}$$

An expansion of the transition amplitude $|M_{Ll}|^2$ around $qr = 0$ leads to $|M_{Ll}|^2 \propto q^{2l}k^{2L}$. Furthermore, assuming that the production amplitudes are constant, one can calculate the partial cross section by integrating this matrix element:

$$\sigma_{Ll} \propto q_{max}^{2L+2l+4} \propto \eta_\phi^{2L+2l+4} \tag{2.10}$$

where $\eta_\phi = q_{max}/m_\phi$ (m_ϕ is the mass of the ϕ meson) [34]. Based on Eq. 2.10, at threshold the total cross section for the $NN \to NN\phi$ reaction with respect to the energy should display a η_ϕ^4 distribution. The dimensionless parameter η_ϕ can be used to estimate the classically calculated maximum angular momentum of the ϕ meson in the c.m. system, and therefore the partial waves involved in the final state. The similar argument can be also found in the work of Gell-Mann and Watson [61].

The selection rules for nucleon-nucleon induced meson production can be calculated from the symmetries of strong interactions that imply the conservation of parity, total angular momentum and isospin [33]. According to Pauli Principle, a two nucleon is required to have anti-symmetric total wave function and

$$(-1)^{L+S+T} = (-1), \tag{2.11}$$

where L, S and T represent the orbital angular momentum, total spin and total isospin of the two nucleon system, respectively. In the case of a proton-proton system, $T = 1$, $L + S$ should be even. In addition, according to parity conservation we have $(-1)^L = \pi_\phi(-1)^{L'+l'}$, where π_ϕ is the intrinsic parity of the ϕ meson and L, L' and l' are the orbital angular momentum of the incoming nucleon-nucleon system, the outgoing nucleon-nucleon system and the produced ϕ meson with respect to the nucleon-nucleon system, respectively. Combined these two criteria, one can obtain $(-1)^{\Delta S+\Delta T} = \pi_\phi(-1)^{l'}$, where ΔS (ΔT) represents the change in total spin (isospin) between the initial NN and the final NN system. There is no change in the total isospin for the $pp \to pp\phi$ reaction due to the fact that the nucleons are the same in the final state as the initial state. This in combination with the intrinsic parity of ϕ meson gives:

$$(-1)^{\Delta S} = (-1)^{1+l'}, \tag{2.12}$$

The near-threshold regime is dominated by the lowest partial waves which in this case would be $l' = 0$ and $L' = 0$. Based on Eq. 2.11 and Eq. 2.12, the only possible transition is ${}^3P_1 \to Ss$ for the $pp \to pp\phi$ reaction. Here the final state is denoted as Ss (the first one represents the orbital angular momentum of NN system, the other is the orbital angular momentum of the ϕ meson with respect to NN system). For further discussions, we have also listed partial waves that are allowed in the near threshold regime for the $pp \to pp\phi$ reaction in Table. 2.2. In the Table, the spectroscopic notation ${}^{2S+1}L_J$ holds for the partial waves in the initial state and ${}^{2S+1}L_J l_\phi$ for the final states.

2.2.4 Kinematics and observables

The corresponding cross section for the ϕ meson production in the reaction $a + b \to c + d + \phi$, where a, b and c, d label the incoming and outgoing nucleons, is related

Table 2.2: List of allowed partial waves for the $pp \to pp\phi$ reaction. The notation is defined in the text [62].

Type	$^{2S+1}L_J \to {}^{2S+1}L_J l_\phi$
Ss	$^3\mathrm{P}_1 \to {}^1\mathrm{S}_0\,\mathrm{s}$
Sp	$^1\mathrm{S}_0 \to {}^1\mathrm{S}_0\,\mathrm{p}$
	$^1\mathrm{D}_2 \to {}^1\mathrm{S}_0\,\mathrm{p}$
Ps	$^1\mathrm{S}_0 \to {}^3\mathrm{P}_1\,\mathrm{s}$
	$^1\mathrm{D}_2 \to {}^3\mathrm{P}_1\,\mathrm{s}$
	$^1\mathrm{D}_2 \to {}^3\mathrm{P}_2\,\mathrm{s}$
Sd	$^3\mathrm{P}_2 \to {}^1\mathrm{S}_0\,\mathrm{d}$
	$^3\mathrm{F}_2 \to {}^1\mathrm{S}_0\,\mathrm{d}$
	$^3\mathrm{F}_3 \to {}^1\mathrm{S}_0\,\mathrm{d}$
Pp	$^3\mathrm{P}_0 \to {}^3\mathrm{P}_{0,1,2}\,\mathrm{p}$
	$^3\mathrm{P}_1 \to {}^3\mathrm{P}_{0,1,2}\,\mathrm{p}$
	$^3\mathrm{P}_2 \to {}^3\mathrm{P}_{0,1,2}\,\mathrm{p}$
	$^3\mathrm{F}_2 \to {}^3\mathrm{P}_{0,1,2}\,\mathrm{p}$
	$^3\mathrm{F}_3 \to {}^3\mathrm{P}_{1,2}\,\mathrm{p}$
	$^3\mathrm{F}_4 \to {}^3\mathrm{P}_2\,\mathrm{p}$
Ds	$^3\mathrm{P}_2 \to {}^1\mathrm{D}_2\,\mathrm{s}$
	$^3\mathrm{F}_2 \to {}^1\mathrm{D}_2\,\mathrm{s}$
	$^3\mathrm{F}_3 \to {}^1\mathrm{D}_2\,\mathrm{s}$

to the invariant amplitude T as [55]:

$$d\sigma = \frac{1}{2(2\pi)^5\sqrt{s(s-4M_N^2)}}|T|^2\frac{d\mathbf{p}_c}{2E_c}\frac{d\mathbf{p}_d}{2E_d}\frac{d\mathbf{q}}{2E_\phi}\delta^{(4)}(P_i - P_f), \tag{2.13}$$

where $p_n = (En, \mathbf{p}_n)$ with n=a, b, c, d and $q = (E_\phi, \mathbf{q})$ are the four-momenta of the nucleons and the ϕ meson in the c.m. system, respectively. s is the total c.m. energy, and $P_{i,f}$ is the total four-momentum of the initial and final states. Further calculations [55] show that the ϕ decay distribution W in its helicity system can be written as:

$$\frac{d\sigma}{dcos\Theta d\Phi} = W(cos\Theta, \Phi) = \sum_{r,r'} M(r;\Theta,\Phi)\rho_{r,r'}M^*(r';\Theta,\Phi), \tag{2.14}$$

where $M(r;\Theta,\Phi)$ is the decay amplitude with r as the helicity of the ϕ meson, $\rho_{r,r'}$ is the density matrix that is expressed in terms of the production amplitudes T^r_β:

$$\rho_{r,r'} = \frac{\sum_\beta T^r_\beta T^{r'*}_\beta}{\sum_{r,\beta} T^r_\beta T^{r'*}_\beta}, \tag{2.15}$$

with a set of unobserved quantum numbers β. Assuming that the ϕ meson decays via $\phi \to K^+K^-$, and using the explicit form of the rotation function, one can get:

$$\begin{aligned} W(\cos\Theta,\Phi) &= \frac{3}{4\pi}[\frac{1}{2}(\rho_{11}+\rho_{-1-1})\sin^2\Theta + \rho_{00}\cos^2\Theta \\ &+\frac{1}{\sqrt{2}}(-Re\rho_{10}+Re\rho_{-10})\sin 2\Theta\cos\Phi \\ &+\frac{1}{\sqrt{2}}(Im\rho_{10}+Im\rho_{-10})\sin 2\Theta\sin\Phi \\ &-Re\rho_{1-1}\sin^2\theta\cos 2\phi + Im\rho_{1-1}\sin^2\Theta\sin 2\Phi], \end{aligned} \tag{2.16}$$

where the normalization condition $\rho_{11}+\rho_{-1-1}+\rho_{00}=1$ is already applied.

Let q denote the momentum of the ϕ meson in the c.m. frame, p that of the pp relative momentum, k that of the K^+K^- relative momentum. According to the allowed partial waves discussed in sec. 2.2.3, the angular dependence for momenta (k,q,p) relative to the beam direction can be derived as [62]:

$$\begin{aligned} W(\hat{k},\hat{q},\hat{p}) &= 3\ [\ \sin^2\theta_k\{\ a^{00}_{11} + \sqrt{5}(\ a^{20}_{11}\ P_2(\cos\theta_q) + a^{02}_{11}\ P_2(\cos\theta_p)\ )\ \}/2 \\ &+ \cos^2\theta_k\{\ a^{00}_{00} + \sqrt{5}(\ a^{20}_{00}\ P_2(\cos\theta_q) + a^{02}_{00}\ P_2(\cos\theta_p)\ )\ \} \\ &+ \sqrt{5}/4 \quad a_{10} \quad \sin 2\theta_p\ \sin 2\theta_k\cos(\phi_k+\phi_p) \\ &- \sqrt{15/8}\ a_{1-1}\ \sin^2\theta_p\ \sin^2\theta_k\cos(2\phi_k+\phi_p) \quad]/(4\pi)^3, \end{aligned} \tag{2.17}$$

where $P_2(\cos\theta)$ denotes Legendre polynomials and the parameters a hold the condition $\int W d\Omega^3 = a_{11}^{00} + a_{00}^{00} \equiv \sigma_{tot}$.

The angular distributions for each momenta are given after the integration of Eq.(2.17),

$$\frac{d\sigma}{d\Omega_k} = 3\ [\ a_{11}^{00}\ \sin^2\theta_k + 2\ a_{00}^{00}\ \cos^2\theta_k]/8\pi, \tag{2.18}$$

$$\frac{d\sigma}{d\Omega_q} = [\ a_{11}^{00} + \ a_{00}^{00} + \sqrt{5}(\ a_{11}^{20} + \ a_{00}^{20})\ P_2(\cos\theta_q)]/4\pi, \tag{2.19}$$

$$\frac{d\sigma}{d\Omega_p} = [\ a_{11}^{00} + \ a_{00}^{00} + \sqrt{5}(\ a_{11}^{02} + \ a_{00}^{02})\ P_2(\cos\theta_p)]/4\pi, \tag{2.20}$$

$$\frac{d\sigma}{d\Omega_{p'}} = [\ a_{11}^{00} + \ a_{00}^{00} + \ 5\ (\ a_{11}^{02} + \ a_{00}^{02})\ P_2(\cos\theta_{p'}) + b\cos 2\phi_{p'}\ P_2^2(\cos\theta_{p'})]/4\pi. \tag{2.21}$$

Here the parameter a are expressed by the partial wave amplitudes:

$$\begin{aligned}
a_{11}^{00} &= |Ss|^2 + 2|P^1s|^2/3 + |P^2s|^2/3 + |P^3s|^2 + 2|S^1p|^2 + |S^2p|^2/5 \\
&\quad + 2\sqrt{2}\ \Re(P^1sP^2s^*)/3 \ + \ 4\ \Re(S^1pS^2p^*)/\sqrt{10}\ , \qquad (2.22) \\
a_{00}^{00} &= |P^1s|^2/3 + 2|P^2s|^2/3 + |S^1p|^2 + 2|S^2p|^2/5 \\
&\quad - 2\sqrt{2}\ \Re(P^1sP^2s^*)/3 \ - \ 4\ \Re(S^1pS^2p^*)/\sqrt{10}\ , \qquad (2.23) \\
a_{11}^{20} &= -2|S^1p|^2/\sqrt{5} - \ \sqrt{5}|S^2p|^2/25 - \ 2\sqrt{2}\ \Re(S^1pS^2p^*)/5, \qquad (2.24) \\
a_{00}^{20} &= \ \ 2|S^1p|^2/\sqrt{5} + 4\sqrt{5}|S^2p|^2/25 - \ 4\sqrt{2}\ \Re(S^1pS^2p^*)/5, \qquad (2.25) \\
a_{11}^{02} &= \sqrt{5}|P^1s|^2/15 + \sqrt{5}|P^2s|^2/30 + \sqrt{5}|P^3s|^2/10 + \ \sqrt{10}\ \Re(P^1sP^2s^*)/15 \\
&\quad + \sqrt{30}\ \Re(P^1sP^3s^*)/5 + \ \sqrt{15}\ \Re(P^2sP^3s^*)/5, \qquad (2.26) \\
a_{00}^{02} &= \ -\ \sqrt{5}|P^1s|^2/15 - 2\sqrt{5}|P^2s|^2/15 + \ 2\sqrt{10}\ \Re(P^1sP^2s^*)/15, \qquad (2.27) \\
a_{10} &= -|P^1s|^2/\sqrt{15} + |P^2s|^2/\sqrt{15} - \ \Re(P^3sP^1s^*)/\sqrt{10} - \ \Re(P^3sP^2s^*)/\sqrt{5} \\
&\quad +2\ \Re(P^1sP^2s^*)/\sqrt{30} - \ \Re(P^2sP^1s^*)/\sqrt{30}, \qquad (2.28) \\
a_{1-1} &= |P^1s|^2/\sqrt{30} + |P^2s|^2/\sqrt{120} + \sqrt{30}|P^3s|^2/20 \\
&\quad + \Re(P^1sP^2s^*)/\sqrt{15} - \ \Re(P^1sP^3s^*)/\sqrt{5} - \ \Re(P^2sP^3s^*)/\sqrt{10}. \qquad (2.29)
\end{aligned}$$

2.2.5 Previous measurements

The near threshold $pp \to pp\phi$ reaction was measured by the DISTO [47] and ANKE [48, 63] Collaboration at four different excess energies. However, only two measurements provided the total and differential cross sections. The low statistics of the other two data sets [48, 63] were sufficient to extract total cross sections but it was hard to draw firm conclusions regarding the differential spectra.

The DISTO Collaboration reported the exclusive measurement of the $pp \to pp\phi$ reaction at $T_p = 2.85$ GeV, corresponding to an excess energy of $\epsilon = 83$ MeV [47]. A proton beam with momentum $p_{lab} = 3.67$ GeV/c was directed onto a liquid hydrogen target. Produced charged particles were tracked through a magnetic spectrometer

and detected by a scintillator hodoscope and an array of water Cerenkov detectors. The magnetic spectrometer consists of a dipole magnet, two sets of scintillating fiber hodoscopes inside the field, and two sets of multi-wire proportional chambers (MWPC) outside the field. The large acceptance of the spectrometer allowed for coincident detection of the final four charge particles. The total cross section ratio $R_{\phi/\omega}$ is observed to be about an order of magnitude larger than expected from predictions of the OZI rule. Furthermore, the measured differential cross sections show strong evidence for the importance of higher partial waves, but no attempt was made to make a consistent partial wave decomposition. The reason was in part due to the necessity to study in detail the structure of the non-ϕ K^+K^- background.

The ANKE Collaboration has also published results on the ϕ meson production in pp collisions at three beam energies, corresponding to excess energies of $\epsilon = 18.5, 34.5$ and 75.9 MeV. The final states were studied by detecting the decay products (K^+K^-) of ϕ mesons in coincidence with one of the forward-going protons, requiring that the missing mass be consistent with the non-observed second proton. The particle identifications in the ANKE spectrometer will be discussed in sec. 3.2. The data on ϕ production at the lowest energy are consistent with the particles in the final state being all in relative S-waves, with the only feature evident in the measured spectra coming from the strong proton-proton FSI. However, the low statistics at the two higher energies were only sufficient to extract total cross sections but it was hard to draw firm conclusions regarding the differential spectra which, on general grounds, are expected to be much richer than that at $\epsilon = 18.5$ MeV.

2.3 Kaon pair production

2.3.1 Motivations

The original motivation [65] for investigating the kaon-pair production in the near threshold $pp \to ppK^+K^-$ reaction was to understand the structure of the scalar

mesons $a_0(980)$ or $f_0(980)$, which decay mainly into $\eta\pi$ and $\pi\pi$ [5], respectively. Both scalar mesons have masses around 980 MeV/c^2 with the widths of the order of 50 -100 MeV/c^2 [66]. The nature of these scalar mesons has been a long-standing problem in meson physics. The standard quark model has difficulty in interpreting these mesons as quark-antiquark pairs ($q\bar{q}$) [67]. If we assume that a_0/f_0 belong to the same $J^{PC} = 0^{++}$ nonet, and consider the fact that f_0 must have a sizable admixture of strange quark since it couples strongly to $K\bar{K}$, then it is difficult to understand why its mass is the same as a_0 that would consist of non-strange quarks only. In addition, the mass and width of a_0/f_0 would be substantially smaller than those of the remaining members of the nonet, such as the $K_0^\star(1430)$ and $f_0(1300)$ [68]. In order to address this question, various explanations have also been proposed. In 1997 Jaffe performed a study of a four quark system ($qq\bar{q}\bar{q}$) in the MIT bag model and concluded that a_0/f_0 might be $qq\bar{q}\bar{q}$ states [69]. In turn, the authors from Ref. [70] have performed a detailed analysis of π-π scattering that show that f_0 may be a glueball. It was also suggested by Ref. [71] that the kaon-pair is a hybrid $q\bar{q}$/meson-meson system. Another interpretation proposed by Ref. [72, 73] described the a_0/f_0 as $K\bar{K}$ molecules in which kaon-antikaon systems are bounded by strong interactions. In this case the possibility of such a $K\bar{K}$ molecule crucially depends on the strength of the $K\bar{K}$ interaction, which can be probed in the near threshold production of kaon-antikaon pairs.

In addition to the $K\bar{K}$ subsystem, information about the KN system is of equal importance especially regarding to the possible KN molecular state $\Lambda(1405)$ [74] and kaonic nuclear systems, such as the deeply bound K^-pp states (see discussion in sec. 2.4). Up to now the scattering length a_{K^-p} has been mainly determined from several kaonic hydrogen measurements [75, 76, 77, 78]. But the situation is not yet clarified since first, the results of former measurements and the ones extracted from DEAR [79, 80] are in disagreement and second, it has been shown that contrary to

pionic hydrogen, the isospin violating correction cannot be neglected in the kaonic case [81]. Due to these still open questions and the fact that the K^-p scattering length extracted from previous scattering data has very large uncertainties [179], it is believed that low energy K^-p scattering data can provide an independent contribution to this important issue [83]. Furthermore, a precise knowledge about the $K^{\pm}N$ cross sections appears to be very important for calculations such as possible kaon condensation in neutron star [84] and strangeness production in a dense nuclear medium [85, 86, 87, 88, 89].

Furthermore, theoretical models in heavy-ion physics depend critically on input from elementary interactions. Meson-nucleon and meson-meson interactions dominate the nucleus-nucleus scattering mechanisms [90]. Thus, knowledge about the kaon pair production in the elementary NN interaction is important for studies of the production of hypernuclei in nucleon-nuclei scattering, and providing information about the existence of a quark-gluon plasma [3, 91].

2.3.2 Models

There are several different reaction mechanisms that can lead to the production of kaon pairs in pp collisions. The first one is related to the scalar meson a_0/f_0 production, which has been investigated within a meson-exchange approximation. The relevant diagrams for the $NN \to NNf_0 \to NN\bar{K}K$ reaction are those involving pions emission from nucleons with the s-channel production of the f_0-meson and its subsequent decay to $K\bar{K}$ or $\pi\pi$. The coupling constant at the $\pi\pi f_0$ vertex is determined from a fit to the reaction $\pi p \to f_0 n \to nK^+K^-$ [92].

Another contribution is from the production of the ϕ (1020) meson that decays via the $\phi \to K^+K^-$ channel (see discussions in sec. 2.2). One can also expect that kaon pairs are from the associated production of $pp \to pK^+Y^\star \to pK^+K^-p$ in pp collisions [63]. There are several excited hyperons that could contribute to such

a reaction. Of particular interest for low energy productions are the $\Sigma(1385)$ and $\Lambda(1405)$ [63]. Though nominally lying below the sum of the K^- and p masses, their large widths (50 MeV/c^2) ensure that they overlap with the K^-p threshold [93].

Moreover, a one-boson exchange model has also been proposed [94] to describe the kaon pair production. This model includes an energy dependent scattering amplitude derived from the fit of the total cross sections in $K^{\pm}p \to K^{\pm}p$ [95] while the pp-FSI was not included. However, this model underestimates the total cross section at low excess energies.

Furthermore, a coupled channel model taking into account the $K^+K^- \rightleftharpoons K^\circ\bar{K}^\circ$ transition has been proposed [96] to describe the total cross section at low energies. This model is calculated within the K-matrix formalism and the associated phenomena discussed extensively by [97, 98]. The calculations show the dominance production of the $I = 0$ $K\bar{K}$ pairs in the near threshold region.

Additionally, a resonance model is also proposed to study the kaon pair production in pp collisions [99]. In the model, the resonance $N^*(1535)$ is formed via the $pp \to pN^*(1535)$ reaction, which decays into $K^+\Lambda(1405)$. The excited hyperon $\Lambda(1450)$ further decays via $\Lambda(1405) \to K^-p$. Within this model, the energy dependence of the total cross sections is well reproduced.

Up to now there is no full calculation available and further theoretical efforts are required to give a complete picture of the K^+K^- production.

2.3.3 A simple ansatz

In principle, one can describe the $pp \to ppK^+K^-$ reaction at all energies in terms of final state interactions between pp and $K^{+/-}$ with the two protons. However, there is no reliable way of carrying out such a program without solving multi-body equations, which is outside the scope of this thesis. Here as a first step we make the *ad hoc* assumption [63] that the overall enhancement factor is the product of the

enhancements in the pp , K^+K^- and two K^-p systems (it is believed that the K^+p interaction might be weakly repulsive and, if so, its neglect would be interpreted as extra attraction in the K^-p system):

$$F = F_{pp}(q_{pp}) \times F_{Kp}(q_{Kp_1}) \times F_{Kp}(q_{Kp_2}). \tag{2.30}$$

All final state interactions are evaluated at the appropriate relative momenta q in the corresponding subsystems.

In order to obtain this formula, firstly one can consider that when two particles interact strongly in the final state, the resulting matrix element involves an average of a production operator with the relative wave function $\psi_{\vec{q}}(\vec{r})$. If the interaction is of very short range, the wave function may be evaluated at the origin to leave an enhancement factor

$$F_2(q) \propto \psi_{\vec{q}}(0) \propto \frac{1}{D(q)}\,, \tag{2.31}$$

where $\vec{q}$ is the relative momentum in the pair and $D(q)$ is the S–wave Jost function [100]. In the commonly used scattering length approximation, one retains only the linear term in q, in which case $F(q) = 1/(1 - iqa)$, where a is the scattering length of the interacting pair.

If two or more pairs of particles interact in the final state, there is no reliable prescription to evaluate an analogous enhancement factor since a three–body equation then needs to be solved. If we denote the interacting pairs as 12 and 13 (strongly interacting pairs), the corresponding wave function will be $\Psi_{\vec{q}_{12},\vec{q}_{13}}(\vec{r}_{12},\vec{r}_{13})$. We now make the *ad hoc* assumption that this wave function factorizes in the form

$$\Psi_{\vec{q}_{12},\vec{q}_{13}}(\vec{r}_{12},\vec{r}_{13}) = \psi_{\vec{q}_{12}}(\vec{r}_{12}) \times \psi_{\vec{q}_{13}}(\vec{r}_{13})\,. \tag{2.32}$$

In this case, the three–body enhancement factor is simply the product of the two–

body factors, evaluated at the appropriate relative momenta:

$$\begin{aligned} F_3(q_{12}, q_{13}) &= F_2(q_{12}) \times F_2(q_{13}) \\ &\approx \frac{1}{(1 - iq_{12}a_{12})(1 - iq_{13}a_{13})} \,. \end{aligned} \tag{2.33}$$

It must be stressed that Eq. (2.33) is merely an *ansatz* to try to understand our ensemble of data and, even if it provides a satisfactory description of them, this does not mean that it is applicable more generally. However, Eq. 2.33 has also been used to treat the near threshold $pp \to pp\eta$ reaction, where all the final pairs of particles interact strongly [101].

The approach does retain the necessary pole structure when $q_{12} = -i/a_{12}$ and similarly for q_{13}. Thus particle-1 can interact simultaneously with both 2 and 3. Furthermore, to lowest order in the momenta, the *ansatz* corresponds to the scattering length of particle-1 from a composite 2+3 with the desired combined scattering length of $a = a_{12} + a_{13}$.

In principle, one can take the simple ansatz Eq. 2.30 to extract the scattering length a_{K^-p} by fitting the experimental data as [63]. However, it should be noted here that this ansatz underestimates the cross section at very low K^+K^- invariant masses, i.e., in the interval between the K^+K^- and $K^\circ\bar{K}^\circ$ thresholds. A similar underestimation is found in the same region of the $pn \to dK^+K^-$ data [102]. It is therefore natural to speculate that these effects are caused by ignoring the K^+K^- FSI in Eq. 2.30. A further investigation [96] shows that the data can be understood in terms of an elastic K^+K^- scattering plus a contribution coming from the $K^+K^- \leftrightharpoons K^\circ\bar{K}^\circ$ charge-exchange scattering. In addition, a recent reanalysis [103] of the data from COSY-11 put weak limits on the $K\bar{K}$ scattering length: $|Re(a_{K^+K^-})| = 0.5^{+4.0}_{-0.5}$ fm and $Im(a_{K^+K^-}) = 3.0 \pm 3.0$ fm. However, the uncertainties are too large to make any conclusion regarding the strength of the elastic K^+K^- FSI.

After including the K^+K^- FSI, a completed treatment of the final state interactions in the $pp \to ppK^+K^-$ reaction is applied in the data analysis to perform acceptance corrections, as discussed in sec. 4.2.

2.3.4 Previous measurements

Measurements of the $pp \to ppK^+K^-$ reaction have been performed above and below the ϕ meson production threshold by the ANKE [48, 63], COSY-11 [83, 103, 104, 105], and DISTO [47] Collaborations. The above ϕ threshold data with high statistics have been collected by DISTO and ANKE. However, the investigation of this region was hampered by the need to separate the non-ϕ from the ϕ contribution and the fact that the data were spread over a very wide range of K^+K^- invariant masses. The below ϕ threshold measurement can provide useful information about the interesting FSI effects without the distortion of ϕ meson. However, the limited statistics in the low energy COSY-11 data make the study difficult [83, 103, 104, 105].

The COSY-11 Collaboration has reported the $pp \to ppK^+K^-$ reactions at several different excess energies $\epsilon = 3, 10, 17$ and 28 MeV below ϕ threshold. During the measurements, the produced charged particles were detected by a magnetic spectrometer that includes a C-shaped dipole magnet, two drift chambers and two scintillation hodoscopes. The obtained event counts are rather limited in all energies. But within such limited statistics the differential K^-p invariant mass distribution normalized to the K^+p system shows a strong preference to the low K^-p invariant masses. The data clearly demonstrate the sensitivity of the KN interaction in the ppK^+K^- final state and, suggest that K^-p interaction might have a connection to the $\Lambda(1405)$ [83]. The results from COSY-11 also show that the scalar meson a_0/f_0 production cannot in fact to be the dominant driving mechanism in the near threshold kaon pair production.

The ANKE Collaboration has also measured the kaon pair production in pp

collisions at three different excess energies of $\epsilon = 51, 67$ and 108 MeV, which are all above the ϕ meson threshold. The non-ϕ kaon pair data were separated from the decay products of ϕ-meson by applying the proper cuts on the K^+K^- invariant masses. The data also showed that the ratio of the differential cross sections in terms of the K^-p and K^+p invariant masses are strongly peaked toward low masses. This effect can be described quantitatively by considering the K^-p final state interaction with an effective scattering length of $a_{K^-p} = 1.5i$ fm. However, the uncertainties of both the real and image part of a_{K^-p} are rather large. The ANKE measurements at three excess energies also showed some enhancement at low K^+K^- invariant masses but with at least a break of slope at the $K^\circ\bar{K}^\circ$ threshold. A combined analysis of all the results in this region [96] shows that the data can be understood in terms of a final state interaction involving both K^+K^- elastic scattering plus a contribution from $K^+K^- \leftrightharpoons K^\circ\bar{K}^\circ$ charge exchange. Although suggestive, the data are not sufficient to draw firm conclusions. In addition, only the total cross section is available for the data from DISTO.

2.4 Kaonic nuclear clusters

2.4.1 Motivations

As discussed in sec. 2.3, if the kaon-nucleon interaction is strongly attractive, a quasi-bound state $\Lambda(1405)$ just below the $\bar{K}$N threshold can be formed [106]. Therefore, it is also possible that strong interactions in isospin-zero channel might be sufficient to form cluster objects of two or more nucleons bound together with kaons [107]. The lightest system $\bar{K}NN$ is a fascinating system to investigate such a possibility. The K^-pp bound state was predicted in 2002 [108] with a binding energy of 48 MeV. The structure of the K^-pp, which emerges from the $\bar{K}N$ interaction, is deduced in a semi-empirical model that reproduces the binding energy (27 MeV) and width (40 MeV) of the $\Lambda(1405)$. A schematic representation of the $\Lambda(1405)$ and the K^-pp

bound state with the corresponding *rms* distance are shown in Fig. 2.5. Here the K^- acts like a glue between one proton ($\Lambda(1405)$) or the two protons (K^-pp).

Recently, the K^-pp bound state has been actively studied because it has the largest number of $\bar{K}N$ pairs with $I = 0$ and is estimated to be the strongest bound system among the three-body systems. The structure and production mechanism of the K^-pp bound state have been investigated using various theoretical approaches [109, 110, 111, 112, 113, 114]. The binding energy and the width were predicted to be 9 - 95 MeV and 34 - 110 MeV, respectively. These predicted values are in considerable disagreement depending on the $\bar{K}$N interaction models and the calculation methods. Moreover, all investigations concerning kaonic clusters are limited in their predictive power as the relevant energy range is far below the $\bar{K}N$ threshold. Due to the fact that the $\Lambda(1405)$ is the only accessible observable below this threshold, a full understanding the production mechanism of $\Lambda(1405)$ is crucial for any serious statement about the possible existence of deeply bound kaonic clusters.

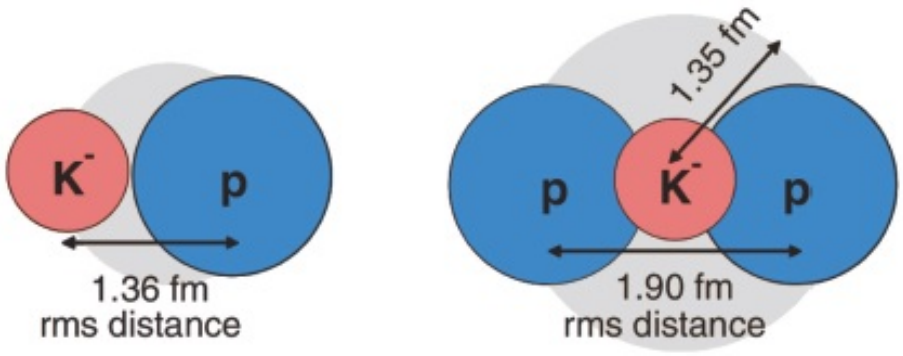

FIGURE 2.5: Structure of the $\Lambda(1405)$ (left) and K^-pp bound state (right) [108].

On the other hand, according to the theoretical predictions [115], the formation of a kaonic bound state (K^-pp) is possible in pp collisions via the $\Lambda(1405)$ doorway. The underlying idea is that the $\Lambda(1405)$ (being already a K^-p bound state) is

produced together with another proton with relatively small momentum, the highly attractive K^--nucleon interaction might lead to the capture of a second proton by the $\Lambda(1405)$ and hence form a K^-pp bound state via $\Lambda(1405)p \rightarrow K^-pp$. This scenario is predicted to be favored for pp collisions at kinetic energies between 3 and 4 GeV, where a large momentum transfer from the projectile to the target characterizes the dynamics and creates the optimal conditions for the formation of the kaonic cluster [116].

2.4.2 Kinematics

According to Ref. [117], the K^-pp bound state decays into the following channels:

$$K^-pp \rightarrow \Lambda + p \tag{2.34}$$

$$\rightarrow \Sigma^\circ + p, \tag{2.35}$$

$$\rightarrow \Sigma^+ + n, \tag{2.36}$$

The analysis in the context of pp collisions performed with the ANKE spectrometer will focus on the investigation of the K^-pp bound state via its decay into Λ and p. The produced Λ further decays into p and π^-. Since the final state contains only the charged particles (p, K^+, p, π^-), the intermediate Λ and finally the K^-pp can be reconstructed via the invariant mass or missing-mass technique (see discussions in sec. 4.4.2).

However, the ordinary production can also contribute to the $ppK^+\pi^-$ final state, which should be studied carefully.

$$p + p \rightarrow p + p + K^+\pi^-, (\text{direct production}) \tag{2.37}$$

$$\rightarrow p + K^+ + \Lambda. (\Lambda \text{ production}) \tag{2.38}$$

Although further requirements on the invariant mass of $p\pi^-$ to be consistent with Λ mass will remove the contributions from the direct production to the final state,

it is not trivial for the ordinary Λ production. Thus a full understanding of the Λ production is crucial regarding the formation of the K^-pp bound state. Three production mechanisms were proposed for the Λ production in pp collisions, as illustrated in Fig. 2.6. However, in the non-resonance approach, theoretical studies do not yield a conclusive picture at present. Some calculations are based on one boson (pion or kaon) exchange amplitudes where kaon exchange was found to be the dominant process [118, 119]. In other studies the total cross section data at higher energies are well reproduced by pion exchange [66, 120]. In the resonance model approach [121, 122, 123, 124, 125], the $K\Lambda$ production proceeds via the excitation of the $N^\star(1650)$ resonance or a combination of the $N^\star(1650)$, $N^\star(1710)$ and $N^\star(1720)$ resonances. In addition, in the calculation of [126], the $N^\star(1650)$ and $N^\star(1710)$ resonances are found to be the dominant contributions.

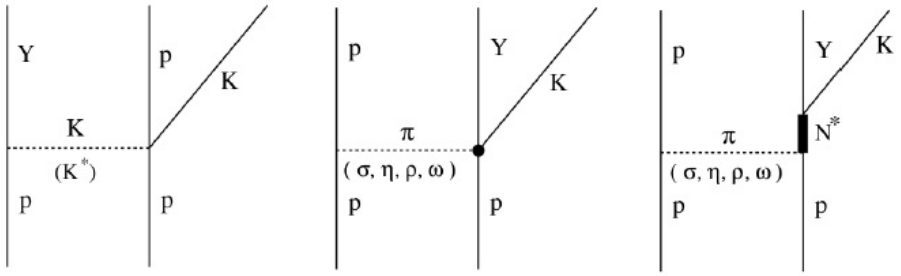

FIGURE 2.6: Production mechanisms for the $pK^+\Lambda$ final state including non-resonant strange (left) and non-strange (middle) meson exchange. The right figure represents the resonant production via an intermediate $N^\star$ resonance [64].

To obtain more information on the various contributions, the data taken by the COSY-TOF collaboration at beam momentum of 2.95, 3.20 and 3.30 GeV/c [64] were compared with the ISOBAR model by Sibirtsev [51], which takes into account different $N^\star$-resonances and the $p\Lambda$ final state interaction. The Dalitz plot distribution

is given as [64]:

$$\frac{d^2\sigma}{dm^2_{K\Lambda}d^2m_{p\Lambda}} = fl \cdot ps \cdot |(\sum_R (C_R \cdot A_R) + C_N \cdot A_N) \cdot (1 + C_{FSI} \cdot A_{FSI})|^2 \qquad (2.39)$$

Here $m_{K\Lambda}$ and $m_{p\Lambda}$ are the invariant masses of the $K\Lambda$ and $p\Lambda$ system. The quantity fl gives the normalization to the total cross section, ps denotes the phase space. A_R are the relativistic Breit-Wigner-amplitudes of the three considered $N^\star$-resonances. A_{FSI} denotes the amplitude of the $p\Lambda$ final state interaction as given by the Juelich YN-model [127]. The strengths of the various contributions were adjusted individually to achieve a best fit for the various Dalitz plots. By comparing the different resonance strengths at various beam energies, an energy dependence of the single $N^\star$ contribution strength can be deduced. This dependence is shown in Fig. 2.7. The red diamonds represent the $N^\star(1650)$ strengths, the combined strengths of $N^\star(1710)$ and $N^\star(1720)$ are shown by the blue squares. The dashed curves indicate the fits to the data points and the coloured bands visualize the 3σ error bands of the fits to the contributed strengths. The plot shows a diminishing of the relative $N^\star(1650)$ contribution with increasing beam energy, whereas the influence of the $N^\star(1710)$ and $N^\star(1720)$ resonances increases.

Moreover, resonances with higher masses such as the $N^\star(1900)$ could be produced at higher energies. A dedicated simulation by the HADES Collaboration, including the $pK^+\Lambda$ phase-space distribution and the contribution from $N^\star(1720)$ and $N^\star(1900)$, achieves a good description of the experimental data at $T_p = 3.5$ GeV [116]. But the simulation fails to describe the angular distributions, which suggests the necessity of a partial wave analysis (PWA) of the $pK^+\Lambda$ final state. The details of such a PWA will be discussed in sec. 5.4. To come to conclusive results concerning the $K\Lambda$ production mechanism, the measurements should concentrate on data covering the full phase space.

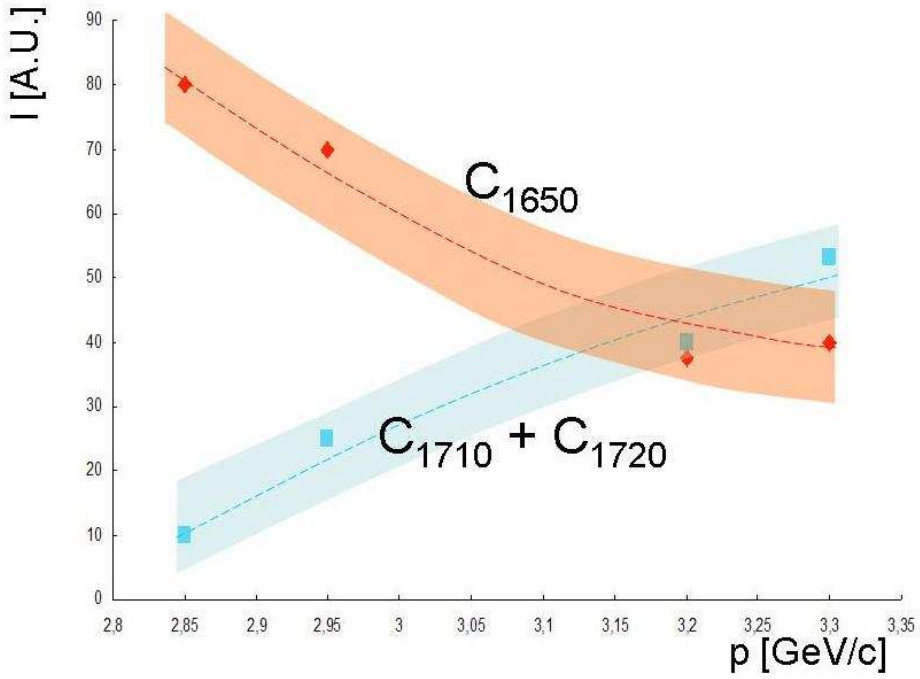

FIGURE 2.7: Contribution of $N^\star(1650)$ compared to the sum of $N^\star(1710)$+$N^\star(1720)$ as a function of the beam momentum [64].

2.4.3 Previous measurements

The kaonic bound state was firstly reported by the FINUDA Collaboration [128] using the measurement of stopped kaons on several solid targets. Later, the DISTO Collaboration analyzed pp collisions at $T_p = 2.85$ GeV and found evidence for the K^-pp bound state [129]. However, no obvious evidence of such a bound state was found in the γd reaction by the LEPS Collaboration [130] and pp collisions at $T_p = 3.5$ GeV by the HADES Collaboration [116].

In the FINUDA experiment [128], K^- from the decay of ϕ mesons were stopped in several solid nuclear targets to form the reaction. Fig. 2.8 shows the invariant mass distribution of Λp. The peak at 2256 MeV/c^2 is interpreted as a K^-pp bound state with a binding energy of 115^{+6+3}_{-5-4} MeV and a width of 67^{+14+2}_{-11-3} MeV. However, there are some theoretical interpretations that the observed peak can be explained by the

two-nucleon absorption with the final state interaction of outgoing particles [131].

$$K^- +^A Z \rightarrow^{A-2} (Z-2) + \Lambda + p \tag{2.40}$$

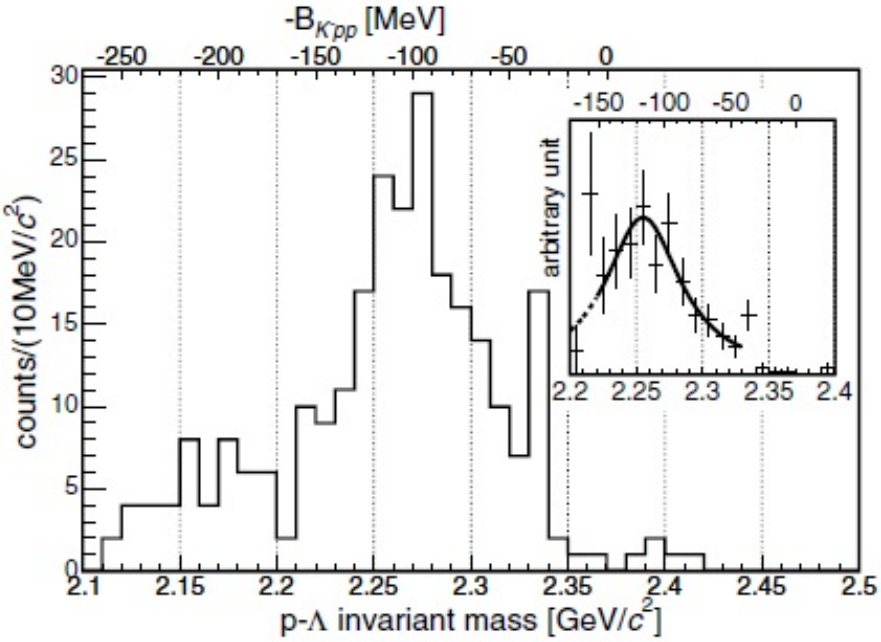

FIGURE 2.8: Λp invariant mass spectrum from FINUDA experiment [128].

The DISTO Collaboration also reported on an indication of the K^-pp bound state measured in the exclusive $pp \rightarrow pK^+\Lambda$ reaction at $T_p = 2.85$ GeV [129]. The observed spectra of the K^+ missing mass and the Λp invariant mass with high transverse momenta of p and K^+ revealed a broad distinct peak with a mass $2267 \pm 3 \pm 5$ MeV/c^2 and a width of $118 \pm 8 \pm 10$ MeV. The measured widths from FINUDA and DISTO are different between the two groups, and they are inconsistent with the existing theoretical predictions. Thus, the existence of K^-pp bound state has not been established yet, and new experiments using different reactions could help to resolve the controversial situation.

Recently, a search for the K^-pp bound state has also been performed using the $\gamma d \rightarrow K^+\pi^- X$ reaction at $E_\gamma = 1.5 - 2.4$ GeV at LEPS [130]. A statistically signif-

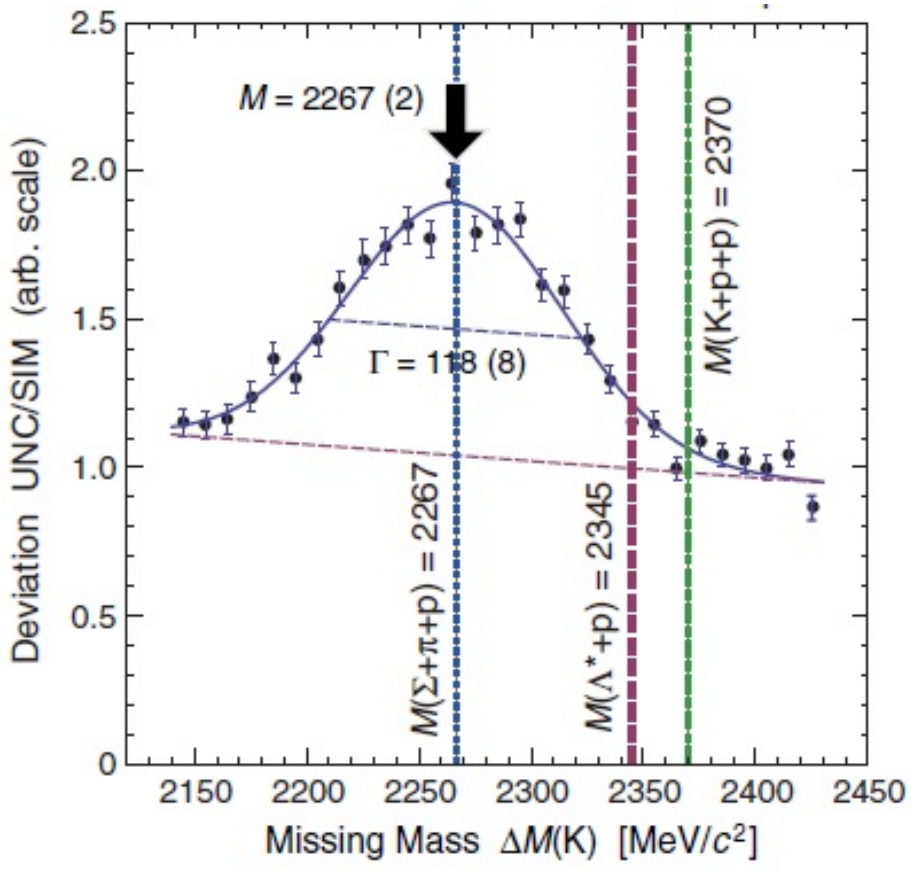

FIGURE 2.9: Λp invariant mass spectrum from the DISTO experiment [129] at $T_p = 2.85$ GeV after the cut of $|cos\theta_{cm}(p)| < 0.6$.

icant bump structure was not observed in the region from 2.2 to 2.36 GeV/c^2, and the upper limits of the differential cross section for the K^-pp bound state production were determined to be 0.1-0.7 μb for a set of assumed binding energy and width values.

In addition, the HADES Collaboration has studied the $pp \rightarrow p\Lambda K^+$ reaction in pp collisions to search for the K^-pp bound state [116]. Their results show that the phase-space simulations cannot describe the experimental distributions. The disagreement cannot be overcome by adding the contribution of one resonance in the $p - \Lambda$ decay channel with a mass around 2300 MeV/c^2. It suggests that the need of a partial wave analysis to disentangle the different contributions to the measured

$pK^+\Lambda$ final state, which is important to search for the bound state.

3

Experimental Apparatus

The experiments were carried out employing the ANKE spectrometer [132] and unpolarized proton beams from the COSY accelerator [133]. A hydrogen cluster gas jet target and solid strip targets were used for pp and pA reactions, respectively. The produced charged ejectiles were then detected by ANKE detection systems.

3.1 The COoler-SYncrotron

The COSY accelerator [133] is operated at the Forschungszentrum Jülich. It consists of an isochronous cyclotron (JULIC) (used as an injector), a storage ring with a circumference of 184 m, and internal and external target stations. COSY provides beams of polarized and unpolarized protons and deuterons in the momentum range between 295 MeV/c and 3.65 GeV/c, corresponding to a kinematic energy range from 45 MeV to 2.83 GeV for protons, and from 67 MeV to 2.23 GeV for deuterons, respectively. The storage ring can be filled with up to 10^{11} particles that leads to typical luminosities of $10^{31} cm^{-2} s^{-1}$ for an internal cluster target. Beams can be cooled by using electron cooling at injection energy (40 - 183 MeV) as well as by

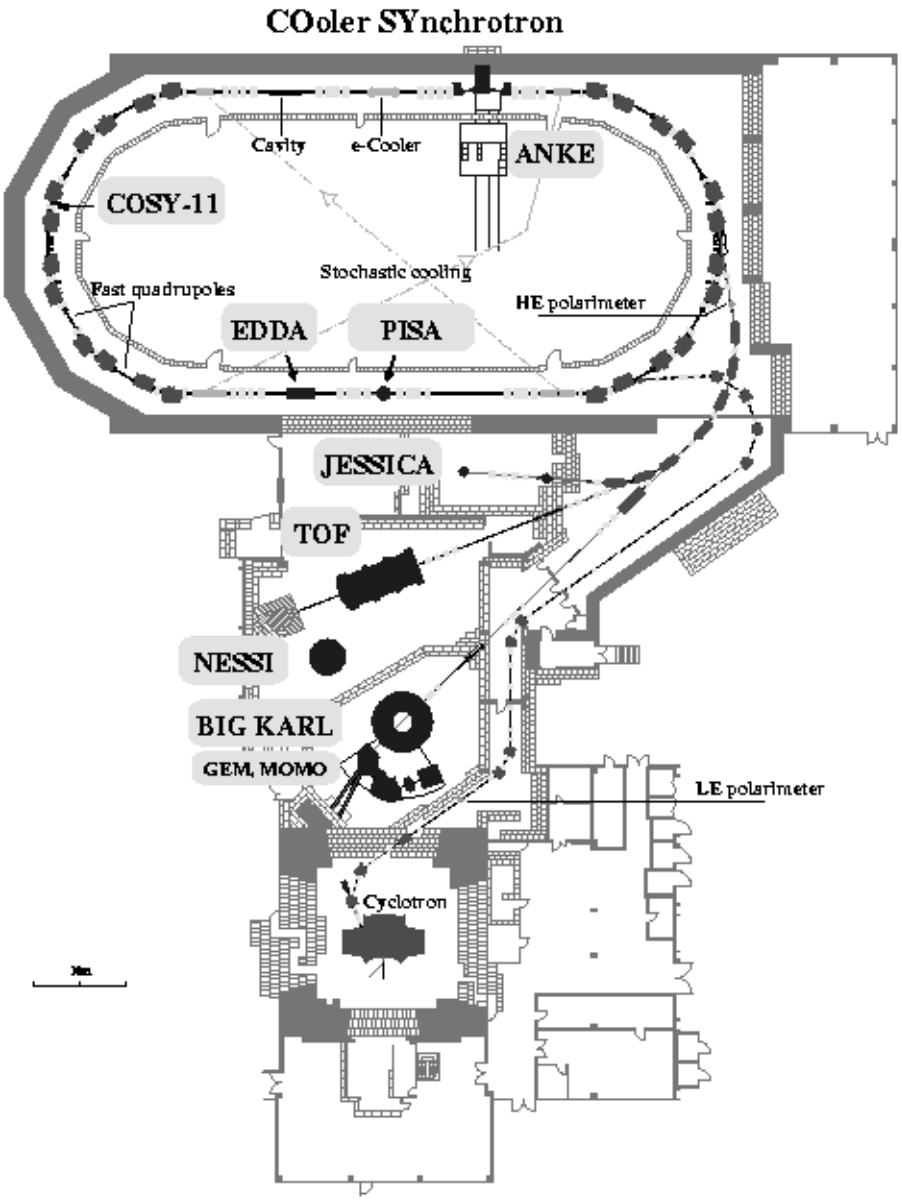

FIGURE 3.1: The COoler Synchrotron layout [133]. The ANKE detector was installed in an internal target position of COSY.

stochastic cooling at high energies (830 - 2830 MeV). With the cooling systems, the beam momentum resolution is reduced from a typical value of $\Delta p/p = 10^{-3}$

down to 10^{-4}. The circulating beam has been used by several collaborations of internal target experiments (COSY-11 [134], WASA [135], ANKE [132]), and for external experiments (i.e. COSY-TOF [136]). There are several advantages for the internal target experiments. Firstly, background reactions are minimized for windowless targets like gas jet targets. Secondly, luminosities can be increased since the beam repeatedly passes through the target (up to 10^6 times per second). With such targets, the degradation of the energy information and the reaction products is largely avoided. A sketch of the layout of COSY is presented in Fig. 3.1.

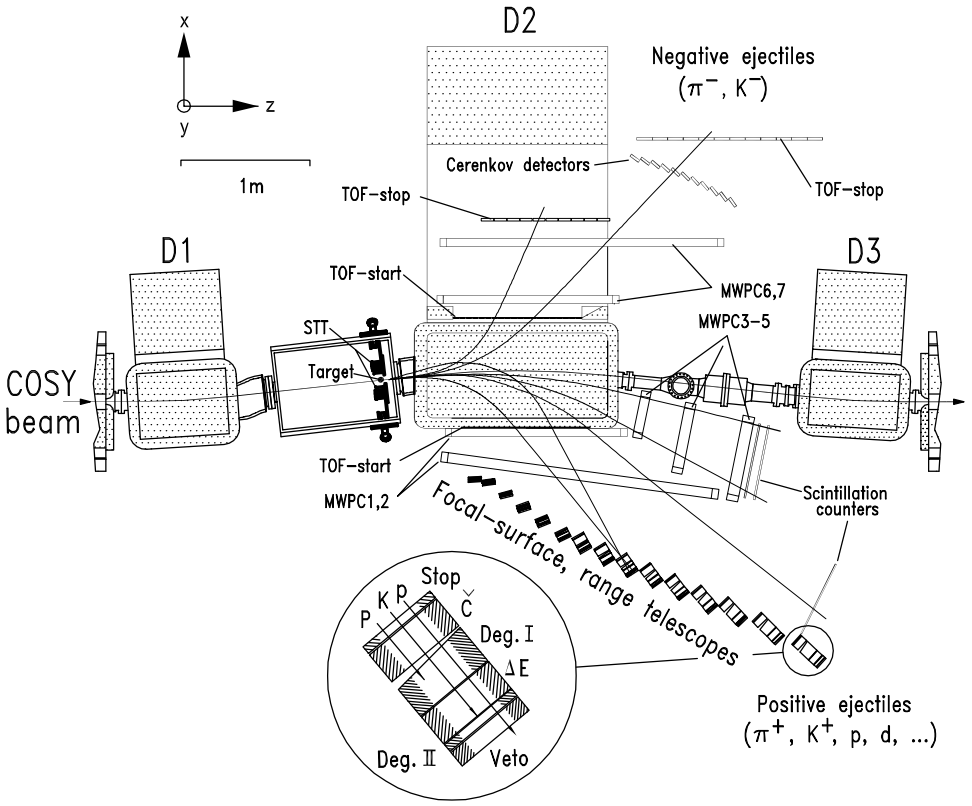

FIGURE 3.2: Layout of the ANKE spectrometer including the dipole magnets D1-D3, a target chamber and vacuum chambers. Detector systems for positively and negatively charged ejectiles are placed at the side exits of D2 as well as in the forward direction [132].

3.2 The ANKE spectrometer

The ANKE magnetic spectrometer [132], which locates at an internal target position of the storage ring of COSY, is a facility designed for the study of hadronic reactions. It consists of three dipole magnets D1, D2 and D3. The magnet D1 deflects the circulating COSY beam by an angle α off its original path onto a target, while D3 guides the beam back to the ring orbit. The rectangular C-shaped magnet D2 is used as a spectrometer magnet, which has a maximum field length of ~ 1.57 T and a maximum deflection angle of 10.6°. The angular acceptance of the spectrometer is $\pm 3 - 5^{\circ}$ in the vertical direction and $\pm 10 - 18^{\circ}$ in the horizontal direction.

The target chamber is placed in front of the D2 magnet. Different types of targets such as a solid strip target, cluster-jet target or polarized storage-cell gas target can be installed inside the target chamber, see sec. 3.3 for detailed discussions.

In proton-induced processes with hydrogen or nuclear targets, ejectiles of all charged states are produced either directly or via the decay of short-lived reaction products (for example $\phi \rightarrow K^+K^-$). In the ANKE spectrometer, positively charged particles (p, π^+, K^+) are deflected into the detectors on the right-hand side of the COSY beam, while negatively charged ones (π^- and K^-) are bent to the left-hand side. Therefore, ANKE was designed to consist of positive, negative and forward detectors for detecting positively charged, negatively charged and fast-going positively charged particles, respectively. In the following sections, each detection system will be discussed in details.

3.2.1 Positive side detection system

The layout of the positive side detection system (Pd) is shown in Fig. 3.3. The Pd system consists of the START and STOP counters for time-of-flight (TOF) measurements, and two multi-wire proportional chambers (MWPCs) for tracks reconstruc-

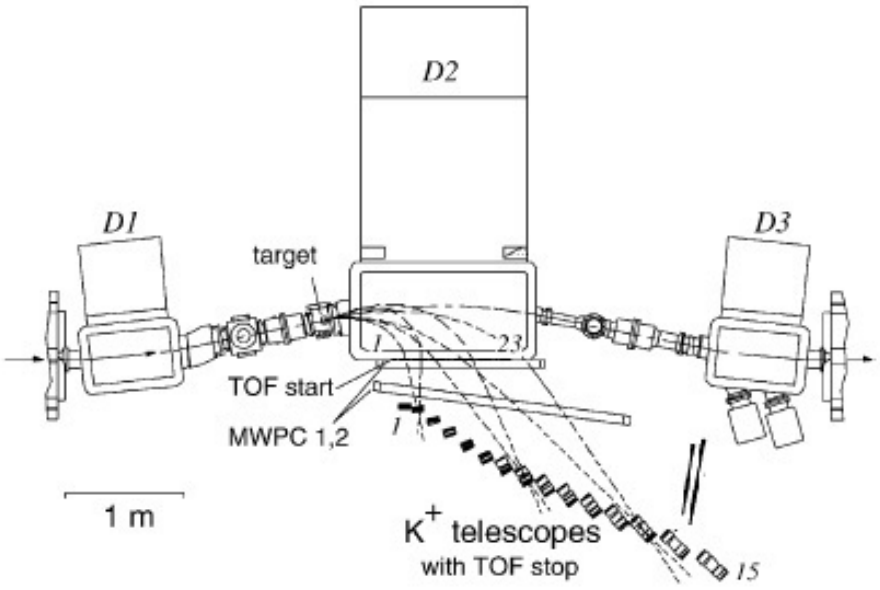

FIGURE 3.3: Top view of the positive detection system (Pd). Pd consists of the START and STOP counters, and two multi-wire proportional chambers (MWPCs).

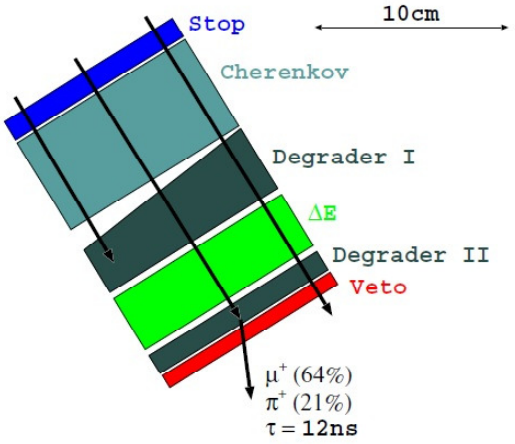

FIGURE 3.4: Sketch of telescope 13. It consists of a STOP counter, a Cerenkov counter, two degraders and a ΔE counter, and a veto counter.

tion. It is shown [132] that protons, pions and kaons can be identified from each other on the basis of their TOF and momenta.

The 23 thin START plastic scintillation counters have different thickness de-

Table 3.1: Dimensions of positive START counters [132].

Counter	Height[mm]	Width[mm]	Thickness[mm]
1-2	270	50	0.5
3-5	270	50	1.0
5-23	270	50	2.0

pending on the counter number, which are positioned as close as possible to the exit window of D2. Starting from the low-momentum side, the START counters 1 and 2 have a thickness of 0.5 mm, where it is 1.0 mm for detectors 3-5 and 2.0 mm for the rest. The thickness of the START counters is a compromise between sufficient light output and small angular spread by multiple scattering. The dimensions for Pd START counters are listed in Table 3.2.1.

The Pd system also consists of 21 STOP scintillation counters with different heights in the range of 520-1000 mm, which are adapted to the vertical acceptance of D2. All the STOP counters are 10 mm thick and 100 mm wide. The first 15 STOP counters are part of range telescopes at the focal plane of D2, where the rest of the 6 STOP counters (so called Side Wall) are mounted between the telescopes and the forward detection system.

The range telescopes are designed by [145] for inclusive K^+ measurement as shown in Fig. 3.4. Each telescope covers a limited momentum range given by its width and the dispersion of D2. A telescope consists of a stop counter, a Cerenkov (only telescopes 7-15) counter, two copper degraders, an energy-loss counter (ΔE), and a veto counter. The thickness of the passive degraders was chosen such that the positive kaons deposit the maximum amount of energy in the ΔE counter and stop either at the edge of it or in the second degrader. The decay products of K^+ are then registered in the veto counter. The procedure of K^+ identification using the delayed veto technique is described in detail in sec. 4.3.

The Side Wall is used for energy loss measurement as well as forward tracking

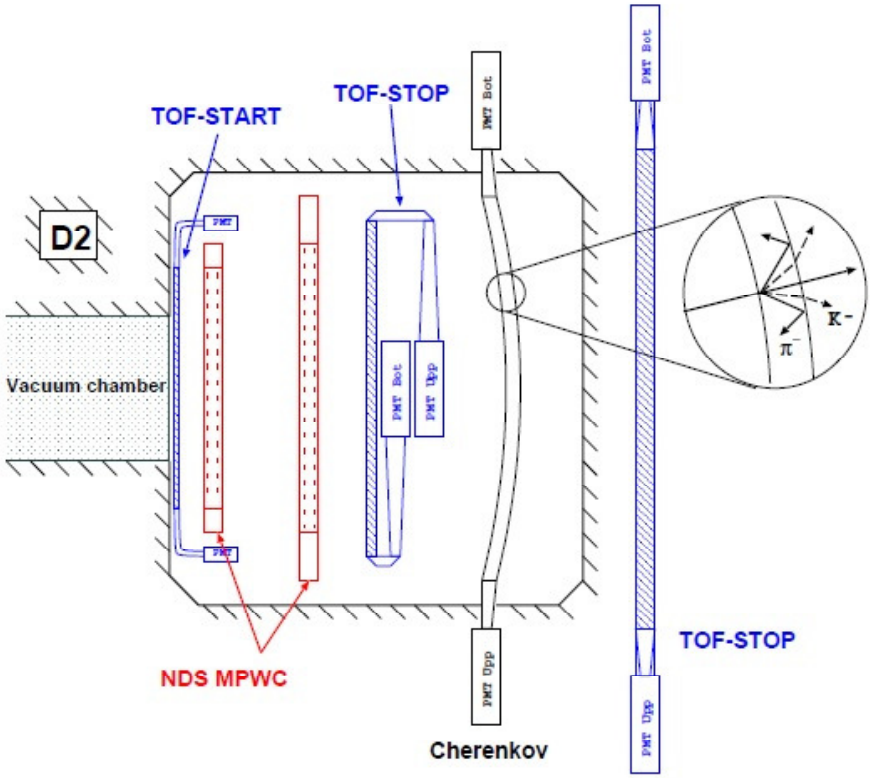

FIGURE 3.5: The side view of the negative detection system, which consists of TOF START-STOP counters and MWPCs.

of fast-going positively charged particles. For all scintillators the light is detected at both ends via photo-multipliers. During the experiments one inch photo-tubes are used for the START counters and two inch tubes for the STOP counters.

Besides the START and STOP counters, Pd contains two MWPCs for determining the emission angles and momenta of the produced ejectiles. The first MWPC is placed close to ANKE START counters, while the second MWPC is connected to D2 magnet. Both chambers are operated with a gas mixture of 70 % argon and 30 % CO_2 with some alcohol admixture. The sensitive areas are 350×1300 and 600×1960 mm^2 for the first and second chamber, respectively. Each chamber consists of three planes of anode wires (vertical, +30°, -30°). Based on hits in the MWPCs, the particle momentum can be reconstructed with a resolution of $\sim 2\%$.

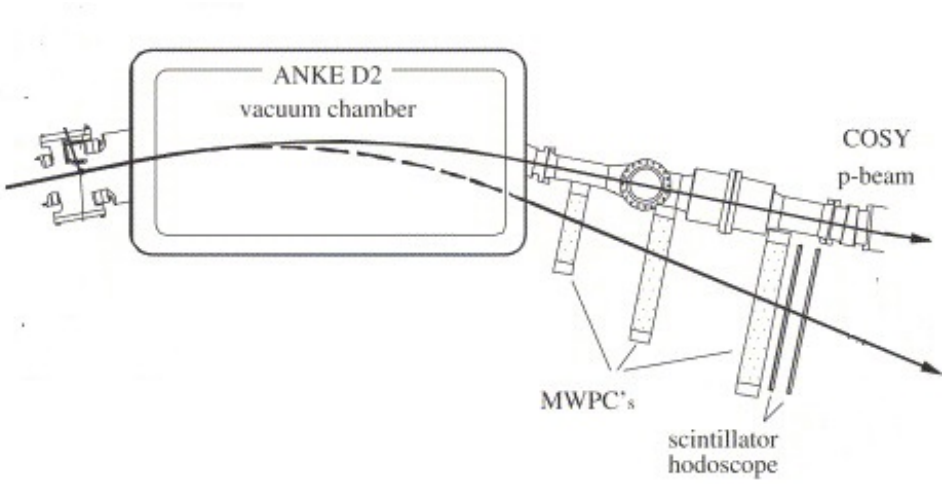

FIGURE 3.6: The top view of forward detection system.

Table 3.2: Dimensions of negative START and STOP counters [145].

Counter	Height[mm]	Width[mm]	Thickness[mm]
START	270	50	2
STOP(1-12)	350	80	10
STOP(12-22)	250	150	20

3.2.2 Negative side detection system

The negative side detection system (Nd) is placed partly inside the return yoke of the dipole magnet D2 [135]. It consists of 20 START and 22 STOP counters for TOF measurements, and two MWPCs for particle momentum reconstruction. The dimensions of the negative START and STOP counters are listed in Table 3.2.2.

Due to space limitation, the measured time resolution between the START and STOP counters in Nd is about 1 ns, slightly inferior compared with Pd. However, this time resolution is insufficient to distinguish between π^- and K^- with momenta above 500 MeV/c. In order to obtain a better separation, TOF information between the target and STOP counters is used. In practice, the time difference between the target and STOP counters is calculated by the TOF difference of correlated positively and negatively charged particles. In this case, the positively charged particles are

detected in the Pd system where the STOP counters are located in the focal plane of D2 and thus, particles have a well defined momenta. The main advantage of this technique is the better time resolution of the thick STOP counters compared to the thin START counters. Moreover, the long path length from the target to STOP counters leads to a larger time difference between pions and kaons. This technique will be discussed in sec. 4.3.

The MWPCs in Nd have the same design and performance as those in Pd, which allows a resolution of $\sim 2\%$ for momenta reconstruction.

3.2.3 Forward detection system

The ANKE forward detection system (Fd) [138], which consists of three MWPCs and two layers of scintillator hodoscopes, is located between the D2 and D3 magnets close to the beam pipe. The distance between the beam tube and the forward detector is about 0.7 m. Such a location results in severe requirements for the tracking system. First of all, due to the closeness to the beam pipe, the Fd system must be able to operate at rather high counting rates. In addition, one has to achieve a sufficiently high spatial resolution (better than 1 mm) for obtaining a momentum resolution of $\sim 1\%$. To fulfil such requirements, a system including three MWPCs was developed with a small anode-cathode gap, filled with a fast gas mixture of CF_4 and iso-C_4H_{10}. Each MWPC contains one X and Y module that consists of a wire and strip plane. Wires are oriented vertically in the X wire planes, and horizontally in the Y planes. The strips are inclined by 18° with respect to the vertical axis in the X planes, and at -18° in the Y planes.

In addition to MWPCs, there are two layers of scintillator counters in hodoscope with eight counters in the first layer and nine in the second layer. The first layer was shifted by half the width of a counter with respect to the second layer. The height of these counters are the same while the width gradually decrease towards the

Table 3.3: Dimensions of the hodoscope in Fd [138].

Counter	Height[mm]	Width[mm]	Thickness[mm]
I_1	360	40	15
I_2	360	60	15
I_{3-8}	360	80	20
II_1	360	40	15
II_2	360	50	15
II_3	360	60	15
II_{4-9}	360	80	20

beam pipe, where higher counting rates are expected. The dimensions of counters in hodoscope are shown in Table 3.2.3.

3.3 Targets

Since ANKE is an internal target experiment in one of the straight sections of COSY, the space is rather limited for the target chamber. Moreover, the target thickness had to be small enough in order not to decrease the beam intensity significantly but on the other hand it had to be large enough in order to provide high event rates. These constraints ruled out the possibility of gas-jet targets and solid targets, and led to the decision to a hydrogen cluster-jet target [139] for pp collisions as shown in Fig. 3.7. The target consists of three major parts: the cluster source, the scattering chamber and the beam dump. The pre-cooled gas, which passes through a Laval-nozzle, is peeled off the cluster flow by the skimmer and two further collimators. Between the two collimator stages, another conical aperture with a diameter of 900 μm is placed in order to define the cluster beam diameter and hold back residual gas. The remaining homogeneous clusters with a small angular divergence cross the scattering chamber and reach the three-stage beam catcher. Finally, cluster beams with homogeneous volume density and well defined beam dimensions can be prepared for interactions with circulating accelerator beams. A typical target density in the scattering chamber

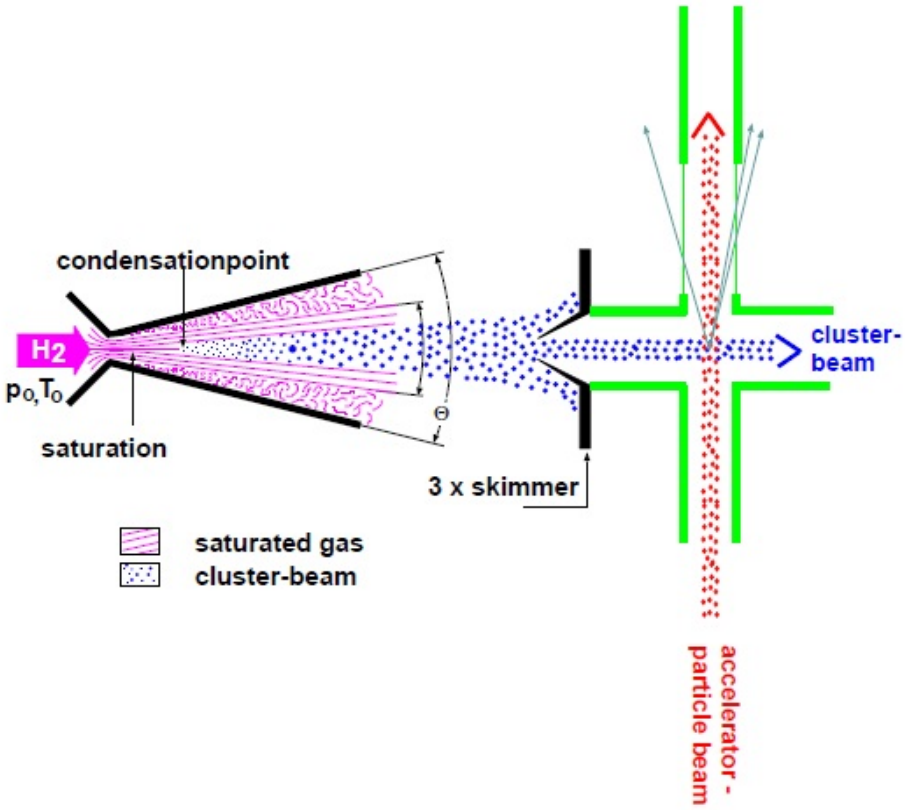

FIGURE 3.7: Schematic drawing of the principle for the hydrogen cluster target used in experiments for *pp* collisions at ANKE [139].

is about 10^{14} atoms/cm^3. The density of the target can be changed by adjusting the nozzle temperature or the gas input pressure. The complete system can be controlled manually or automatically by an IEEE-488 bus via a VME system [139].

On the other hand, thin strips of solid target material [132] have been used for nucleon-nucleus reactions as shown in Fig. 3.8. The strips typically have triangular shapes with dimensions of 2 mm (width at base) and 20 mm in the length. Several targets can be inserted simultaneously into the target chamber so that comparative measurements can be performed without breaking the target system.

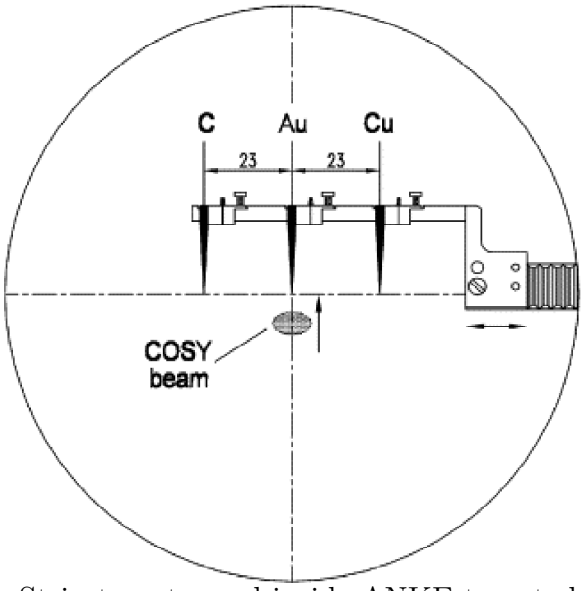

FIGURE 3.8: Strip targets used inside ANKE target chamber [132].

3.4 Electronics and data acquisition system

Digitization of signals from the scintillation counters is performed with CAMAC (FERA), FASTBUS QDC and TDC modules [132]. All scintillator counters are read out at both ends via photomultipliers, which provide both amplitude and time information. The structure of an individual scintillator readout channel is presented in Fig. 3.9. The precise time information from the counters is achieved by constant fraction discriminators (CFD) and mean timers that generate the hardware mean of the time signals of both photomultipliers. A typical time resolution in the mean timer for STOP counters is on the order of 50 ps. Moreover, the vertical spatial information in each scintillator is obtained from the time difference of phototubes at both ends. The spatial resolution for most of the STOP counters is better than 30 mm.

For the side detection system, it is possible to set a common TOF gate (with length variable from 3 to 23 ns) in coincidence with up to 16 individually adjustable START-STOP combinations by using specially built VME-modules [140]. In this way

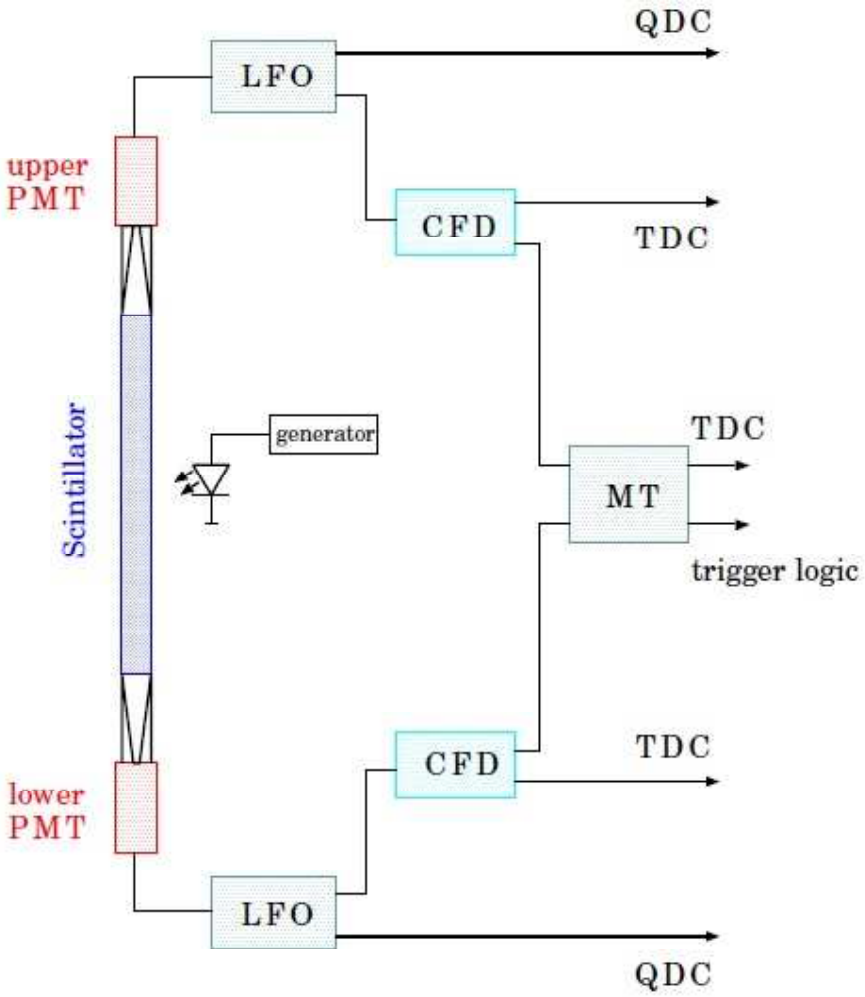

FIGURE 3.9: Scheme for scintillator counters read-out system.

corridors of acceptable START-STOP combinations can be defined through which the charged particles produced from the specified reaction should pass. Sixteen VME modules are required for the online TOF trigger which allows to select pions, kaons or protons during data taking. Based on the mean timer information and the START-STOP combination, these trigger modules decide within 100 ns whether an event is accepted or not. The readout of the MWPCs is performed using a highly integrated front-end system based on two chips which were developed at the Rutherford Appleton Laboratory (RAL) [141].

The readout of the forward scintillators is the same as the side system. A trigger

signal was generated when both layers of the hodoscope were hit, which can help reduce the combinatorial background.

The multi-crate data acquisition system (DAQ) supports the standard readout systems CAMAC, FASTBUS and VME [142], which is designed to meet the requirements of ANKE, e.g. recording of high event rates. For a total trigger rate of 10 kHz, approximately 50% of the events are written on tape. The collected data are then transmitted in clusters of sub-events via a Fast-Ethernet connection to the event builder and written on tape using a fast DLT tape drive [140]. In order to ensure the correctness of every event, each readout system employs a synchronization module that was developed for this purpose. These modules are interfaced by a ring-like bus system. The parallel readout system is scalable over a wide range and supported by an extensive body of software. The software enables interactive communication with the individual subsystems, which is particularly useful during commissioning and for general diagnostic purposes.

4

Data Analysis

The software package RootSorter [143] was used for data analysis, which is based on the ROOT framework [144]. One can use RootSorter to preselect raw data by applying rather loose cuts on TOF gates in Pd for different types of particles. The determinations of the TOF gates for protons relies on the TOF information measured from START-STOP combinations. While the TOF information is insufficient to identify the gates for K^+. A dedicated system using the so-called decay VETO technique was developed to provide corresponding K^+ TOF gates in different combinations of START-STOP counters. It should noted that this criterion is not used in the final analysis since it reduces the statistics significantly.

After the pre-selection stage, the reduced data were then analyzed to identify final particles and therefore interested reaction channels. In ANKE, particle identification relies on the momentum reconstruction and TOF measurements. One can easily identify π^+, K^+ and proton in the Pd system, but due to the rather limited space, the time resolution in Nd is insufficient to separate kaons and pions. Instead, TOF calibrations for correlated charged particle pairs between $Pd - Nd$ system are

adopted. Meanwhile, TOF calibrations are also applied in $Pd - Fd$ system for K^+ identifications. Therefore, a triple coincident detection is performed with one particle in Pd, one in Fd and the third particle in Nd. For example, in the $pp \to ppK^+K^-$ reaction, the K^+p and K^-p pairs can be identified with K^+ in Pd, proton in Fd and K^- in Nd. Using a missing mass technique, the ppK^+K^- final states can be identified with a small amount of background. The similar processes have also been applied to the $pp \to pK^+\Lambda$ reaction.

In this chapter, the particle identification methods including TOF measurements and momentum reconstruction are described in details. The detection and trigger efficiencies are also discussed, followed by luminosity determinations using two different methods.

4.1 Running conditions

The experiments discussed in this thesis were performed at COSY-ANKE with different beam energies in 2004 (pp), 2007 (pA) and 2008 (pp). The corresponding experimental conditions are listed as:

- **Beam energy:** pp collisions at $T_p = 2.83$ GeV @ 2004 and $T_p = 2.57$ GeV @ 2008. pA collisions at $T_p = 2.83$ GeV @ 2007.
- **Target:** a high density hydrogen cluster-jet gas target and solid strip targets for pp and pA collisions, respectively.
- **Magnetic field:** D2 magnet field B = 1.57 T.
- **Trigger:** different triggers in parallel.

During the experiments, three different triggers were recorded simultaneously: T1 (a three-particle trigger, which requires events to register simultaneously in Pd,

Nd and Fd), T2 (a one-particle trigger with pre-scaling factor, which requires events to be detected in the Fd system) and T3 (a scaler trigger, which records beam related quantities). In some experiments, due to high events rates, particles were required to pass through certain TOF gates in order to generate a trigger T1 (no such requirement for the experiment performed at $T_p = 2.57$ GeV in 2008). The trigger T1 allows a triple-coincidence detection of the four-body final states. The trigger T2 was used for luminosity determinations based on the proton-proton elastic scattering method, as discussed in sec. 4.6. Due to the high count rates of pp elastic events, T2 was pre-scaled by a factor of 999. This scaling factor will be taken into account in the analysis in order to obtain the correct event counts.

4.2 Data Preselection

The huge amount of data collected during experiments were first preselected by rejecting scattered backgrounds and accidentals. Then loose cuts were applied on the START-STOP TOF gates in order to select specific particles. For example, positively charged particles that produced from the $pp \rightarrow ppK^+K^-$ reaction and detected in a range of simulated kaon peak position $\pm$ 30 channels are considered as kaon candidates. The peak positions were found with the procedure using delay VETO technique described in sec. 4.3. Since the TOF resolution in Pd is $\Gamma(FWHM) \approx$ 15 channels that corresponds to 675 ps, more than 99 % of kaon events are selected by applying those cuts. The raw data size was reduced by $\sim$ 75% after this finer cut for kaons in the data pre-selection step. For negatively charged particles, similar cuts of the range of peak position $\pm$ 30 channels are also applied. All cuts will be checked later on with clean events.

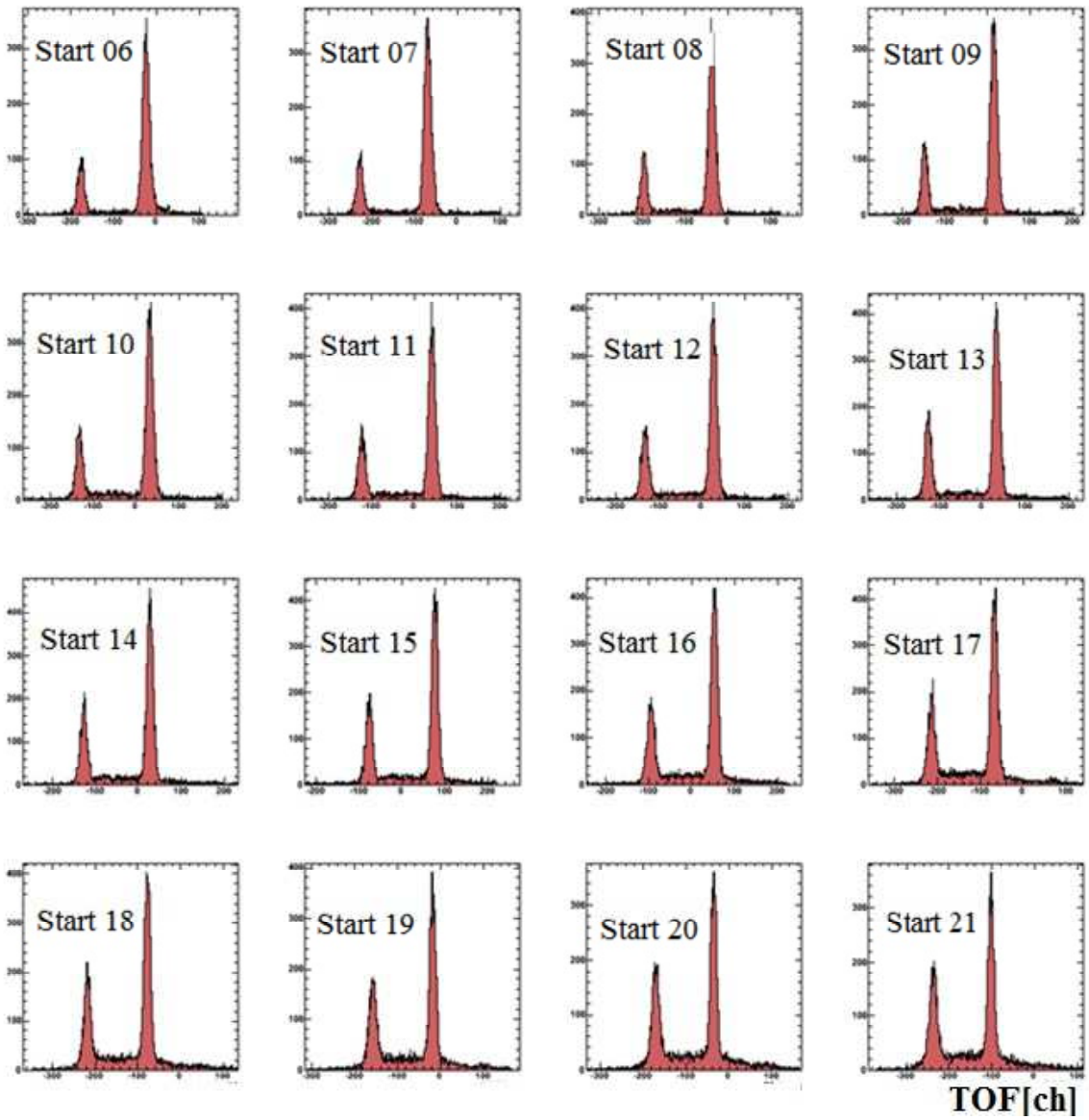

FIGURE 4.1: Individual time-of-flight spectra between STOP counter 13 and all the available START counters.

4.3 Particle identification

The preselected data were stored into a separate ROOT file for further analysis including particle identification and luminosity determination. In COSY-ANKE, particle identification relies on TOF measurements and momenta reconstruction. The selections vary for different types of particles. For example, positive kaons

were selected by a dedicated K^+ detection system using TOF information between the START and STOP counters in the Pd system. The selection of protons only relies on the TOF information in Pd. While the identification of K^- required TOF correlations between STOP counters in the Pd and Nd system.

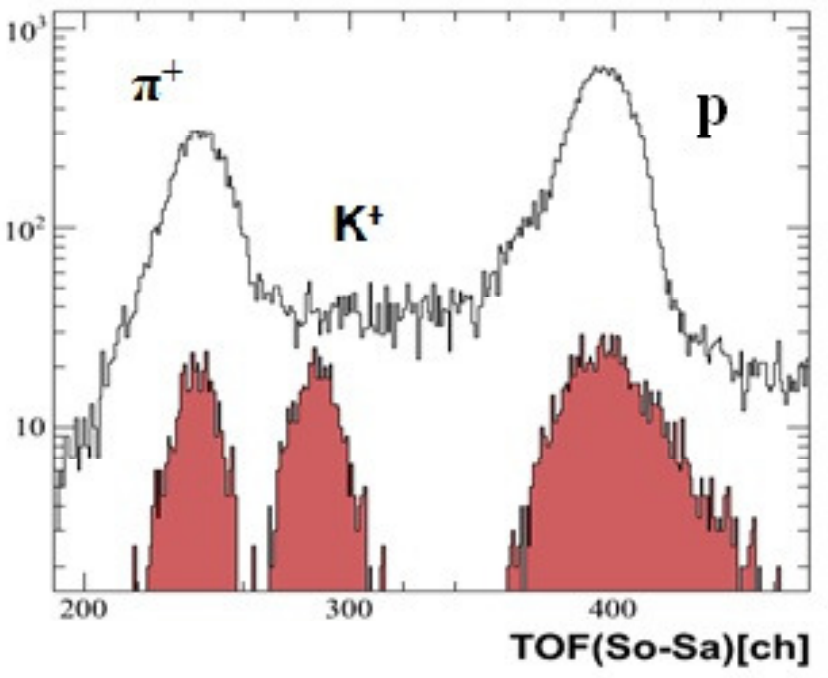

FIGURE 4.2: Summed TOF over all START-STOP combination.

4.3.1 Time of flight

One of the most important criteria for particle identification for the ANKE spectrometer is the particle TOF information [132, 145]. During data taking an open TOF trigger was chosen such that pions, protons and kaons are selected. Fig. 4.1 shows a typical TOF spectra for different combinations of START counters and the STOP counter 13 in the Pd system. As shown in the figure, most spectrum show two distinct peaks for protons (right) and pions (left) that were produced from the

target region. The combined TOF distribution for STOP counter 13 is shown in Fig. 4.2. It is clear that there is a non-negligible amount of background, which is mainly caused by fast protons emitted from the target at small angles. These protons would hit the pole shoes of D2 or the vacuum chamber and produced secondary particles. These particles were then detected by STOP counters in Pd resulting in a broad background distribution in TOF spectra since they did not have well defined momenta. The background can be suppressed by applying vertical angle cuts, see sec. 4.3.2 for details.

In principle, the observed time resolution is sufficient to discriminate the pions (protons) and kaons, since the TOF difference (peak-to-peak) between these ejectiles is $\sim 8\sigma$. However, due to a large amount of produced π^+s that can be up to three orders of magnitude higher, kaon peaks are not visible in the TOF spectra. Thus, a dedicated system for K^+ detection was designed for separating kaons from the pions background [132, 145].

As mentioned before, fifteen telescopes were mounted on the focal plane of ANKE with each telescope consisting of one STOP counter, one Cerenkov detector, two copper degrader (I,II), one ΔE, and one veto counter. The STOP counters combined with several START counters are used for TOF measurements. The degrader I is used for stopping protons originating from the target and slowing down kaons such that they are stopped in the ΔE counter or in degrader II. This results in a large K^+ energy loss in the ΔE counter which helps to separate them from pions and scattered protons. The tapered shape of degrader I accounts for momentum dispersion along the focal surface of D2: From the left to the right edge of each telescope the degrader thickness increases in correspondence with the ejectile momentum. In order to minimize the spread of kaons, each telescope is positioned such that the first degrader is located in the focal plan where the momentum spread is the smallest. Pions pass through the counters and degraders almost unaffected due to high velocity and result

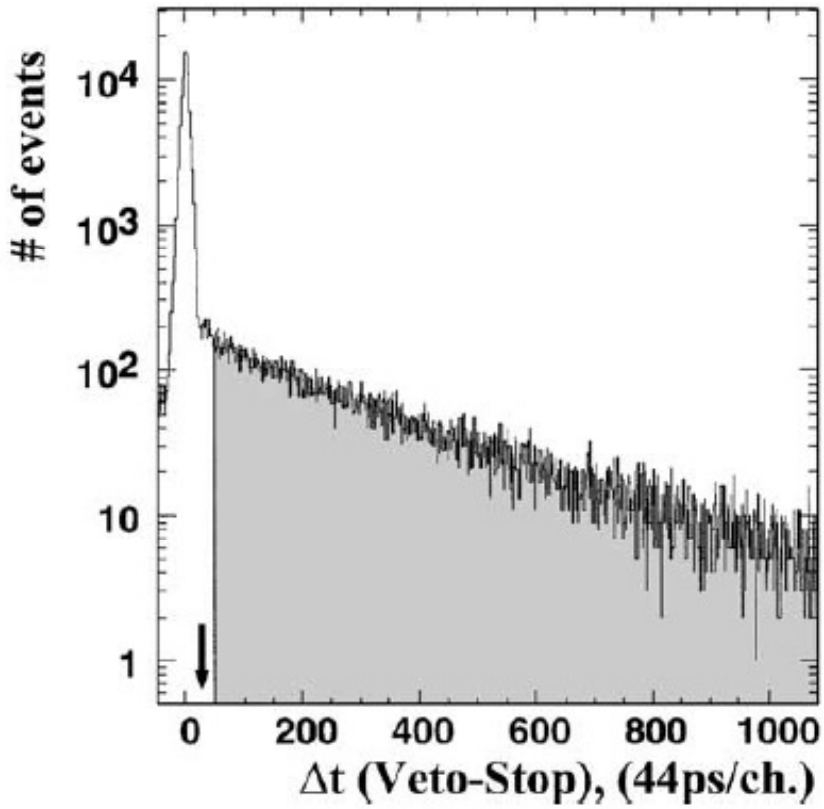

FIGURE 4.3: Time difference between detection of particles in veto and stop counters of telescope 13. The arrow shows the cut used during the measurements where the off-line cut is indicated by the shaded area.

in small energy losses in all counters. While Kaons that stopped in the ΔE counter or degrader II decay with a lifetime of $\tau = 12.4$ ns via $K^+ \rightarrow \mu^+ v_\mu (BR = 63.54\%)$ or $K^+ \rightarrow \pi^+ \pi^\circ (BR = 20.68\%)$. The decay products μ^+ and π^+ which were emitted isotropically can reach the veto counter and produce signals with a characteristic delay with respect to the signals in the STOP or ΔE counter. This provides an additional criteria for K^+-identification which becomes particularly important for low energy beams. The distribution of the time difference between veto and STOP counters of Telescope 13 is shown in Fig. 4.3. One can clearly see a prompt peak from particles directly passing through the second degrader (pions and secondary

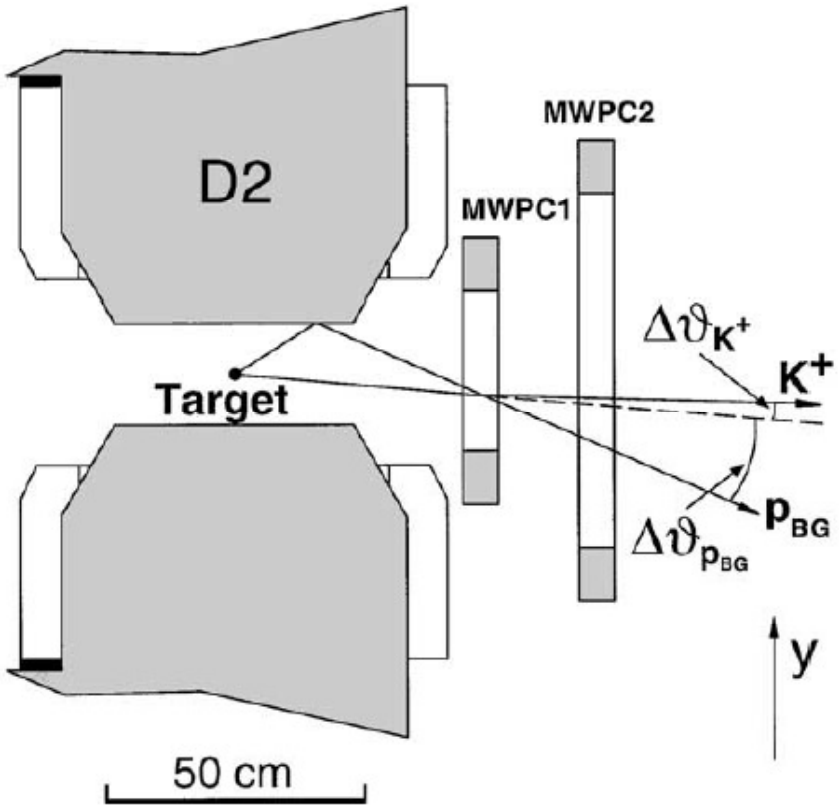

FIGURE 4.4: Ejectiles from the target and scattered background particles in general have different vertical angles behind the spectrometer.

protons). In addition, there are delayed events visible which can be attributed to the decay products of K^+-mesons stopped in the second degrader. An exponential fit to the time distribution in the veto counters yields a value of $\tau = 12.0 \pm 0.3$ ns, which is consistent with the expected value of 12.4 ns. After applying this criterion, the peak positions and widths of kaons using TOF are clearly identified. The shaded area in the sum spectra in Fig. 4.2, shows the time distribution of particles after applying cuts based on the delayed VETO technique.

4.3.2 Background suppression

The most problematic background is caused by secondary particles produced on the pole shoes of D2 or in the vacuum chamber. To suppress those backgrounds, several

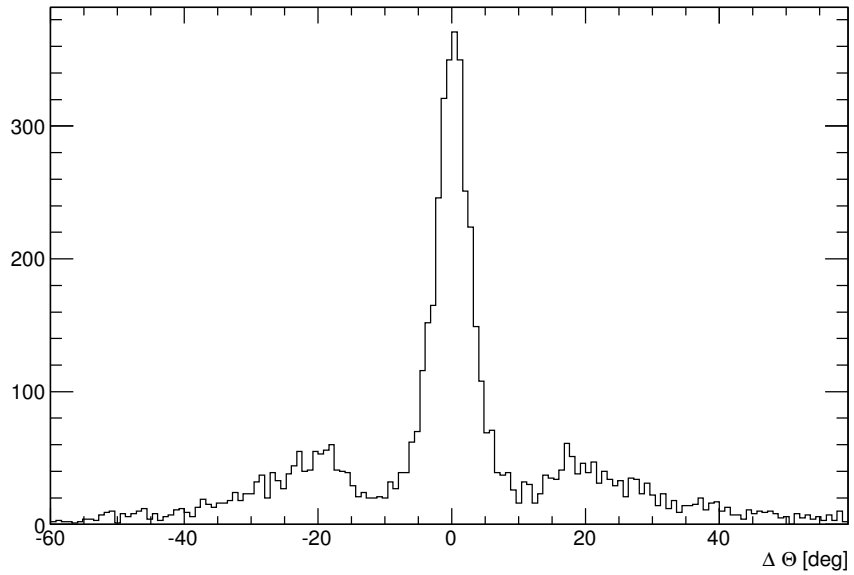

FIGURE 4.5: Vertical angle distribution measured with the two MWPCs after applying the K^+-cuts in the scintillator spectrum. The spectrum show a clear peak of kaons originating from the target. Background from scattered particles is also visible.

finer cuts are introduced in the analysis: a target vertex cut, vertical and horizontal angle cuts. The principle of the vertical angle cut [145] is illustrated in Fig. 4.4. As indicated by the dashed line in the figure, particles from the target within the angular acceptance of ANKE passing through the first MWPC at vertical coordinate y are expected to have a certain vertical angle θ. These ejectiles may undergo multi-scattering inside the detection system and cause some smearing $\Delta\theta_{K^+}$ (for kaons). In contrast, scattered particles P_{BG} in general have larger angular differences $\Delta\theta_{p_{BG}}$. Thus, the vertical information of MWPCs can be used for effective suppression of scattered particles. Fig. 4.5 shows a vertical angular distribution for K^+. There is a clear peak corresponding to ejectiles from the target after applying all cuts in the scintillator counters. The background under the peak was then subtracted. Thus the vertical MWPC information is very efficient for the suppression of scattered particles.

Moreover, scatterings inside the MWPCs are neglected during the track selection.

In addition to the cuts on vertical distributions [132], finer cuts are also applied in the horizontal direction. In the horizontal cuts, events are only accepted if responding wires are inside a corridor defined by trajectories connecting the edges of the individual START and STOP counters. Therefore, the good tracks must hit a certain combination of START-STOP counters in the side system. This criterion can further suppress scattered backgrounds, accidental coincidences and chamber noises.

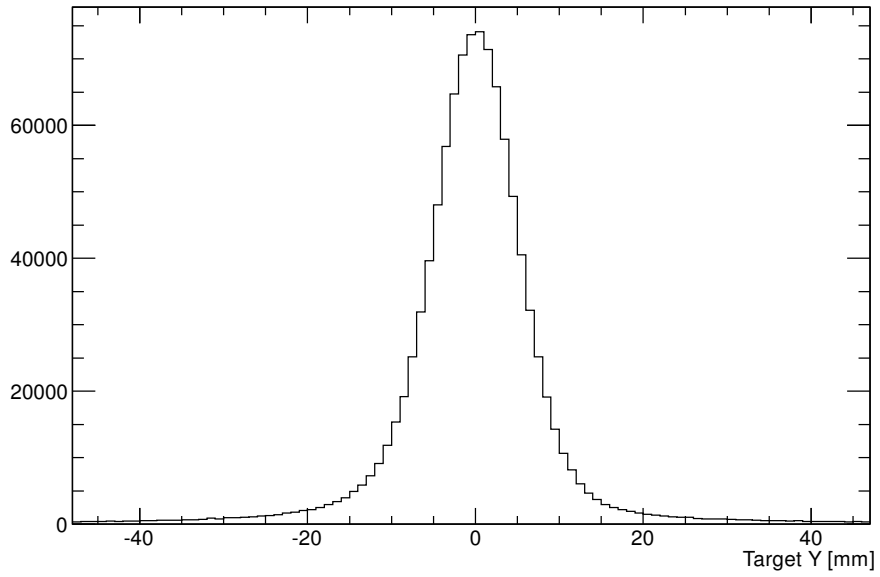

FIGURE 4.6: Target distribution in Y direction.

On the other hand, the coordinates of generated particles in Y direction (perpendicular to the reaction plane) should lie within a Gaussian shaped peak while the background is uniformly distributed. With the recorded coordinates from MWPCs, one can reconstruct the track coordinates in the target region and apply a finer cut for background rejections, as shown in Fig. 4.6. For tracks registered in the forward detector, the crossing point for tracks at the exit window must be in the active region.

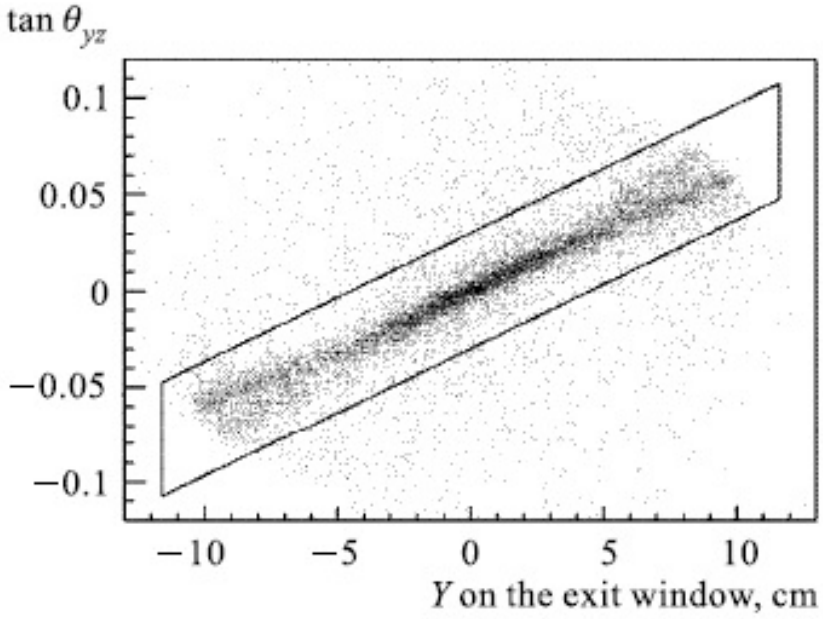

FIGURE 4.7: Correlation of the track parameters in the YZ plane.

Thus, standard cuts on the coordinates of the track intersection with the forward window were also applied to reject scattered background events [138]. In addition, a correct correlation of the track parameters in the YZ plane is also required to suppress the background. A typical experimental distribution of the track parameters in the YZ plane is shown in Fig. 4.7, the projection of the whole trajectory onto the YZ plane is close to the straight line crossing the beam-target intersection area.

4.3.3 Momentum reconstruction

The momenta of ejectiles can be reconstructed based on track information and the measured three-dimensional D2 magnetic field. A number of momentum reconstruction algorithms have been adopted for the ANKE detection system, such as the box-field approximation, polynomial approximation and the Runge-Kutta method.

The box-field approximation was used during the preselection of the raw data. In this approach the magnetic field of D2 is assumed to be homogeneous in a box

with effective width and length in an effective region. The trajectory of a particle inside the magnetic field is defined by the Lorentz force. In addition, the trajectory is assumed to be a straight line when the particle has left the field. The out-going vertical and horizontal angles that derived from MWPCs in the side systems are used to calculate the momentum components. Under these assumptions, the effective length of the box-field is calculated from the field strength, the beam momentum and the deflection angle of the ANKE spectrometer. On the other hand, the effective width is determined from the experimental data using $pp \to pK^+\Lambda$ as a calibration reaction [146]. In the calibration, a K^+ and proton were selected in one of the side detectors. The K^+ and proton momentum components have been determined using the box-field method with an assumed effective width. The effective width was then tuned to make sure that the missing mass of pK^+ be consistent with Λ. The achieved momentum resolution for particles detected in the side system is $\sim 2\%$ (FWHM).

The polynomial method has been developed for fast determinations of momenta for the forward detection system. Each component is approximated by a third-order polynomial of the four track parameters $\vec{T}$ $(tan(\theta_{xz}), tan(\theta_{yz}), x_w, y_w)$, where θ_{xz} and θ_{yz} represent the projection angles on the XZ and YZ planes, respectively, while x_w and y_w are the coordinates of the track on the D2 exit window. The polynomial coefficients are determined by a teaching sample of events, produced by a GEANT-based simulation [147, 138]. The sample is generated for every combination of the magnetic field value, beam direction and target position. The accuracy of the reconstruction method was studied on a set of simulated events obtained without smearing by multiple scattering, MWPC coordinate resolution, and the size of the beam-target overlap. The uncertainty of the reconstructed momentum due to uncertainties in the input data lies below 0.1%, which is confirmed by the measured resolutions for elastically scattered protons. The achieved momentum resolution for particles detected in Fd is $\sim 1\%$.

In the final analysis the Runge-Kutta method is adopted for the best accuracy of the momentum reconstruction for both the side and forward detection systems. In this method, the Lorentz force is solved using the Runge-Kutta algorithm. Moreover, the energy loss corrections are considered in every step. For fast calculations, the initial parameters for the Runge-Kutta method are taken from the box-field approximation.

4.3.4 TOF calibration

As mentioned before, due to the limitations of the experimental setup, the measured time resolution between Nd START-STOP counters is $\sim$ 1 ns, which is insufficient to differentiate between π^- and K^- with momenta above 500 MeV/c. However, the TOF difference between π^- and K^- from the target to the Nd STOP counters are in a range from 1.8 to 5 ns with the achieved time resolution of $\sim$ 550 ps, which is sufficient to separate K^- from the π^- background.

In order to obtain the TOF calibrations of PdNd, $\pi^+\pi^-$ events were collected during the experiments. A trigger was set such that the start signal for the TDC is always derived from the Pd STOP counter. The positive and negative pions are selected by using TOF information from START-STOP counters. The momenta of pions are then determined using the hits positions from MWPCs and the polynomial method. The corresponding TDC difference between π^+ and π^- is denoted as ΔTDC. On the other side, the TOF difference expected for a $\pi^+\pi^-$ pair t_{tof} can be calculated based on their measured momenta and path lengths from the target to STOP counters. The TOF calibration was done by assuming that:

$$\Delta t_{tof} = a \cdot \Delta TDC + b \tag{4.1}$$

The parameter a and b can be obtained by fitting experimental distributions for each combination of PdNd STOP counters, as shown in Fig. 4.8. These parameters

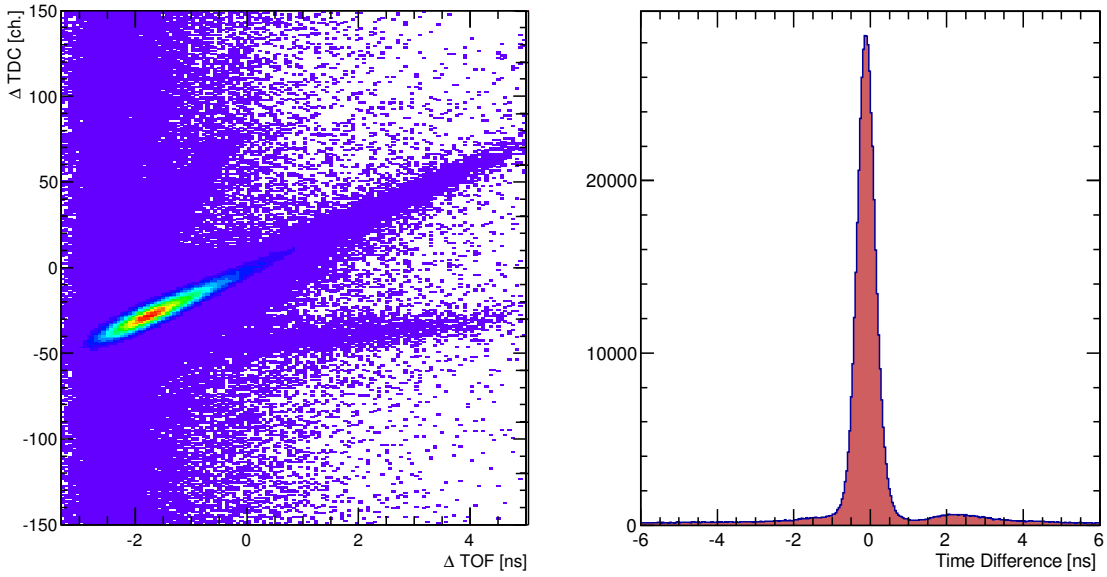

FIGURE 4.8: Right: TDC value versus the calculated time difference between NDS and PDS for one STOP-STOP combination using the momentum information from $\pi^+\pi^-$ pair. Left: The sum of all normalized TOF difference of the Pd and Nd STOP counters is shown.

are stored and later used for calibrating TDC values and identifying the correlated events, such as K^+K^- pairs. The same technique has also been applied to the forward detection system: the TDC calibration for PdFd can be done by selecting π^+p events with proton in Fd and π^+ in Pd system.

4.3.5 Correlations

After the TOF calibrations for all possible combinations of STOP counters in Pd, Nd and Fd, one can identify the correlated particle pairs, i.e. K^+K^- and K^+p pairs. Given the established TOF calibration parameters a and b, the TDC difference of a K^+ and a proton can be converted into time information. Firstly, assuming that these two particles were detected in the Pd and Fd system, respectively, the TOF difference of K^+p pairs can be calculated based on tracks length and reconstructed particle momenta. Based on this information, good events must be lying in a region where

these two time differences are consistent, as shown in Fig. 4.9a). The projection of the time difference is shown in Fig. 4.9b), in which the prompt peak is the corresponding K^+p pairs signals. A 3σ cut was applied to this time difference in order to reduce the misidentified K^+p events. The same technique was also applied for selecting K^+K^- pairs and other correlated events.

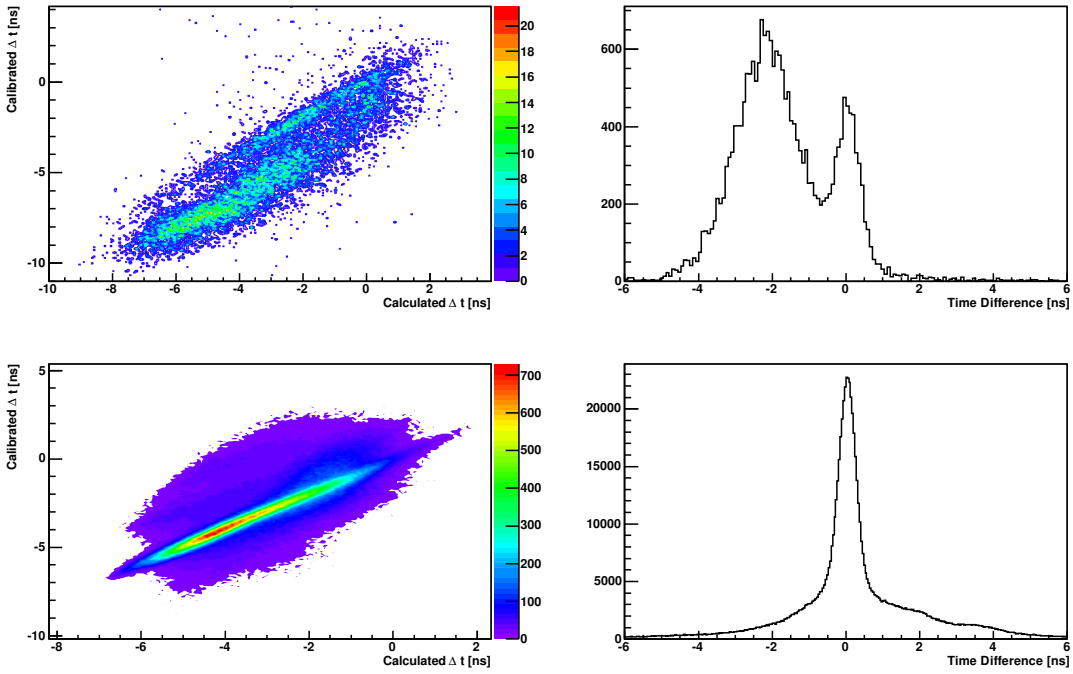

FIGURE 4.9: The left column shows: the TOF differences between the STOP counter in the negative as well as in the forward detector system with respect to the positive STOP counters versus TOF calculated using momentum information under the assumption that the detected particles are K^+K^- and K^+p. The right column shows its projection where clear separation between this pair can be performed.

4.4 Reaction identification

4.4.1 The $pp \to pp\phi/K^+K^-$ reaction

After identifying the correlated pK^+ and pK^- pairs (with K^+s in Pd, protons in Fd and K^-s in Nd), a triple-coincident detection of a K^+K^- pair and a forward-going

protons can form a missing mass distribution of K^+K^-p:

$$M_x^2 = (P_\gamma + P_p - P_{K^+} - P_{K^-} - P_{p'})^2 \tag{4.2}$$

where P_γ and P_p are the 4-momenta of the beam and target, respectively. P_{K^+}, P_{K^-} and $P_{p'}$ are the 4-momenta of the detected final states. The obtained missing mass distributions of K^+K^-p are shown in Fig 4.10 and Fig 4.11 at two different energies, which show a clear peak around the proton mass. In order to obtain ppK^+K^- final state, a 3σ cut was applied in the missing-mass distributions. However, there are still non-negligible amount of misidentified events inside the $\pm 3\sigma$ cut window around the proton mass, which were subtracted using weighted data from the side bands, as parametrized by the solid line in Fig. 4.10 and Fig 4.11. The corresponding background is estimated to be about 11.5% (2.83 GeV) and 5% ($\sim$2.57 GeV) using a second-order polynomial fit. Any ambiguity in this procedure is less than 3% and considered as a source of systematic uncertainties in the data analysis.

After identifying the ppK^+K^- final state, the separation of non-ϕ kaon pair and the ϕ meson production can be achieved by applying a 3σ cut on the invariant mass of the ϕ meson, further discussions can be found in sec. 6.2.

4.4.2 The $pp \to pK^+\Lambda$ reaction

Following the similar procedures for the $pp \to ppK^+K^-$ reaction, one can also identify the $pp \to pK^+\Lambda$ reaction. The Λ particle is identified via its decay products p and π^-. As a first step three charged particles in the final state (p_1, K^+, p_2, π^-) can be identified by the techniques described in previous sections. After identifying the final state particles, one needs to assign the right proton to the Λ decay. Since two protons occur in the final state, it is not known in the first place, which proton originally stems from the decay of the intermediate state Λ. In the analysis, both the invariant masses of π^-p_1 and π^-p_2 are formed. An 3σ cut on the peak around 1115 MeV is

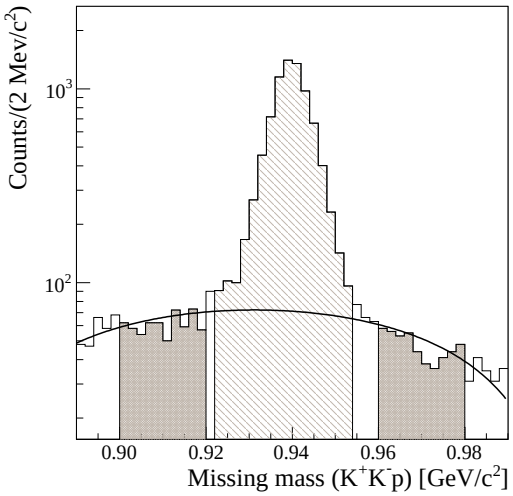

FIGURE 4.10: The pK^+K^- missing-mass distribution in the $pp \rightarrow pK^+K^-X$ reaction at $T_p = 2.568$ GeV. The hatched histogram shows the cuts imposed for the selection of the non-detected proton. The solid line, which is a second-order polynomial fit, was used to estimate the background contribution under the proton peak.

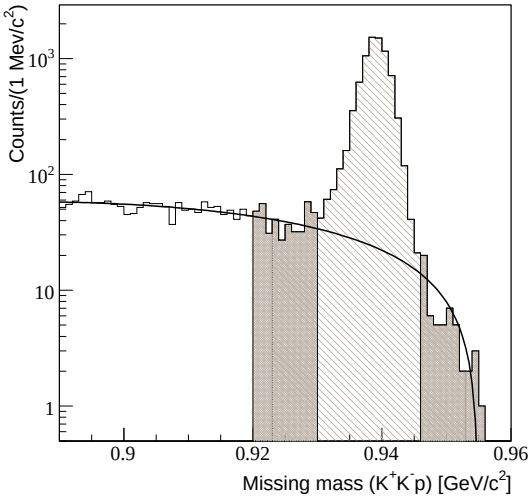

FIGURE 4.11: The pK^+K^- missing-mass distribution in the $pp \rightarrow pK^+K^-X$ reaction at $T_p = 2.568$ GeV. The hatched histogram shows the cuts imposed for the selection of the non-detected proton. The solid line, which is a second-order polynomial fit, was used to estimate the background contribution under the proton peak.

applied to differentiate the Λ events from the direct $\pi^- p$ productions. Based on the detection systems and triggers involved during the measurements, there are three different configurations that form the final state of $pK^+\Lambda$ with π^-s registered in Nd:

- **case 1:** Protons in Pd, and Protons in Fd.
- **case 2:** K^+s in Pd, and Protons in Fd.
- **case 3:** Protons in Pd, and K^+s in Fd.

The corresponding missing mass distributions are shown: in case 1, the missing mass of the $p_1 p_2 \pi^-$ system is shown in Fig. 4.12, which should be consistent with the mass of K^+. While in case 2 and 3, the missing masses of the $pK^+\pi^-$ system are shown in Fig. 4.13 and Fig. 4.14, respectively. In both figures, the peak in the missing mass distributions is consistent with the mass of proton.

After applying 3σ cuts on the missing mass distributions, one can identify the $pp\pi^+\pi^-$ final states. However, in order to study the Λ production, an additional requirement that the invariant mass of $p\pi^-$ should be consistent with Λ mass is required. This requirement removes a large amount of background, which may come from the direct production process $pp \rightarrow ppK^+\pi^-$. The background contribution under the missing-mass peak is estimated from the side-band events, the same as the analysis of the ppK^+K^- final state.

4.5 Efficiency

The efficiencies are crucial to determine the real number of events produced from the reactions of interests, and thus the differential cross sections and total cross sections. In the analysis, two kinds of efficiency are considered: detection efficiency including scintillator efficiency and tracking efficiency in MWPCs and trigger efficiency in the DAQ system.

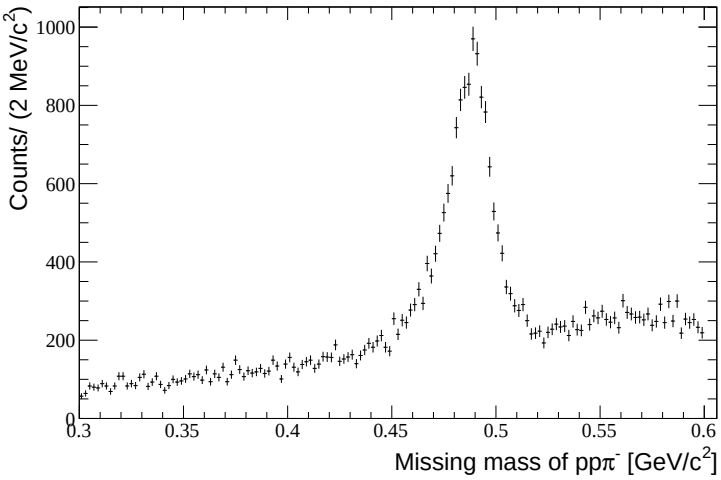

FIGURE 4.12: (Preliminary result) The $pp\pi^-$ missing-mass distribution in the $pp \to pK^+\Lambda$ reaction at $T_p = 2.568$ GeV in Case 1.

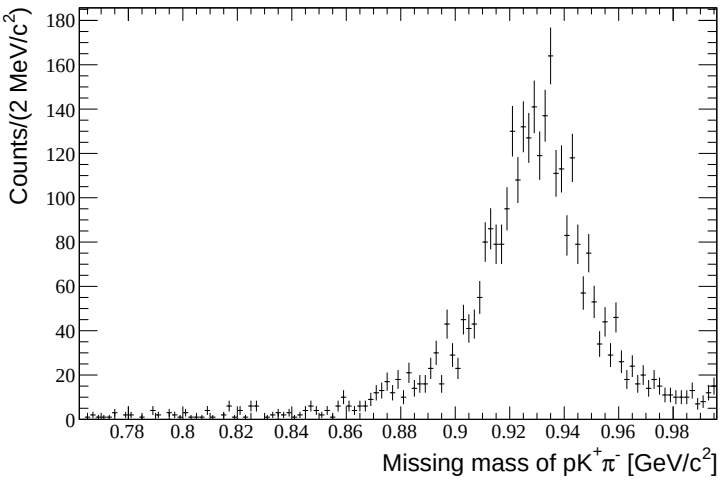

FIGURE 4.13: (Preliminary result) The $pK^+\pi^-$ missing-mass distribution in the $pp \to pK^+\Lambda$ reaction at $T_p = 2.568$ GeV in Case 2.

4.5.1 Scintillator efficiency

The detection efficiencies for pions and kaons in the scintillator counters can be determined by fitting the energy-loss spectra with Landau distributions. It is found that the detection efficiency for pions is larger than 99%. And the detection efficiencies for kaons are even higher and is about 100%, except for the thin START counters,

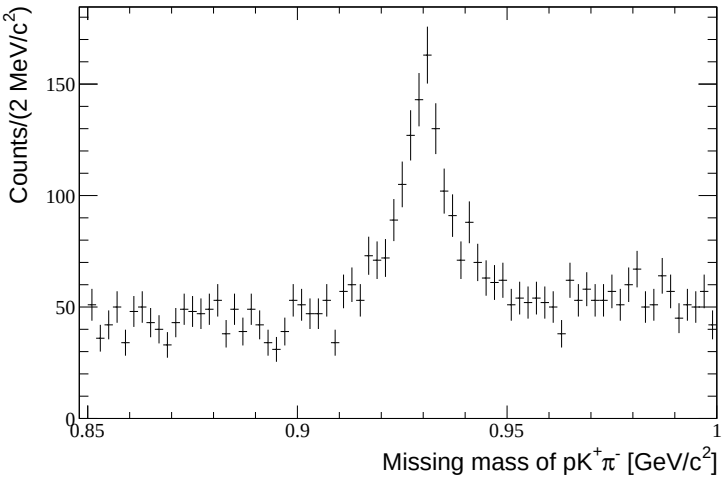

FIGURE 4.14: (Preliminary result) The $pK^+\pi^-$ missing-mass distribution in the $pp \to pK^+\Lambda$ reaction at $T_p = 2.568$ GeV in Case 3.

which were excluded from the analysis.

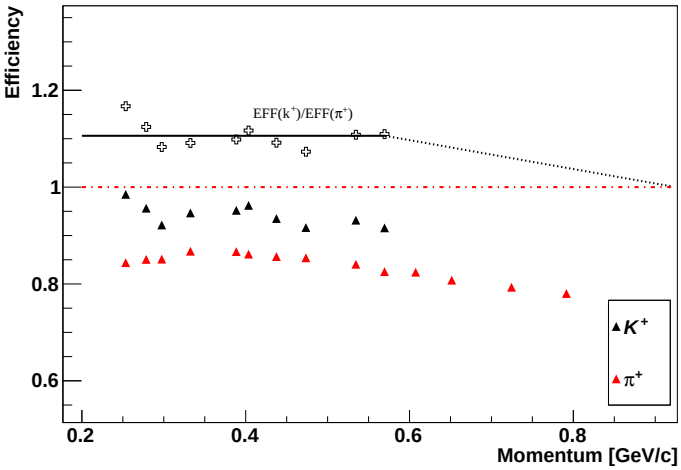

FIGURE 4.15: Detection efficiency for K^+ and π^+ and their ratio are shown.

4.5.2 MWPC efficiency

The tracking efficiency of a particle in the MWPCs depends on its type and momentum. Since the scintillator efficiency for kaons and pions is almost 100%, one can determine the tracking efficiency by the ratio of the number of a certain type

particle with tracks inside the chambers to the total number of particles detected by the START-STOP counters (and delayed-VETO for K^+):

$$\epsilon_{eff} = \frac{N_{tracks.in.MWPC}}{N_{START-STOP}} \tag{4.3}$$

The calculated tracking efficiency varies from 92 to 98 % and 80 to 90 % for K^+ and π^+, respectively. Following the same way, the tracking efficiency of π^- can be determined based on hits inside MWPCs, as shown in Fig. 4.15. However, it is impossible to extract the efficiency for K^- based on the START-STOP counters, since the measured time resolution is insufficient to differentiate between K^- and π^-. However, if we assume that the positively and negatively charged particles with the same momentum should have the same energy loss in material, the ratio of the detection efficiency $\epsilon_{K^+}/\epsilon_{\pi^+}$ as a function of momenta combined with π^- efficiency can be used to determine the K^- efficiency.

On the other hand, in the forward detection system the situation is different since there are no START counters. The detection efficiency is determined by the sensitive area of each plane, which is divided into 20 $\times$ 20 squares (2-3 cm in size). The efficiency in each square is then calculated using track information reconstructed from other planes [138] using $\epsilon_{i,j} = \frac{N_{without}}{N_{with}}$, where N_{with} and $N_{without}$ represent the number of tracks reconstructed with and without signal from the plane, respectively. In order to achieve reasonable statistics in each square, a large amount of experimental data are used in the analysis. It is found that the detection efficiency in the forward detection system is about 96%. The obtained efficiency map is shown in Fig. 4.16.

4.5.3 Trigger efficiency

In addition to the detection efficiency, the dead-time of the data acquisition also presents a correction for the total number of events. The trigger efficiency is deter-

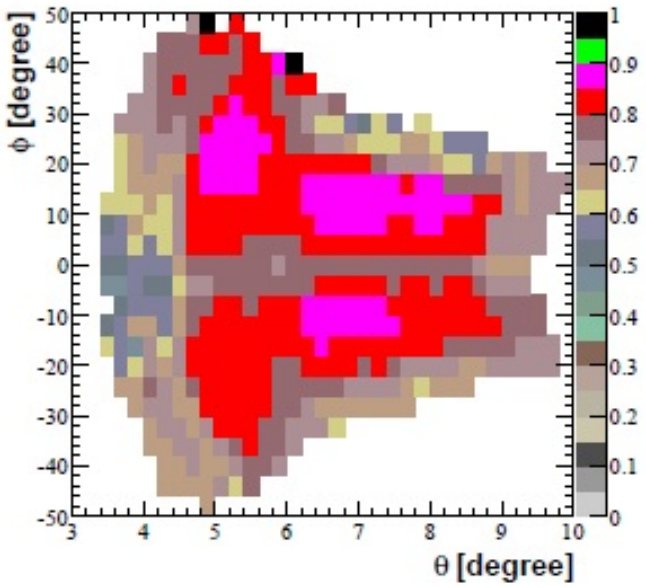

FIGURE 4.16: Efficiency map for the forward MWPCs.

mined by the ratio of the so-called trigger-in events T_{in} to the accepted events by the data acquisition system T_{out}. The efficiency of three-particle trigger T_1 is different from that of one-particle trigger T_2. Fig. 4.17 shows the trigger efficiencies in one run for trigger T_1 and T_2. Since the trigger rates were not stable during the experiments, the trigger efficiencies were corrected on a run-by-run basis.

4.6 Luminosity

In order to extract total cross sections, the absolute value of the integrated luminosity during the experiments must be determined. There are two ways to determine the luminosity: *pp* elastic scattering method and Schottky method. In the final analysis, the *pp* elastic scattering method was adopted to measure the luminosity, while the Schottky method was used as a cross-check.

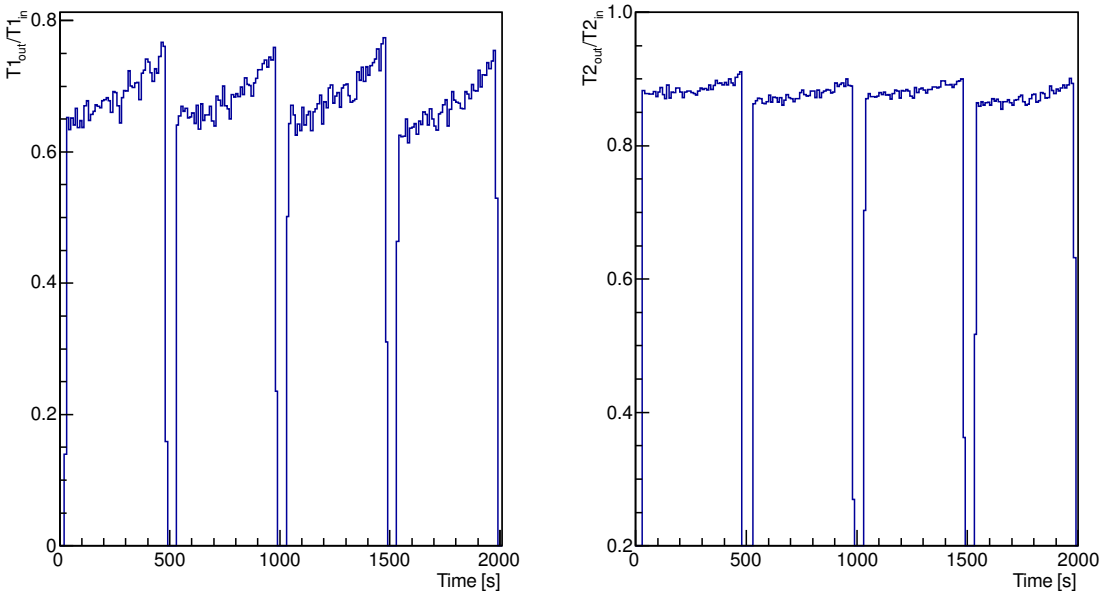

FIGURE 4.17: Trigger efficiencies for T_1 and T_2 are shown.

4.6.1 Luminosity determination via pp elastic scattering

The small angle *pp* elastic scattering is considered as a suitable calibration reaction for luminosity determination in COSY-ANKE [48, 63]. In this method, a forward-going proton that covers polar angles from 4° to 10° in the laboratory frame was detected in the Fd system. The *pp* elastic scattering then can be identified using the missing-mass technique that requires the missing-mass of the detected proton should be consistent with the mass of a proton. After background subtractions, the total number of detected *pp* elastic scattering events can be obtained. Finally, the elastically scattered events combined with the theoretical predictions of *pp* differential cross sections from the SAID solution [148, 149, 150], allow one to extract the luminosity by the following formula:

$$L = \frac{N_{tot}}{\int_{\Omega_{det}} \frac{d\sigma}{d\Omega} d\Omega} \tag{4.4}$$

where N_{tot} is the total number of pp elastic events identified in the forward detection system, $\frac{d\sigma}{d\Omega}$ is the differential cross section for pp elastic scattering from the SAID solution [148, 149, 150], while Ω_{det} is the solid angle of the forward detector.

However, due to the lack of data [151, 152, 153, 154, 155, 156] the SAID database overestimates the values in small angles ($< 10^{\circ}$) between 2.5 and 3 GeV [63]. In order to describe well the experimental data without introducing an overall scaling factor, a normalization option has to be taken into account [63]. In addition, the SAID program does not provide uncertainties. But the uncertainties have been estimated by R. A. Arndt [157] to be of a few percent level for our energies.

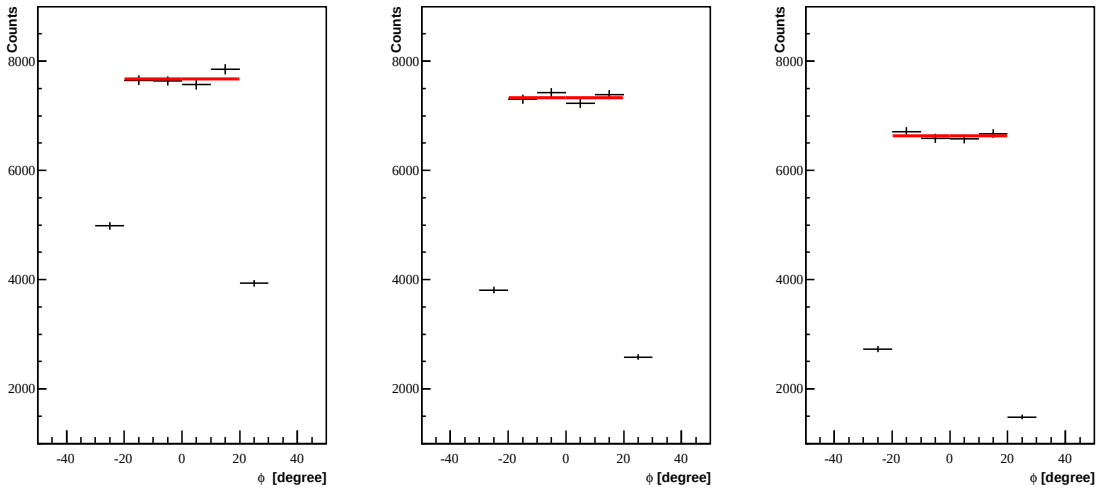

FIGURE 4.18: Detector edges in azimuthal angles.

In order to calculate the solid angle, the forward detector acceptance has been divided into several polar angle bins with a width of 0.5°. For each small bin the detector solid angle can be calculated as:

$$\Omega_i^{det} = \Delta\phi_i[cos\theta_i - cos(\theta_i + 0.5^{\circ})] \tag{4.5}$$

where $\Delta\phi_i$ is the range of azimuthal angles in which the event distributions are flat. The typical spectra for azimuthal angular distributions ($-20^{\circ} < \phi < 20^{\circ}$) are shown

in Fig 4.18.

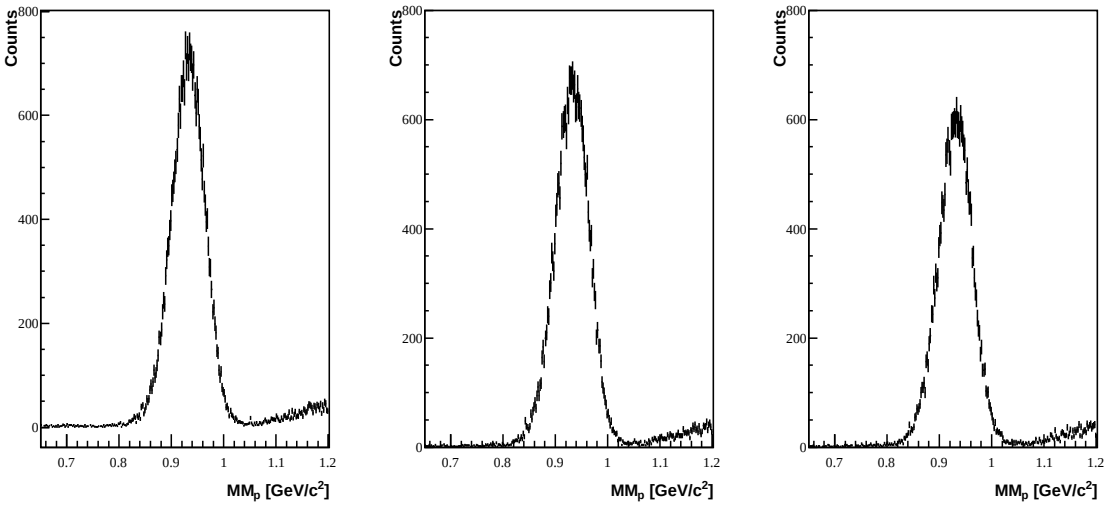

FIGURE 4.19: The proton missing mass spectra.

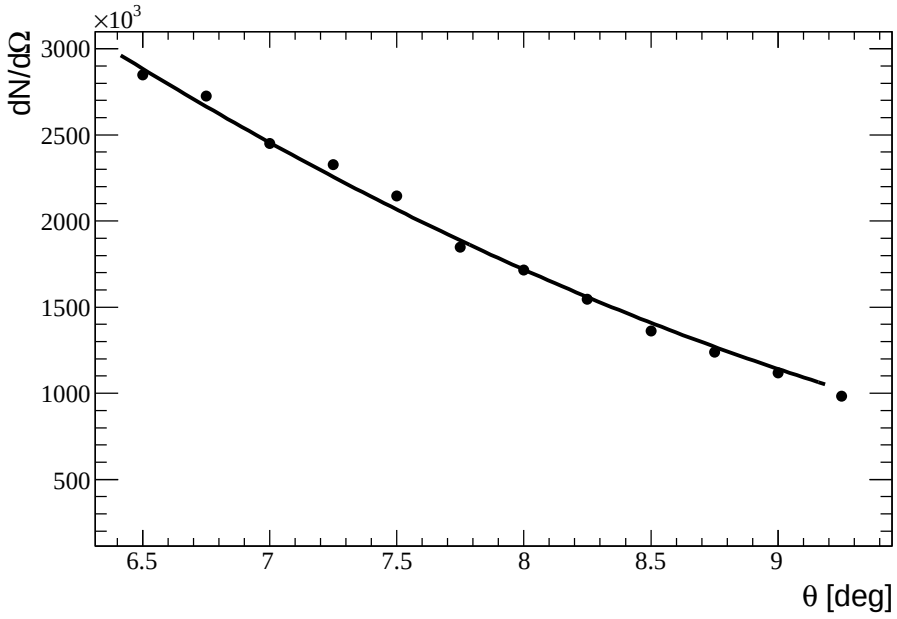

FIGURE 4.20: The events distribution for pp elastic scattering at $T_p = 2.57$ GeV. The points are experimental data and the cure is the prediction from the SAID solution multiplied by luminosity.

The last step for calculating the luminosity is to determine the total number

of elastic events. The large *pp* elastic cross section in combination with the high momentum resolution of the forward detector, allows one to separate the elastically scattered protons from the background using the missing mass technique. Typical spectra of missing mass in several angular ranges are shown in Fig. 4.19. The clear peak of *pp* elastic events sitting on the background was then fitted with a Gaussian distribution, while the background was subtracted using a second order polynomial fit. The elastic events have been corrected by the pre-scaling factor, trigger efficiency and the detection efficiency using the 2D efficiency map, as shown in Fig. 4.16. After a 3σ cut on the missing mass spectra, the total number of final *pp* elastic events is determined:

$$N_{tot} = \frac{N_{det} \cdot f}{\varepsilon_{trigger} \cdot \varepsilon_{det}} \tag{4.6}$$

where N_{det} is the total number of detected *pp* elastic events, f is the pre-scaling factor and $\varepsilon_{trigger}$ is the trigger efficiency of T_2, while ε_{det} is the track efficiency.

Finally, the luminosity can be calculated as:

$$\frac{d\sigma}{d\Omega}(\theta) = \frac{1}{L}\frac{N_{tot}}{\Omega_{det}}(\theta). \tag{4.7}$$

As shown in Fig. 4.20, one can fit the experimental angular distribution to obtain the luminosity L. The individual contributions to the systematic uncertainty of the luminosity determination at different beam energies are listed in Table. 4.1.

4.6.2 Luminosity determination by Schottky method

As an independent check of the *pp* elastic scattering method, one can measure the effective target thickness and the beam flux, and therefore the luminosity by:

$$L = n_B \cdot n_T \tag{4.8}$$

Table 4.1: Systematic uncertainties for luminosity determination via the *pp*-elastic scattering. The total error has been obtained by adding the individual elements quadratically.

Uncertainty	2.57 GeV	2.83 GeV
Track reconstruction efficiency	5%	5%
Acceptance correction	6%	7%
Momentum reconstruction	1%	1%
Background subtraction	3%	3%
ΔL=(L$_\theta$-L$_{Mean}$)	2%	2.4%
Total	8.6%	9.5%

where n_B is the beam flux and n_T the effective target thickness. For experiments with an internal target at a storage ring, the target thickness cannot be simply established through macroscopic measurements. However, when a charged beam passes through a thin target many times, its energy loss is proportional to the target thickness. Moreover, the energy loss builds up steadily in time and causes a shift in the frequency of revolution in the machine which can be measured through the study of the Schottky spectra. Thus, the target thickness can be obtained by measuring the frequency shift of the proton beam [158]:

$$n_T = \frac{1+\gamma}{\gamma}\frac{1}{\eta}\frac{1}{(dE/dX)m}\frac{T_0}{f_0^2}\frac{df}{dt} \tag{4.9}$$

where γ is the Lorentz factor, η is the frequency-slip parameter, dE/dX is the stopping power [5], and m is the mass of the target atom. T_0 and f_0 represents the initial beam energy and the revolution frequency of the accelerator, respectively. The frequency shift $\frac{df}{dt}$ during one cycle is measured using the Schottky spectrum as:

$$(\frac{df}{dt})_{target} = (\frac{df}{dt})_{total} - (\frac{df}{dt})_{bg} \tag{4.10}$$

where $(\frac{df}{dt})_{total}$ is the observed frequency shift during the normal measurement and $(\frac{df}{dt})_{bg}$ is the frequency shift produced by the residual gas of the COSY ring. The mean

revolution frequency shifts are shown for a sample of machine cycles in Fig. 4.21. In each cycle, the frequency shift is well described by a linear function, which is consistent with the assumption that the overlap between beam and target changes little over the cycle.

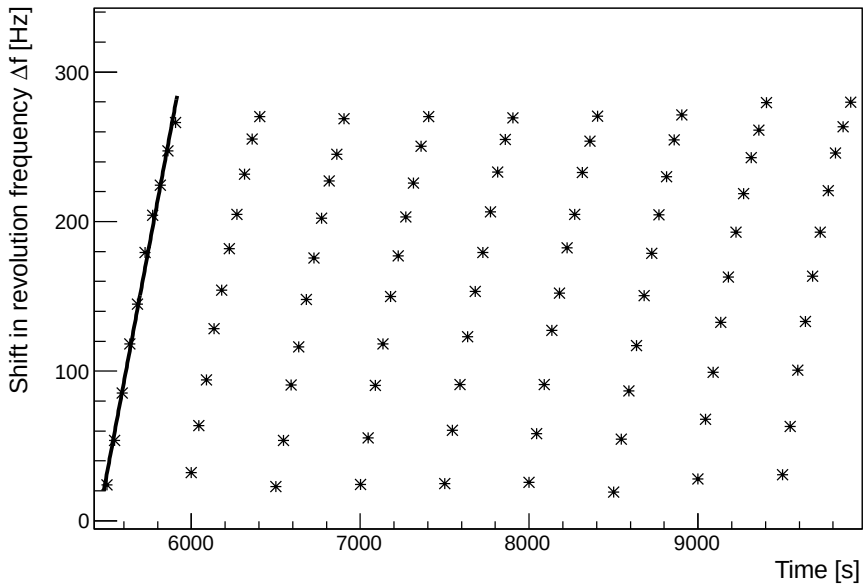

FIGURE 4.21: Typical mean revolution frequency shift derived from the Schottky spectra for a sample of machine cycles.

The η parameter can be calculated using $\eta = \frac{1}{\gamma^2} - \alpha$, where α is the momentum compaction factor. The α value a constant value for a given lattice setting can be measured by:

$$\frac{\Delta f}{f} = \alpha \frac{\Delta B}{B} \tag{4.11}$$

where Δf represents the variation of the mean revolution frequency, ΔB is the change of magnetic field B by a few parts per thousand. The fitting is shown in Fig. 4.22.

The beam current $I_B = n_B e$ was measured by a high precision beam current transformer (BCT), which was continuously recorded by the ANKE DAQ system.

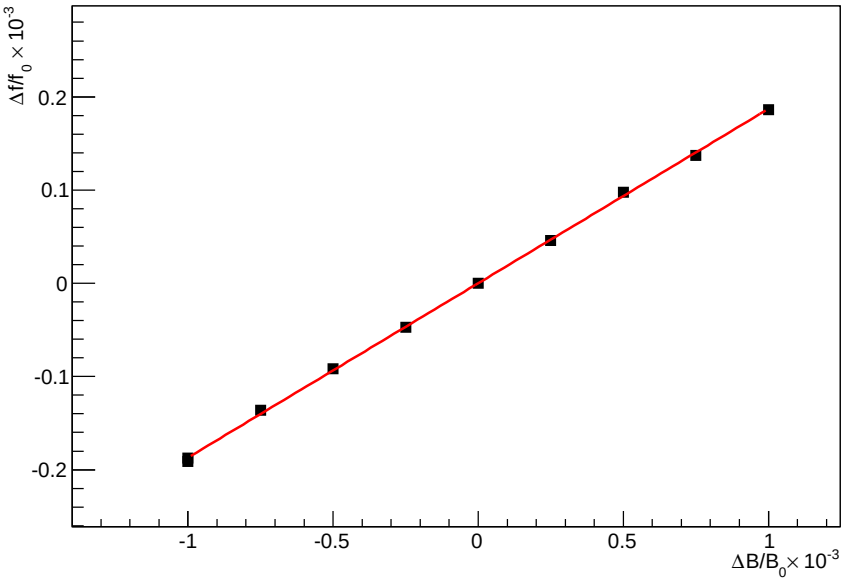

FIGURE 4.22: Variation of the mean revolution frequency with the field strength in the bending magnets in parts per thousand. The slope of the straight line yields the value of the momentum compaction factor α.

It was calibrated to deliver a voltage signal of 100 mV for a 1 mA current. The initial beam current varies from cycle to cycle, and decreases in each cycle with respect to time due to energy losses. Thus, in the analysis the mean value $\langle n_B \rangle$ has been determined for each cycle, which yields the integrated luminosity over a certain period of time. Finally, the luminosity can be determined with the obtained value of the target thickness and beam current.

The systematic uncertainty in the determination of the effective target thickness mostly comes from the measurement of the frequency shift rate (4%) and the frequency-slip parameter η (3%). The measurement of the beam current with the BCT is accurate to 0.1%, therefore its error is neglected in the analysis.

The Schottky method yields a luminosity with an overall uncertainty of 5%, which is compared directly with the values derived from *pp* elastic scattering, as shown in Fig. 4.23. The two method give consistent results within the uncertainties. The *pp*

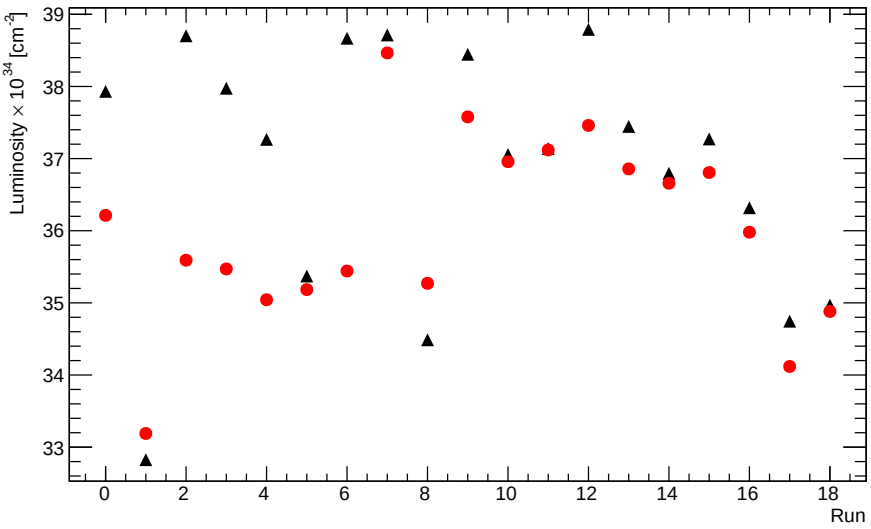

FIGURE 4.23: Comparison of the luminosity determined by the Schottky method (red points) and by elastic scattering (black points)

elastic scattering method was used in the analysis in order to be consistent with previous measurements. In addition, according to [63], the Schottky method could not be applied as reliably in the higher energies.

Careful monitoring of the Schottky spectra not only allows the absolute luminosity determination with a precision of the order of $\sim 6\%$, but also permits one to measure momentum changes of the beam during the cycle. A big challenge in the close-to-threshold measurements is the determination of the beam momentum with sufficient accuracy, since the total cross section can change significantly with a small change of the excess energy. One can determine the beam momentum in the experiment by using the knowledge of the beam trajectory and monitoring the beam frequency using the Schottky method [159].

5

Detector Acceptance

After identifications of the specified reaction channels and determination of the experimental luminosity, the raw experimental distributions can be calculated, which must be corrected for the detector acceptance in order to extract the differential cross sections. The acceptance of the ANKE spectrometer is determined through a Monte Carlo simulation based on GEANT4, in which the geometrical acceptance, resolution, detector efficiency, and kaon decay probability were taken into account. Since we were interested in four-body final state, a phase-space calculation may work well as a starting point. However, most of the time the detector acceptance is not uniform over the phasespace, there is even zero acceptance for some parts of the phasespace. Moreover, the real distributions may deviate significantly from the pure phasespace. Thus, we need phenomenological parametrizations that describe well the experimental data as much as possible in order to perform necessary acceptance corrections. In the analysis, a number of parametrizations have been applied to different reactions to study the ANKE acceptance.

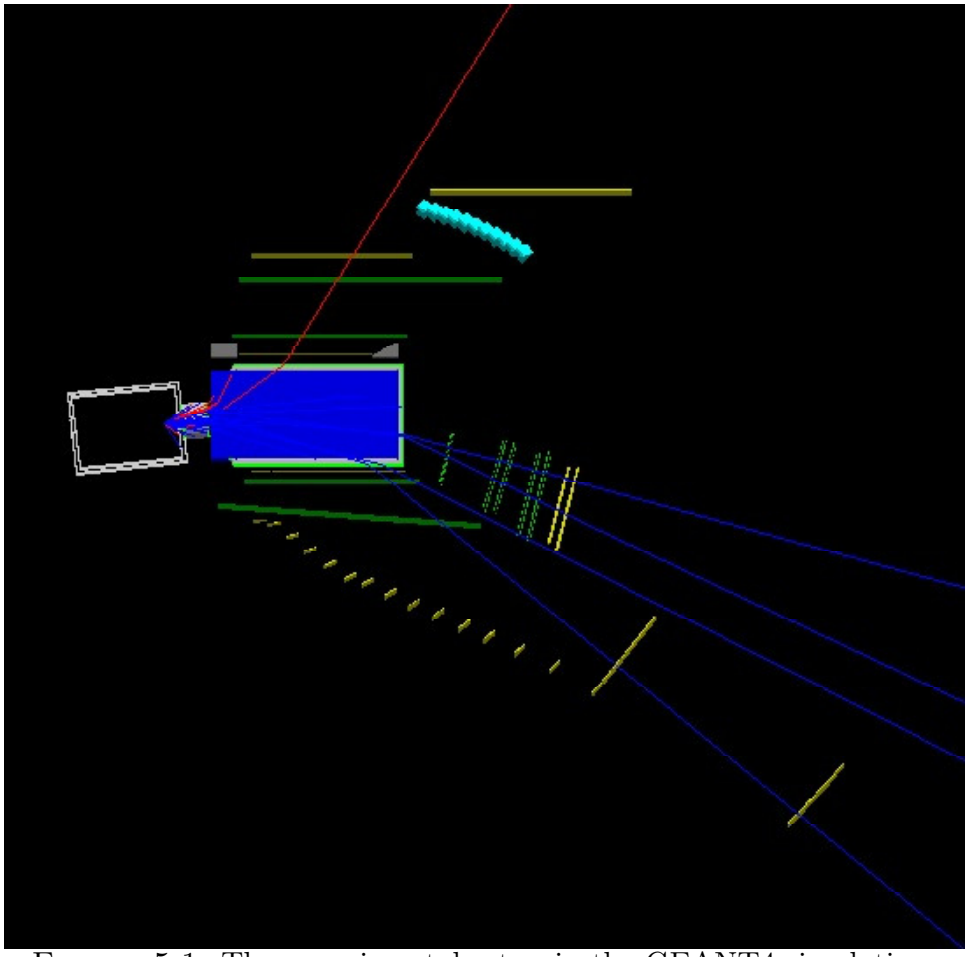

FIGURE 5.1: The experimental setup in the GEANT4 simulation.

5.1 Geant4 Simulation

A GEANT4 based Monte Carlo simulation has been developed to study the ANKE acceptance, which uses the database interface to construct the experimental geometry [160]. It defines the shape and materials of all the detector setups as well as passive elements like the vacuum chamber and the beam pipe. Different ANKE detectors can be added into the simulation by calling the corresponding classes. The following detectors are included in the simulation: the three particle detection systems (Pd, Nd and Fd), the D2 vacuum chamber and the target chamber. A picture of the implemented geometries is shown in Fig. 5.1.

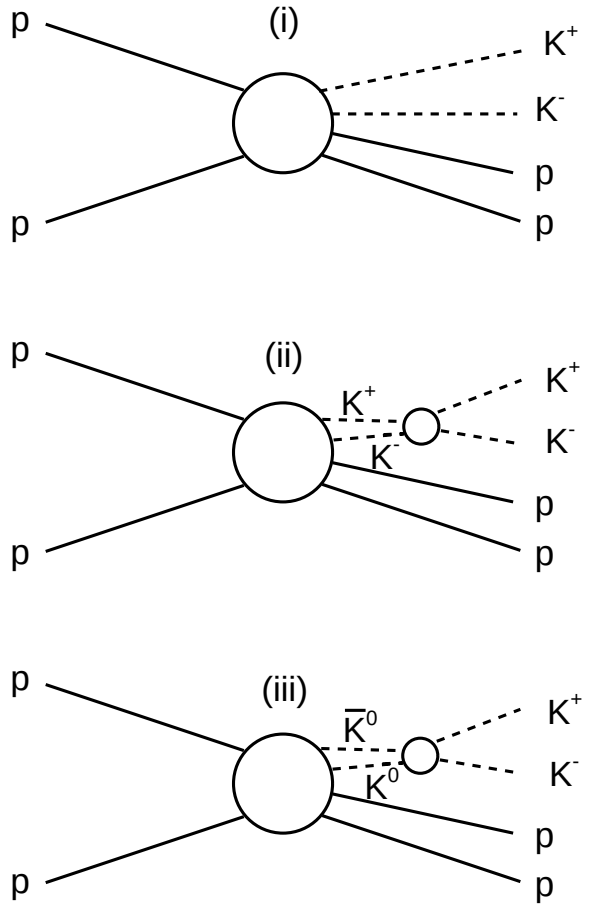

FIGURE 5.2: Diagrammatic representation of (i) direct production of K^+K^- pairs, where the large blob includes the *fsi* effects in the pp and K^-p systems considered in Ref. [63]. The elastic K^+K^- *fsi* is illustrated in (ii) and the production of virtual $K^0\bar{K}^0$ pairs followed by a charge exchange *fsi* in (iii)

Particles generated from an event generator Pluto [162] are read into the simulation. In the program, the reaction vertex can be specified as a point like or extended vertex with various shapes. The magnetic field map that implemented in the simulation was based on Mafia calculations. The simulation outputs contain hits information in the scintillators as well as trajectories of tracks in the wire chambers. Each hit carries the information about the particle that produced the hit (type and momentum), its position and the time since the start of the event. The simulation results were analyzed in the same procedures as we did for the experimental data,

as described in Chapter. 4.

5.2 Acceptance correction for the $pp \to ppK^+K^-$ reaction

We start the analysis with the non-ϕ kaon pair production since it is crucial to master this contribution to understand the background under the ϕ peak. The model-independent acceptance estimation method used in our earlier work [48] cannot be applied in the present analysis since the number of zero elements in the acceptance matrix is significant and this leads to large fluctuations and uncertainties. Phenomenological parametrizations must therefore be relied upon in order to perform the necessary acceptance corrections.

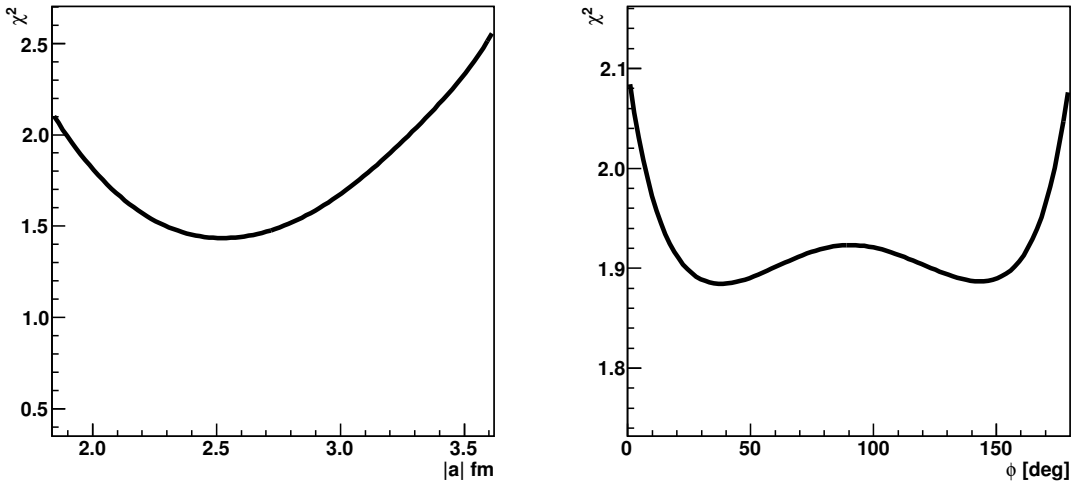

FIGURE 5.3: The reduced χ^2 distributions with respect $|a|$ and ϕ at $\varepsilon_{KK} = 23.9$ MeV. Our best fit was obtained with $a_{K^-p} = 2.45i$ fm.

A simple ansatz that takes into account the influence of the pair-wise final state interactions was taken as the basis of the simulation. As discussed before, we assumed that the overall enhancement factor F is the product of enhancements in the pp, K^+K^-, and K^-p systems [63, 96]:

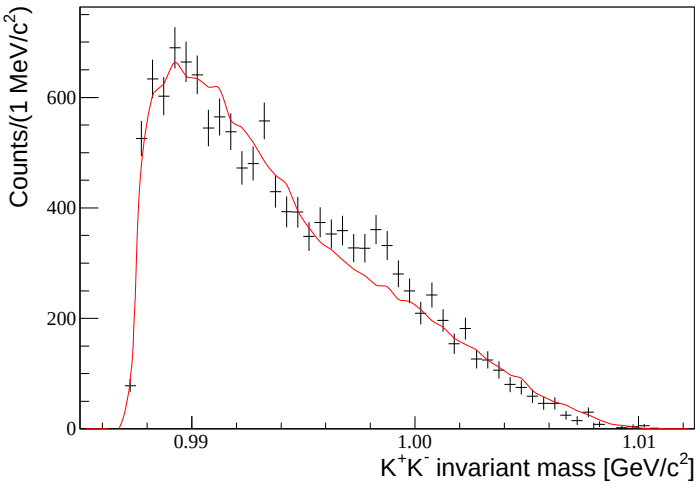

FIGURE 5.4: (Color online) The raw K^+K^- invariant mass distribution at ε = 23.9 MeV, $\mathrm{IM}_{K^+K^-}$ (points), is compared with the distribution of events obtained in a Monte Carlo simulation (curve). The error bars indicate only the statistical uncertainties.

$$F = F_{pp}(q_{pp}) \times F_{Kp}(q_{Kp_1}) \times F_{Kp}(q_{Kp_2}) \times F_{KK}(q_{KK}) \tag{5.1}$$

where q_{pp}, q_{Kp_1}, q_{Kp_2} and q_{KK} are the magnitudes of the relative momenta in the corresponding systems. The details of these enhancement factors are discussed as follows:

- K^-p **FSI**. To describe the interaction between K^- and p in the final state, the scattering length approximation with $F_{Kp}(q) \approx 1/|1 - iqa_{K^-p}|^2$ was used. The scattering length a_{K^-p} is unknown and thus applied as a fitting parameter in the analysis. It is believed that the K^+p interaction might be weakly repulsive and, if so, its neglect would be interpreted as an extra attraction in the K^-p system.

- pp **FSI**. The proton-proton enhancement factor was taken into account by

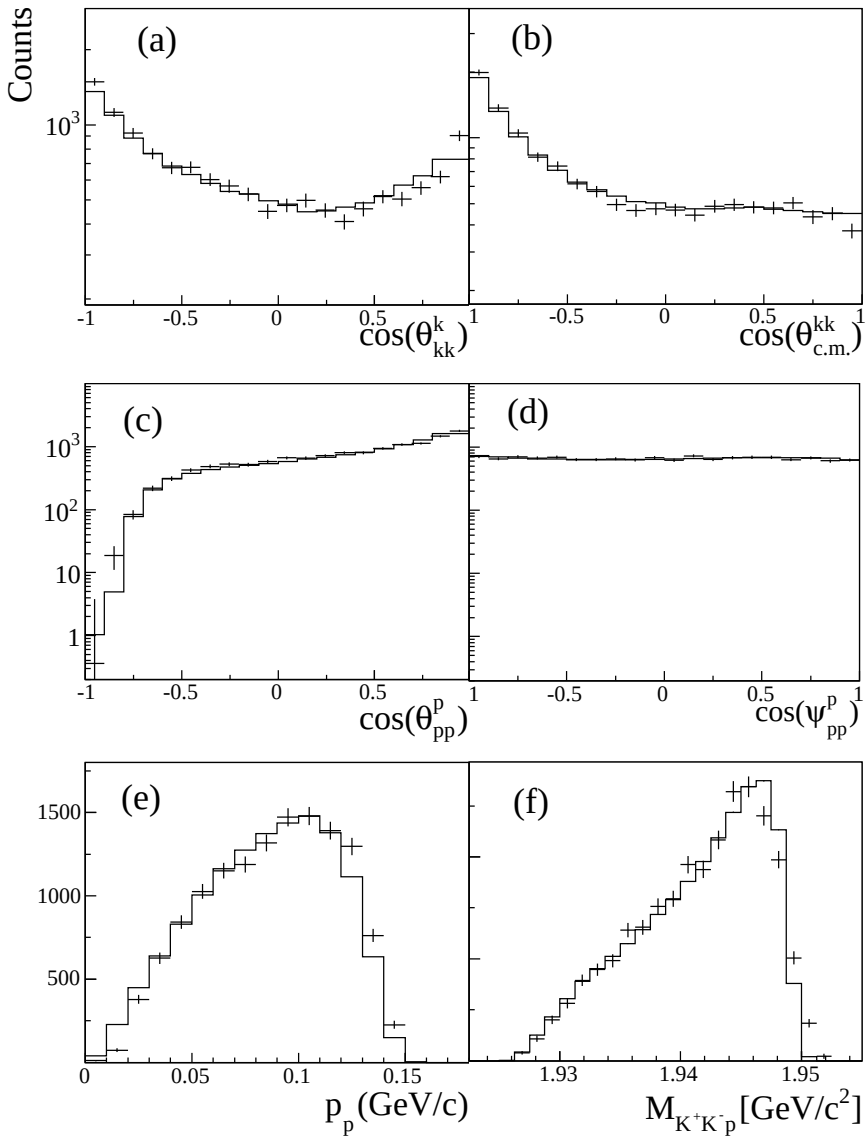

FIGURE 5.5: Differential distributions of experimental (points) and simulated (histograms) yields for kaon pair production in the $pp \rightarrow ppK^+K^-$ reaction at $T_p = 2.57$ GeV. Vertical bars represent the statistical uncertainties and horizontal ones the bin widths. The individual panels are (a) the cosine of the polar angle of the K^+ in the K^+K^- reference frame, (b) the polar angle of the kaon pairs in the overall c.m. frame, (c) the polar angle of the emitted proton in the *pp* reference frame relative to the beam direction, (d) the polar angle of the proton in the *pp* reference frame relative to the direction of the kaon pair, (e) the proton momentum in the *pp* reference frame, and (f) the K^+K^-p invariant mass distribution.

means of the Jost function method with:

$$|J(q)|^{-1} = \frac{q+i\beta}{q-i\alpha} = [\frac{r\beta^2}{2} + \frac{rq^2}{2}][-\frac{1}{a} + \frac{rq^2}{2} - iq]^{-1}, \tag{5.2}$$

where Goldberger and Watson parametrization [100] is used. α and β are the parameters that specify the FSI between the two protons, they are related to the scattering length by:

$$a = \frac{\alpha+\beta}{\alpha\beta}, r = \frac{2}{\alpha+\beta} \tag{5.3}$$

The position of the $^1S_0$ virtual state is well fixed at α =0.1 fm^{-1}. The pp final state interaction should not influence higher partial waves and, in order to reduce the effects above $\sim$ 10 MeV, β = 0.5 fm^{-1} was taken in the formula:

$$|F_{pp}(q)|^2 = \frac{q^2+\beta^2}{q^2+\alpha^2} \tag{5.4}$$

- K^+K^- **FSI**. The enhancement factor in the K^+K^- system takes into account an elastic K^+K^- scattering plus a charge-exchange process $K^+K^- \rightleftharpoons K^0\bar{K}^0$ [96]. Fig. 5.2 illustrates the three types of contributions that are considered in the analysis. Assuming that B_0 and B_1 are the amplitudes for producing s-wave $K\bar{K}$ pairs in isospin-0 and 1 states, respectively. These amplitudes are then distorted through a FSI corresponding to elastic scattering. This leads to an enhancement factor of $1/(1-ikA_I)$, where k is the relative momentum in the K^+K^- system and A_I is the s-wave scattering length in the isospin channels. The scattering length of the charge-exchange $K^0\bar{K}^0 \rightleftharpoons K^+K^-$ process is proportional to the difference between A_0 and A_1 and the relative momentum. In summary, the enhancement factor has the form:

$$F_{KK} = |\frac{B_1/(B_1+B_0)}{(1-iq[A_1-A_0]/2)(1-ikA_1)} + \frac{B_0/(B_1+B_0)}{(1-iq[A_0-A_1]/2)(1-ikA_0)}|^2 \tag{5.5}$$

There are large uncertainties in the numerical values of $K\bar{K}$ scattering lengths. Here we take $A_1 = (0.1 \pm 0.1) + i(0.7 \pm 0.1)$ fm [163, 164, 165, 166]. Values of the isoscalar scattering length can be extracted from fits to data [166, 167, 168, 169], but what deduced from the BES Collaboration data [170], $A_0 = (-0.45 \pm 0.2) + i(1.63 \pm 0.2)$ fm seems to be the most reliable. The ratio of the $I = 1$ and $I = 0$ production amplitudes of s-wave $K\bar{K}$ pairs was parametrized as

$$B_1/B_0 = Ce^{i\phi_c}, \tag{5.6}$$

where C is the unknown magnitude and ϕ_c the phase angle.

For an unpolarized measurement of the ppK^+K^- final state, sixteen degrees of freedom (d.o.f) are required to parametrize the reaction. However, there exist several constraints that reduce the number of d.o.f. Particle identification and four-momentum conservation law reduce the number of d.o.f to eight. Considering that the final states should be symmetrical with respect to the beam direction, seven d.o.f are sufficient, which were chosen to be the K^+K^- and K^+K^-p invariant masses, the relative momentum of the protons in the pp system, and four angular distributions as follows:

- $cos\theta^{K^+}_{K^+K^-}$. The polar angle of K^+ in the K^+K^- reference frame.
- $cos\theta^{K^+K^-}_{c.m.}$. The polar angle of the kaon pair with respect to the beam direction in the overall center-of-mass (c.m.).
- $cos\theta^{p}_{pp}$. The polar angle of the emitted proton with respect to the beam direction in the pp reference frame.
- $cos\Psi^{p}_{pp}$. The polar angle of the emitted proton with respect to the direction of the kaon pair system in the pp reference frame.

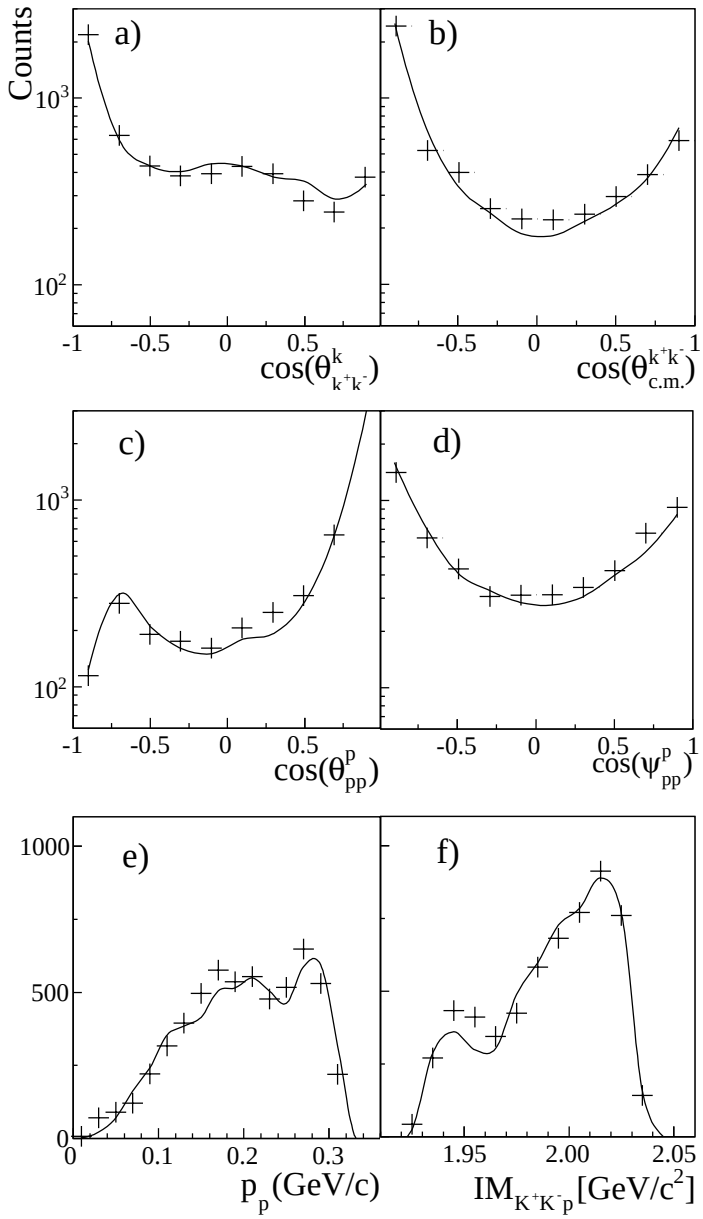

FIGURE 5.6: Differential distributions of experimental and simulated yields for kaon pair production in the $pp \to ppK^+K^-$ reaction at $T_p = 2.83$ GeV. The notations for the six panels are the same as those in Fig. 5.5.

Monte Carlo events of the $pp \to ppK^+K^-$ phase space weights were reconstructed in the same way as the experimental data, which takes into account the detector resolution. The events were then re-weighted according to Eq. 5.1. It should be

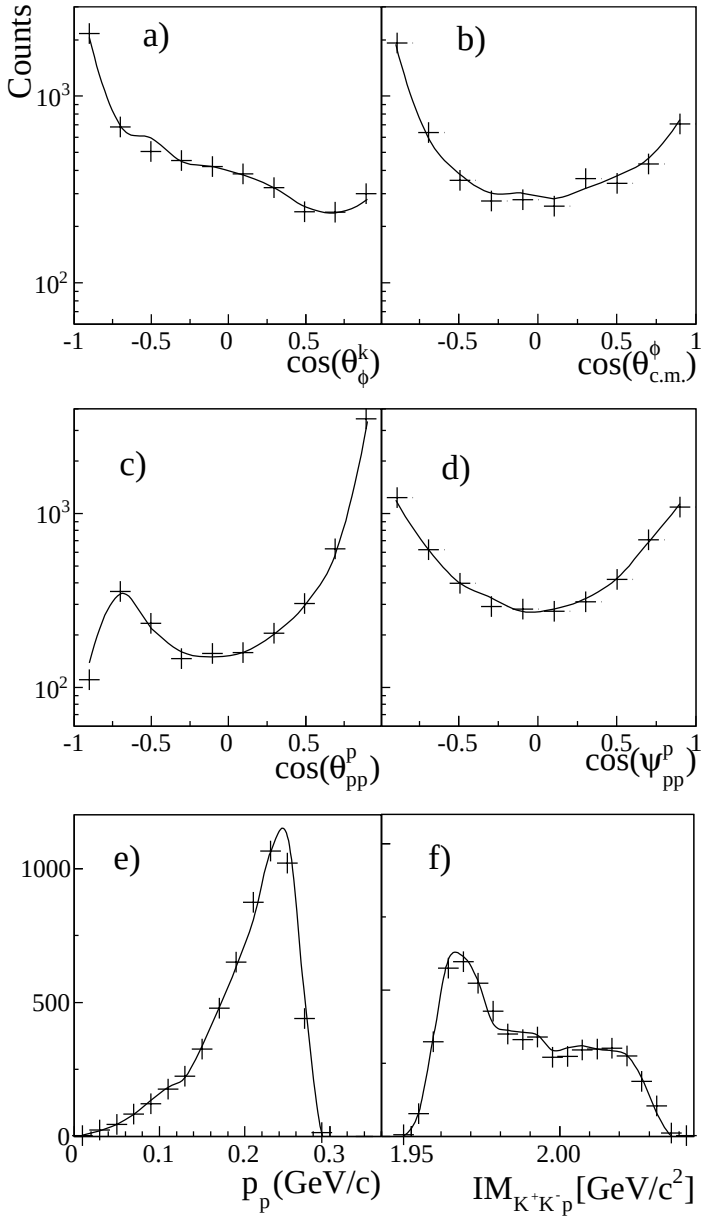

FIGURE 5.7: The differential distributions of yields in the ϕ region (1.01 GeV/c^2 < $\mathrm{IM}_{K^+K^-}$ < 1.03 GeV/c^2) for the $pp \to ppK^+K^-$ reaction at $T_p = 2.83$ GeV, where the points are experimental data and the curves represent simulations. The notations for the six panels are the same as those in Fig. 5.5.

noted here that it was not possible to describe the data at the two excess energies by the same set of parameters. The purpose of the model is to describe data as

closely as possible in order to perform acceptance correction at the two energies. No attempt was made to fit both data simultaneously. Here we assume a constant production amplitude, therefore the different energies should be taken into account by the q^2 factors. Using the coefficients from [63, 96] as starting parameters, a couple of simulations were carried out for different sets of the coefficients leading to differential distributions that were convoluted with the acceptance. For each choice of the parameters, the χ^2 values have been calculated as the difference between simulated and measured distributions. Subsequently, the coefficients that describe the experimental data best have been determined by minimizing χ^2 (calculated as Eq. 5.7)with the MINUIT package, which is an efficient and widely used routine. In practice, the simulated and measured results are presented as one-dimensional histograms, which were then used to correct the experimental distributions bin-by-bin. In order to check the fitting results, a grid fitting method was adopted that loops each possible combination of the parameters for calculating global minimum χ^2.

$$\chi^2 = \sum \frac{(O_i(X_i) - \hat{O}_i(\vec{x}, X_i))^2}{\sigma_i^2} \tag{5.7}$$

The uncertainties caused by the fitting procedure are not considered as a source of systematic uncertainties. Instead, the difference between the model and phase space are taken into account. Finally, a MC simulation based on the best fit parameters was implemented to check the match between simulation and data.

5.2.1 $T_p = 2.57$ GeV

The best fit to the data at $\varepsilon_{KK} = 23.9$ MeV ($T_p = 2.57$ GeV) was achieved with $a_{K^-p} = (2.45 \pm 0.4)i$ fm. Nevertheless, the uncertainties in the real and imaginary parts are quite large and strongly correlated with the imaginary part. It should be noted that the absolute value of the scattering length is determined much better

than its phase, as illustrated by the projections of the χ^2 contour plot in Fig. 5.3. To allow easy comparison with the analysis of the higher energy data, the effective scattering length was taken to be purely imaginary.

Table 5.1: The fit results for the magnitude and phase of the ratio of the $I = 1$ and $I = 0$ amplitudes of Eq. (5.6). The data are fitted using the *ansatz* of Eq. (5.6) with (i) both elastic and charge-exchange *fsi*, (ii) elastic *fsi* alone, and (iii) purely charge-exchange *fsi*.

Fit parameter.	el.+c.e.	el. alone	c.e. alone
C	0.54 ± 0.03	0.74 ± 0.1	0.57 ± 0.01
ϕ_C (deg)	-112 ± 4	181 ± 1	-145 ± 2

The fit results for K^+K^- FSI was shown in Table. 5.1. As it is seen that the resulting descriptions of the experimental data in Fig. 5.4 and Fig. 5.5 are very good and certainly sufficient for evaluating the ANKE acceptance.

5.2.2 $T_p = 2.83\ GeV$

The best fit of the K^-p scattering length at $T_p = 2.65 - 2.83$ GeV is $a_{K^-p} = 1.5i$ fm with large uncertainty in both real and imaginary parts, as shown by the countour plot (Fig. 5.8). The free K^-p $I = 0$ and $I = 1$ values from Ref. [63] are also shown there along with their one-σ limits. There is an overlap with either isospin scattering length.

The fit results for K^+K^- FSI were shown in Table. 5.2. The resulting descriptions of the experimental data as shown in Fig. 5.6 are very good and certainly sufficient for evaluating the acceptance.

5.3 Acceptance correction for the $pp \to pp\phi$ reaction

Turning now to the ϕ meson production in proton-proton collisions, the only amplitude that survives at threshold corresponds to the ${}^3P_1 \to {}^1S_0 s$ transition. We here

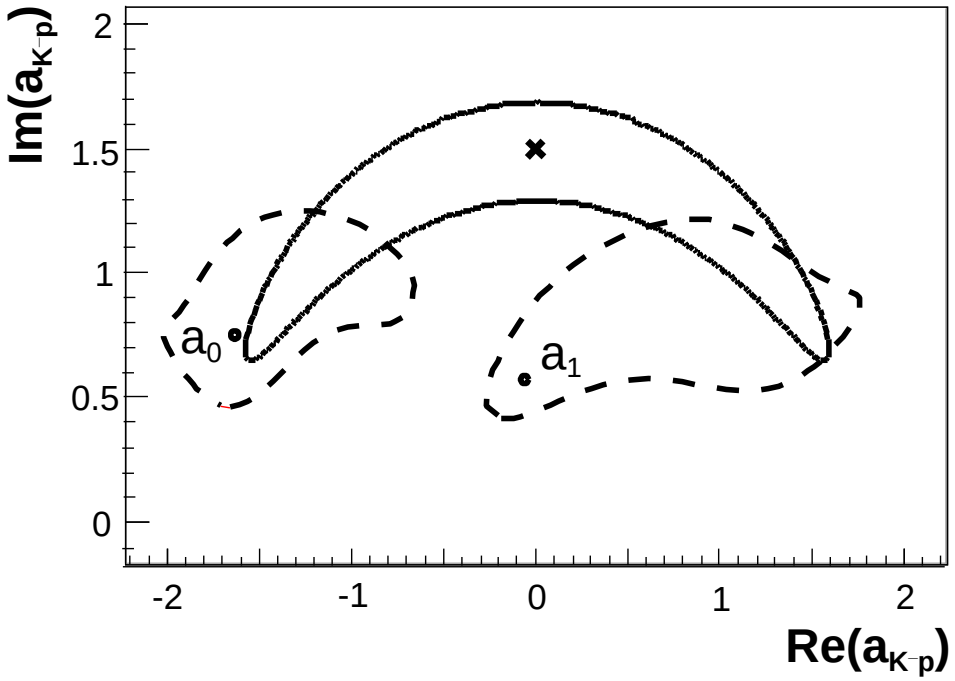

FIGURE 5.8: Contour plot corresponding to the one–σ level uncertainty of the fits of the complex parameter a of the *fsi ansatz*. Our best fit is obtained with $a = 1.5i$ fm (marked with a cross). Also shown are the best fit values (points) and corresponding contours (dashed lines) for the isoscalar (a_0) and isovector (a_1) K^-p scattering lengths derived from the study of free K^- nucleon scattering [179]

Table 5.2: The notations are the same as 5.1.

Fit parameter.	el.+c.e.	el. alone	c.e. alone
C	0.66 ± 0.1	0.9 ± 0.01	0.50 ± 0.04
ϕ_C (deg)	-87 ± 10	151 ± 2	-132 ± 6

denote the final state using $^{2S+1}L_J\ell$, where S, L, and J represent the total spin, orbital angular momentum and total angular momentum of the pp system, respectively, and ℓ the orbital angular momentum of the ϕ relative to the pp system. Our previous analysis indicates that the differential cross section at an excess energy $\varepsilon_\phi = 18.5$ MeV with respect to the ϕ threshold is dominant by the S-wave, with a clear effect coming from the pp final state interaction [48].

In contrast, significant contributions from higher partial waves were suggested by the DISTO data at $\varepsilon_\phi = 83$ MeV [47]. The measured differential cross sections as functions of the relative momentum in the pp reference frame and the momentum of ϕ meson in the c.m. system were interpreted as reflecting the importance of Ps and Sp final waves, respectively. The anisotropy in the helicity distribution shows the necessity for a Pp wave contribution. As it is shown in sec. 2.2.3, there are many possible transitions that could lead to a $pp\phi$ final state. Here we keep only typical ones in our model description, in which the spin-averaged squared transition matrix element can be written as:

$$\begin{aligned} \overline{|M|^2} &= A_{Ss}\,(\hat{k}\times\hat{K})^2 + A_{Ps}\,\vec{p}^{\,2} + A_{Pp}(\vec{q}\cdot\vec{p})^2 \\ &\quad + A_{Sp}\left[3(\vec{q}\cdot\hat{K})^2 - \vec{q}^{\,2}\right]. \end{aligned} \tag{5.8}$$

where the momenta of the proton beam and ϕ meson in the overall c.m. system are denoted by $\vec{K}$ and $\vec{q}$, respectively. $\hat{k}$ represents the momentum of decay kaons in the ϕ reference frame, and $\vec{p}$ is the relative momentum in the final pp system.

Apart from the explicit momentum factors, we assume that the coefficients $A_{L\ell}$ in Eq. (5.8) are constant except that, at low invariant masses, the final pp system in the $^1S_0$ state is subject to a very strong final state interaction. The A_{Ss} and A_{Sp} contributions in Eq. (5.8) were therefore multiplied by an enhancement factor which was calculated using the Jost function in Eg. (5.4). The Coulomb interaction was neglected and, crucially, no attempt was made to include a final state interaction in the ϕp system.

The ϕ meson was taken to have a Breit-Wigner form with a width of $\Gamma = 4.26$ MeV/c^2 [171], convoluted with a resolution width of $\sigma \simeq 1$ MeV/c^2. The values of the coefficients $A_{L\ell}$ in Eq. (5.8) were determined by the following procedure: the simulations were carried out for different sets of the coefficients leading to differential distributions convoluted with the acceptance. For each choice of the

coefficients $A_{L\ell}$, the χ^2 values have been calculated for the difference between simulated and measured distributions. Subsequently, the coefficients which describe the experimental data best have been determined by minimizing χ^2 with the MINUIT package [172]. The best fit results are shown in Table 5.3. The resulting descriptions of the experimental data in Fig. 5.7 are very good and certainly adequate for carrying out the acceptance corrections. The invariant mass distribution of K^+K^- is shown in Fig. 5.9. A clear ϕ peak is observed above a slowly varying background. A cut was applied to divide the experimental data into two samples, a ϕ-rich region where 1.01 GeV/$c^2 < IM_{K^+K^-} <$ 1.03 GeV/c^2 and a non-ϕ (the rest) region.

Table 5.3: Values of the model parameters of Eq. (5.8) deduced by comparing the simulations with data in the ϕ region. The momenta are measured in GeV/c. All the parameters are normalized to $A_{Ss} = 1$ and the corresponding uncertainty of ± 0.25 is not included.

Parameter	Fit value
A_{Ss}	1.0
A_{Sp}	9.9 ± 1.8
A_{Ps}	143 ± 4
A_{Pp}	293 ± 21

The systematic uncertainties arise from the acceptance correction were estimated by comparing the final results that have been corrected according to the model to those corrected by phase space. This difference probably represents the worst case scenario, in the sense that no model differed more from our parametrization than phase space would be considered.

5.4 Acceptance correction for the $pp \to pK^+\Lambda$ reaction

The acceptance correction for the $pp \to pK^+\Lambda$ reaction is based on the program that is designed to fit $NN \to BBP$ data where B is a $J^P = \frac{1}{2}^+$ baryon and P is a

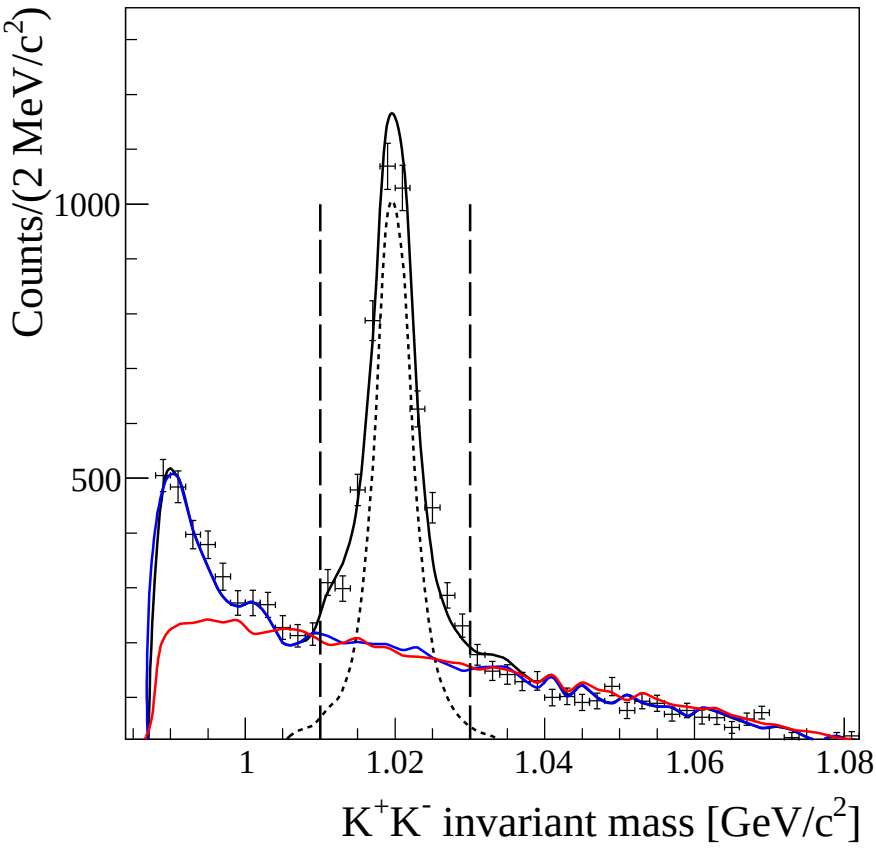

FIGURE 5.9: (Color online) The raw K^+K^- invariant mass distribution, $M_{K^+K^-}$ (points), is compared with the distribution of events obtained in a Monte Carlo simulation (curve). The error bars indicate only the statistical uncertainties. The blue curve shows the non-ϕ contributions within the fitted parametrization, the red curve the four-body phase-space simulation of ppK^+K^-, and the dotted histogram the ϕ contributions. The solid line is the incoherent sum of the ϕ and non-ϕ contributions. The vertical lines indicate the cuts used for the separation of the ϕ-rich and non-ϕ regions. The fluctuations reflect the Monte Carlo sampling effects.

pseudoscalar meson. The cross section for the $pp \to pK^+\Lambda$ reaction is given by [173]:

$$d\sigma = \frac{(2\pi)^4 |A|^2}{4|\vec{k}|\sqrt{s}}\, d\Phi_3(P, q_1, q_2, q_3)\ , \qquad P = k_1 + k_2\ , \tag{5.9}$$

where A is the reaction amplitude, $\vec{k}$ is the 3-momentum of the initial particle calculated in the c.m.s system of the reaction, and $s = P^2 = (k_1 + k_2)^2$. The two colliding

particles have 4-momenta k_1 and k_2, while final particles have 4-momenta q_i. The invariant phase space is given by:

$$d\Phi_m(P, q_1 \dots q_m) = \delta^4(P - \sum_{i=1}^{3} q_i) \prod_{i=1}^{3} \frac{d^3 q_i}{(2\pi)^3 2 q_{0i}} \ . \tag{5.10}$$

and the total reaction amplitude A can be written as a sum of the partial wave amplitudes:

$$A = \sum_{\alpha} A^{\alpha}_{tr}(s) Q^{in}_{\mu_1 \dots \mu_J}(SLJ) A_{2b}(i, S_2 L_2 J_2)(s_i) \times Q^{fin}_{\mu_1 \dots \mu_J}(i, S_2 L_2 J_2 S' L' J) \ .$$

where the operators for initial states $Q^{in}_{\mu_1 \dots \mu_J}(SLJ)$ and final states $Q^{fin}_{\mu_1 \dots \mu_J}(i, S_2 L_2 J_2 S' L' J)$ can be found in [174]. S, L, J represent spin, orbital momentum and total angular momentum of the pp system, S_2, L_2, J_2 are spin, orbital momentum and total angular momentum of a two-particle system in the final state, and S', L' are spin and orbital momentum between the two particle system and a third particle. The best description of the transition amplitude $A^{\alpha}_{tr}(s)$ was obtained with the parametrization:

$$A^{\alpha}_{tr}(s) = \frac{a^{\alpha}_1 + a^{\alpha}_3 \sqrt{s}}{s - a^{\alpha}_4} \, e^{i a^{\alpha}_2}, \tag{5.11}$$

where a^{α}_i are real parameters.

For the description of the final pp interaction we use a modified scattering length approximation formula:

$$A^{\beta}_{2b}(s_i) = \frac{\sqrt{s_i}}{1 - \frac{1}{2} r^{\beta} q^2 a^{\beta}_{pp} + i q a^{\beta}_{pp} q^{2L} / F(q, r^{\beta}, L)}, \tag{5.12}$$

where multi-index β denotes possible combinations of a kinematic channel i and quantum numbers S_2, L_2 and J_2, a^{β}_{pp} is a pp-scattering length and r^{β} is the effective

range of the pp system. The $F(q, r, L)$ is the Blatt-Weisskopf form factor and q is a relative momentum in the pp-system.

As a first step, we carried out simulations of the $pK^+\Lambda$ final state by pure phase space emission within the ANKE acceptance. All possible configurations describe in sec. 4.4.2 were combined in order to cover the full phase space. Then, these simulations were weighted by PWA calculations and compared to the experimental data within the acceptance. Fig. 5.10 shows preliminary results for the best fit of three invariant mass spectra of the $pK^+\Lambda$ final state within the ANKE acceptance. The histograms show the experimental distributions of the invariant mass of the particle pairs: (a) $M(\Lambda K^+)$, (b) $M(pK^+)$, and (c) $M(p\Lambda)$. The red line show the same distributions obtained from the PWA results of the $pK^+\Lambda$ final state.

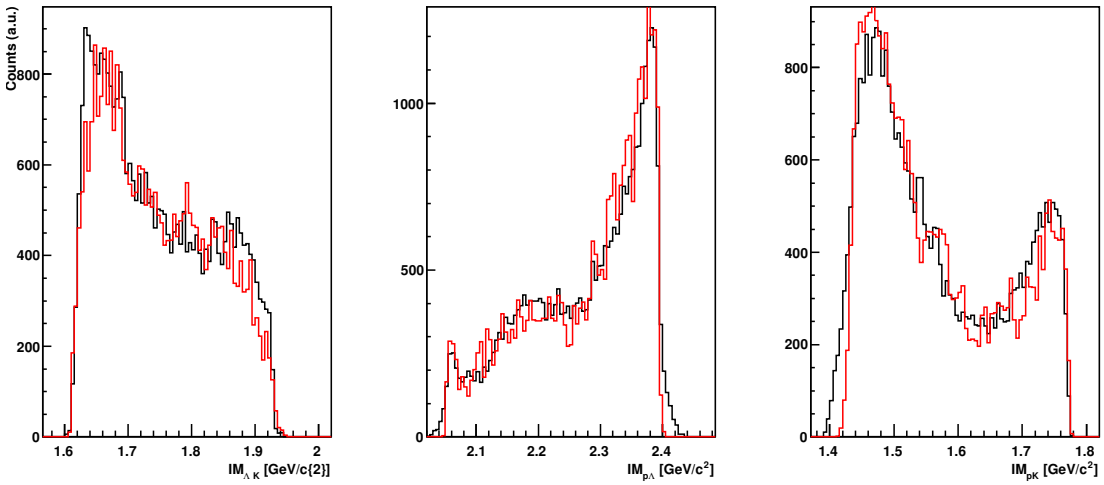

FIGURE 5.10: (Preliminary results) The black lines show the experimental distributions for the invariant mass of the particle pairs. ΛK, pK, and $p\Lambda$. The red lines show the same distribution obtained from PWA fitting.

Fig. 5.11 shows the angular distribution for the PWA fitting results and the experimental data within the ANKE acceptance for all combinations in the c.m., Gottfried-Jackson and helicity reference frames, which were defined analog to [175]. The Gottfried-Jackson (G-J) frame is defined as the rest frame of two final particles.

In this frame, the G-J angle is defined as the angle between one of the rest frame particles (e.g. the kaon in the $p-K$ system) and the proton beam. The G-J angle is denoted as (θ^{K-B}_{p-K}), where the superscript ($K-B$) represents for the angle of kaon with respect to the beam direction, the subscript ($p-K$) stands for the G-J rest frame. The motivation to study the G-J angles arise from the fact that in case of kaon exchange, the $p-K$ rest frame is equivalent to the rest frame of the exchanged meson and the proton. The helicity angle is defined in the same rest frame as the G-J angle, but instead of calculating the angle between one particle in the rest frame and the proton beam, the angle of the particle with respect to the third particle is used. In this sense, the helicity angle interrelates only the kinematics of the final three particles of the reaction. The helicity angular distribution is a special projection of the Dalitz plot, and thus a proper observable to identify the kinematics behind the particle production. A uniform populated Dalitz plot should result in isotropic helicity angular distributions, while the distorted Dalitz plot will reflect anisotropic distributions. Therefore, the helicity angle is an ideal tool to study not only final state interactions but also the possible contributions of intermediate resonances.

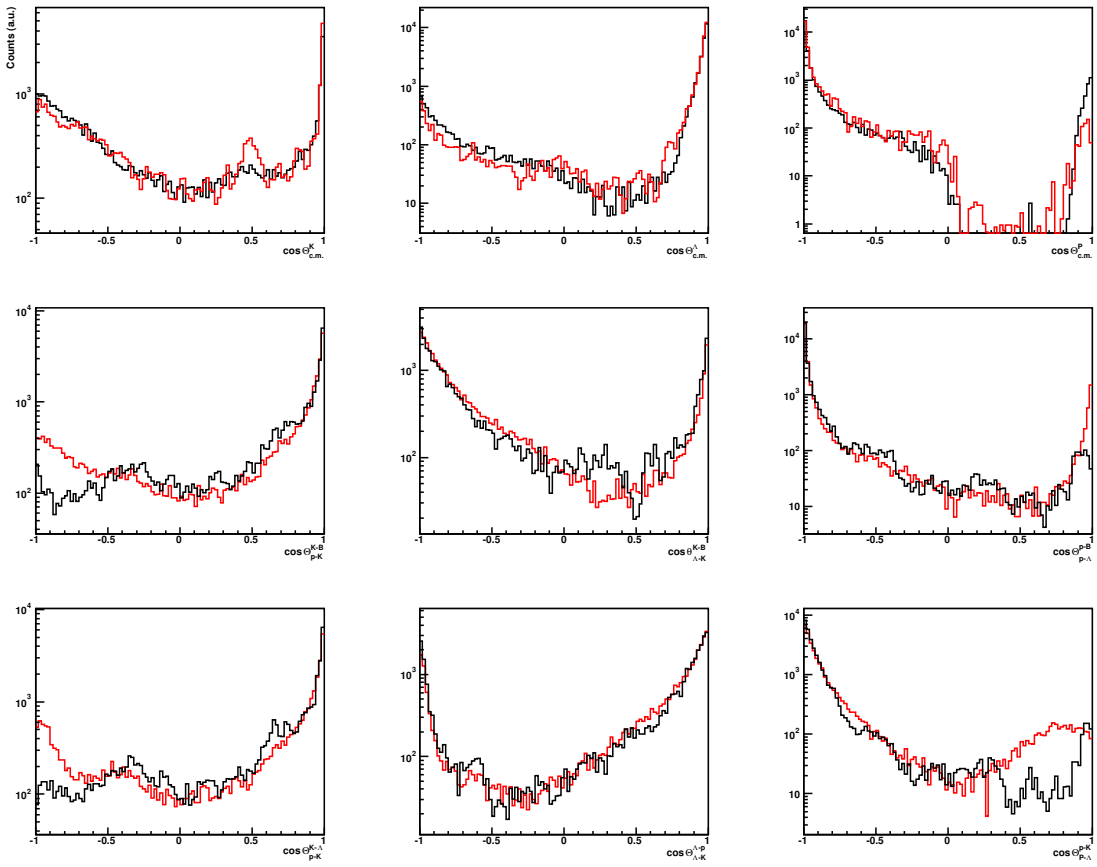

FIGURE 5.11: (Preliminary results) Angular distributionsfor the production in c.m. of Λ, p, and K^+ (top: (from left to right) $cos\Theta^{K}_{c.m.}$, $cos\Theta^{\Lambda}_{c.m.}$, and $cos\Theta^{p}_{c.m.}$), Gottfried-Jackson (middle: (from left to right) $cos\Theta^{K-B}_{p-K}$, $cos\Theta^{K-B}_{\Lambda-K}$, and $cos\Theta^{p-B}_{p-\Lambda}$)), and helicity angles (bottom: (from left to right) $cos\Theta^{K-\Lambda}_{p-K}$, $cos\Theta^{\Lambda-p}_{\Lambda-K}$, and $cos\Theta^{p-K}_{p-\Lambda}$)) frames. The black lines show the experimental data and the same distributions (red curve) obtained from PWA fitting of the $pK^+\Lambda$ final state.

6

Results

After the determination of the luminosity and detector acceptance, the differential cross sections can be obtained by

$$\frac{d\sigma}{d\Omega} = \frac{1}{L}\frac{N_{raw}}{A \cdot \epsilon} \tag{6.1}$$

where L is the luminosity, A and ϵ represent the ANKE acceptance and the overall efficiency (including both trigger efficiency and tracking effifiency), respectively. The discussions of the efficiency and acceptance corrections can be found in previous chapters. In this chapter, we focus on the extractions of differential and total cross sections.

6.1 Systematic uncertainty

Four major sources of systematic uncertainties were identified for the present analysis. An obvious one is the uncertainty of the luminosity determination. The second source of systematic uncertainties stems from the determination of the yield with a sizable background subtraction. The acceptance correction itself is the third source

of systematic uncertainties. The last source comes from the tracking efficiency corrections in the Pd, Nd and Fd system.

The systematic uncertainty due to the luminosity determination has been studied previously. In principle the luminosity can be determined by two different methods. However, in the analysis the *pp* elastic scattering method was used in order to be consistent with previous measurements. The major errors in this method come from efficiency corrections in the Fd system, acceptance corrections for *pp* elastic reaction, and momentum reconstructions.

The systematic errors caused by background subtraction were estimated by varying the range of the side-band around the missing-mass peak when fitting the background underneath the signal.

The uncertainties from acceptance corrections were estimated from the differences between the distributions corrected by the models and those corrected by the phase space. As the observed distributions deviate significantly from those based on phase space simulations, such estimations should provide upper limits on these uncertainties.

The errors from the determination of tracking efficiencies mainly come from the momenta spread inside each of the STOP counters [63].

In the case of the total cross section these four systematic uncertainties were added quadratically. While in case of differential cross sections the systematic uncertainties for the determination of the yield and the acceptance correction were investigated in detail for each bin of the observable under consideration.

6.2 The $pp \to ppK^+K^-$ reaction

6.2.1 Differential cross sections at $T_p = 2.57$ GeV

The differential cross section for the $pp \to ppK^+K^-$ reaction at an excess energy of $\varepsilon = 23.9$ MeV is shown in Fig. 6.1 as a function of the K^+K^- invariant mass.

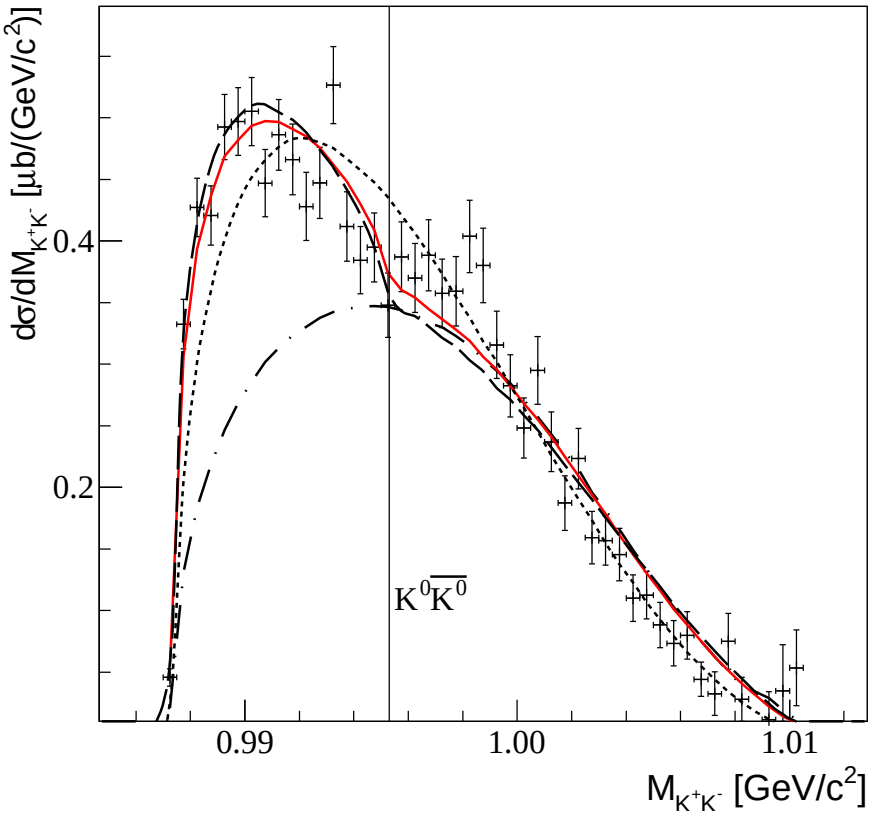

FIGURE 6.1: (Color online) The K^+K^- invariant mass distribution for the $pp \to ppK^+K^-$ reaction at $\varepsilon = 23.9$ MeV. The dotted curve shows the four-body phase space simulation whereas the inclusion of the final state interactions through Eq. 5.1 gives the dashed curve for $a_{K^-p} = 1.5i$ fm and the red solid curve for $a_{K^-p} = 2.45i$ fm. The dot-dashed curve was obtained by considering only the pp and K^-p final state interactions with $a_{K^-p} = 2.45i$ fm.

Also shown are simulations based on a four-body phase space and those distorted by the final state interactions in the K^+K^-, pp, and K^-p systems within the product ansatz of Eq. 5.1. This was done separately with effective scattering lengths of $a_{K^-p} = 1.5i$ fm and $a_{K^-p} = 2.45i$ fm. The most striking features in the data are the strength near the K^+K^- threshold and the dip at $M_{K^+K^-} \approx 0.995$ GeV/c^2, which corresponds precisely to the $K^0\bar{K}^0$ production threshold [96]. This is compelling evidence for a cusp effect coming from the $K^0\bar{K}^0 \rightleftharpoons K^+K^-$ transitions. Similar effects were

observed in $pp \to ppK^+K^-$ by DISTO [47] and by ANKE in $pn \to dK^+K^-$ [176]. Although these enhancements must be due to $K\bar{K}$ final state interactions, including $K^+K^- \rightleftharpoons K^0\bar{K}^0$ charge exchange scattering, they could be connected with some small production of the a_0/f_0 scalar resonances. However, in reality, the data are only sensitive to the $K\bar{K}$ scattering lengths. To investigate this phenomenon in greater detail, the K^+K^- invariant mass distribution was divided by a simulation where only the final state interactions in the pp and K^-p with $a_{K^-p} = 2.45i$ fm were considered.

The best fit to the data is shown in Fig. 6.2. On the basis of the parameters quoted in Table. 5.1, the best fit is achieved with a production of $I = 0$ $K\bar{K}$ pairs in the near threshold region that is about three times stronger than that for $I = 1$. This sensitivity originates mainly from the very different $I = 0/I = 1$ scattering lengths, which is a general feature of the various analyses. This suggests that the production of $I = 0$ pairs is dominant in the $pp \to ppK^+K^-$ reaction, independent of the exact values of the scattering lengths. This finding is consistent with our earlier result [96]. The deviations apparent in Figs. 6.1 and 6.2 at high K^+K^- invariant masses might be connected with the approximations made in our coupled-channel model [96].

Previous analyses of the $pp \to ppK^+K^-$ reaction at different excess energies [177, 63, 83, 103] have all shown a strong preference for low values of the K^-p and K^-pp invariant masses, M_{K^-p} and M_{K^-pp}. To study this further, we have evaluated differential cross sections in terms of these invariant mass distributions and also their ratios:

$$R_{Kp} = \frac{d\sigma/dM_{K^-p}}{d\sigma/dM_{K^+p}},$$

$$R_{Kpp} = \frac{d\sigma/dM_{K^-pp}}{d\sigma/dM_{K^+pp}}. \tag{6.2}$$

The corresponding experimental data and simulations are shown in Figs. 6.3 and 6.4.

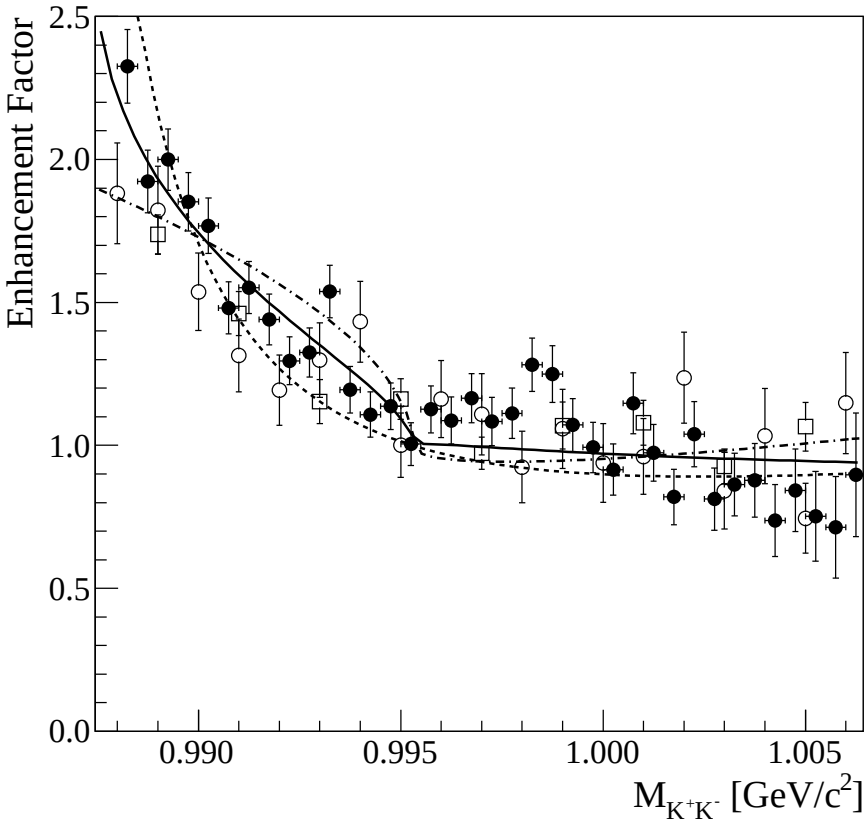

FIGURE 6.2: Ratio of the measured K^+K^- invariant mass distribution in the $pp \to ppK^+K^-$ reaction to a simulation that includes only K^-p and pp final state interactions (shown by the dot-dashed curve in Fig. 6.1). In addition to the current data (solid circles), weighted averages of previous measurements (open squares and circles) are also presented. The solid curve represents the best fit in a model that includes elastic K^+K^- FSI and $K^0\bar{K}^0 \rightleftharpoons K^+K^-$ charge-exchange [96]. The best fits neglecting charge exchange and including only this effect are shown by the dashed and dot-dashed curves, respectively.

Both R_{Kp} and R_{Kpp} display the very strong preferences for lower invariant masses seen in the earlier data. The low mass enhancements in Figs. 6.3c and 6.4c clearly indicate once again that the $pp \to ppK^+K^-$ reaction cannot be dominated by the undistorted production of a single scalar resonance a_0 or f_0. On the other hand, the strength of the K^-p interaction suggests that the kaon pair production might be related to that of the $\Lambda(1405)$ through $pp \to pK^+(\Lambda(1405) \to K^-p)$ [178]. This idea

was put on a quantitative footing by assuming that the $\Lambda(1405)$ was formed through the decay $N^\star \to K^+\Lambda(1405)$ [99]. Within a four-body phase space simulation both ratios should be constant and equal to one and such a simulation also fails to describe the individual M_{Kp} and M_{Kpp} distributions. Whereas the inclusion of a K^-p FSI with an effective scattering length $a_{K^-p} = 1.5i$ fm improves the situation, it overestimates the data in the high invariant mass regions for both R_{Kp} and R_{Kpp}. With the larger effective scattering length $a_{K^-p} = 2.45i$ fm, these ratios, as well as the individual distributions, can be well reproduced. Within the product ansatz of Eq. 5.1 the K^-p final state interaction effectively becomes stronger at lower excess energies. This illustrates the limitations of this simple ansatz to the complex four-body dynamics.

Although the K^-p elastic final state interaction describes well the vast bulk of the data shown in Figs. 6.3 and 6.4, it is interesting to note that there seems to be a small but significant deviation between the K^-p data and simulation in Fig. 6.3b at low invariant masses. Since the $\bar{K}^0n$ threshold is at 1437.2 GeV/c^2, this suggests that the data in this region might also be influenced by $K^-p \rightleftharpoons \bar{K}^0n$ channel coupling.

Due to the low statistics, the COSY-11 data at excess energies of 10 and 28 MeV [83, 103] cannot distinguish between predictions based on effective scattering lengths of $a_{K^-p} = 1.5i$ fm and $a_{K^-p} = 2.45i$ fm. This observation is illustrated for the invariant mass of K^+K^-, R_{Kp} and R_{Kpp} in Fig. 6.5 for an excess energy of 10 MeV. The similar phenomenon is also found at an excess energy of 28 MeV.

6.2.2 Differential cross sections at $T_p = 2.83$ GeV

The corresponding experimental data and simulations at an excess energy of $\varepsilon = 23.9$ MeV are shown in Figs. 6.6 and 6.7. The general features of these results are well reproduced by the simple factorized ansatz of Eq. 5.1. It is nevertheless surprising that the distortions produced by the constant effective scattering length, $a = (0 + 1.5i)$ fm, used at $\varepsilon_{kk} = 51$ MeV [63] still describe the data so well at an

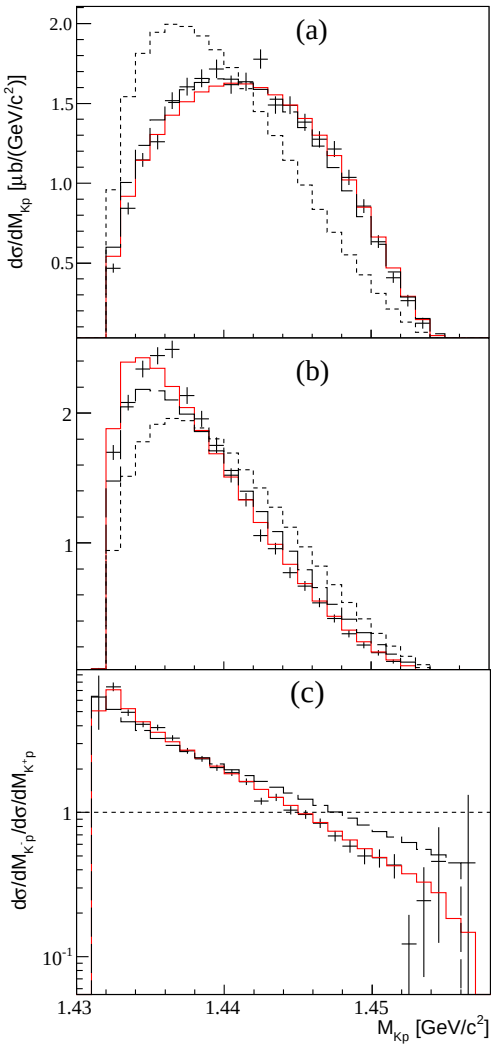

FIGURE 6.3: (Color online) Differential cross sections for the $pp \to ppK^+K^-$ reaction with respect to the invariant masses of K^+p (upper panel) and K^-p (middle panel), and their ratio R_{Kp} (lower panel). The dotted histograms represent the four-body phase-space simulations, whereas the red solid and dashed black ones represent estimations based on Eq. 5.1 that take into account K^-p, pp and K^+K^- final state interactions with $a_{K^-p} = 2.45i$ fm and $a_{K^-p} = 1.5i$ fm, respectively.

excess energy with respect to the K^+K^- threshold as high as 108 MeV, though some deviations are apparent for Kp invariant masses above about 1.5 GeV/c^2.

The similar distortions of Figs. 6.6 and 6.7 also clearly indicate that the direct production of the scalar resonance a_0 or f_0 cannot be the dominant driving mecha-

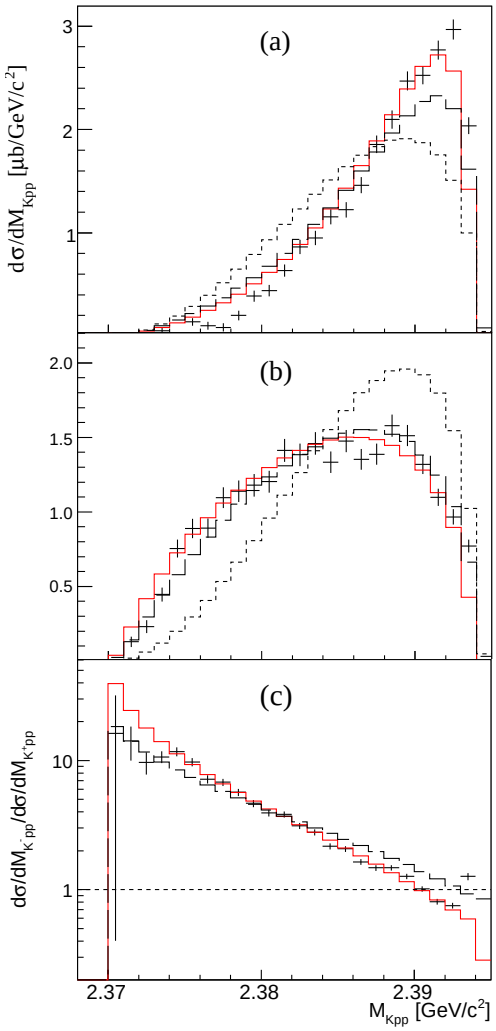

FIGURE 6.4: (Color online) Differential cross sections for the $pp \to ppK^+K^-$ reaction with respect to the invariant masses of K^+pp (upper panel) and K^-pp (middle panel), and their ratio R_{Kpp} (lower panel). The conventions for the theoretical estimates are as in Fig. 6.3.

nism in the $pp \to ppK^+K^-$ reaction.

A combined analysis of previous ANKE data at three energies [96] and the data presented here suggests that, independent of the exact values of the scattering lengths and beam energies, the $K\bar{K}$ enhancement is mainly in the isospin-zero channel. The model for the enhancement factor fitted from [96] has been introduced into the simulation to describe better the data shown in Fig. 6.14 for invariant masses

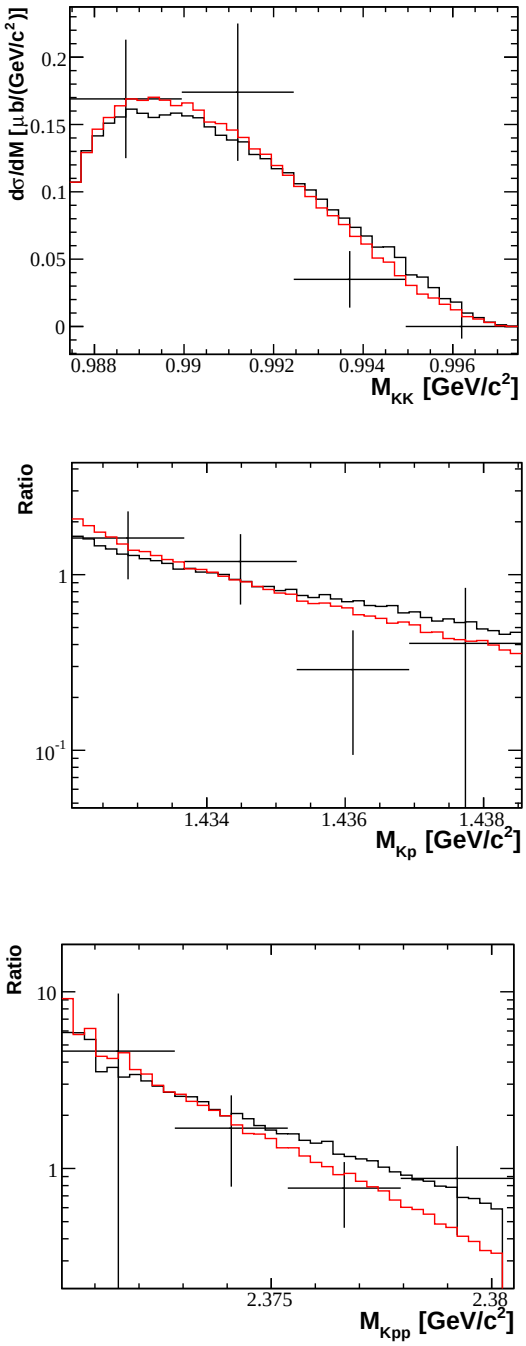

FIGURE 6.5: (Color online) The distributions of the $M_{K^+K^-}$, R_{Kp} and R_{Kpp} for the $pp \to ppK^+K^-$ reaction measured by COSY-11 at $\varepsilon = 10$ MeV, respectively. The red solid cure and black solid ones represent the theoretical calculations taking into account K^-p, pp and K^+K^- final state interactions with $a_{K^-p} = 2.45i$ fm and $1.5i$ fm, respectively.

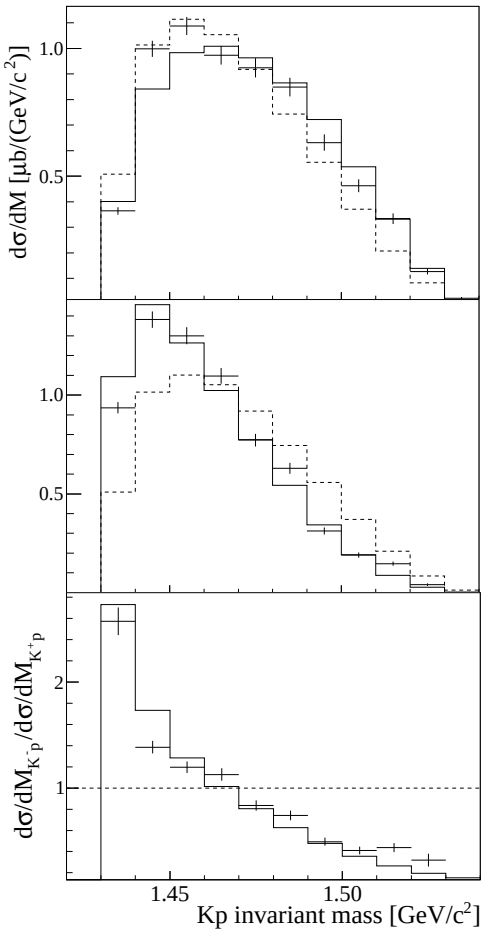

FIGURE 6.6: Differential cross sections for the $pp \to ppK^+K^-$ reaction in the non-ϕ region with respect to the invariant masses of K^+p (upper panel) and K^-p (middle panel), and their ratio R_{Kp} (lower panel). The dashed histograms represent the four-body phase-space simulations, whereas the solid ones represent the theoretical calculations taking into account pp and K^-p final state interactions through Eq. 5.1.

$IM_{KK} < 995$ MeV/c^2. Its effects can be seen more clearly in the plot of the ratio of the K^+K^- invariant-mass data to the simulation based on Eq. 5.1, where no $K\bar{K}$ FSI was included. This, together with the results of previous measurements above ϕ threshold [63], are shown in Fig. 6.8. The two data sets are in agreement and are consistent with the existence of some coupled-channel effect at the $K^0\bar{K}^0$ threshold.

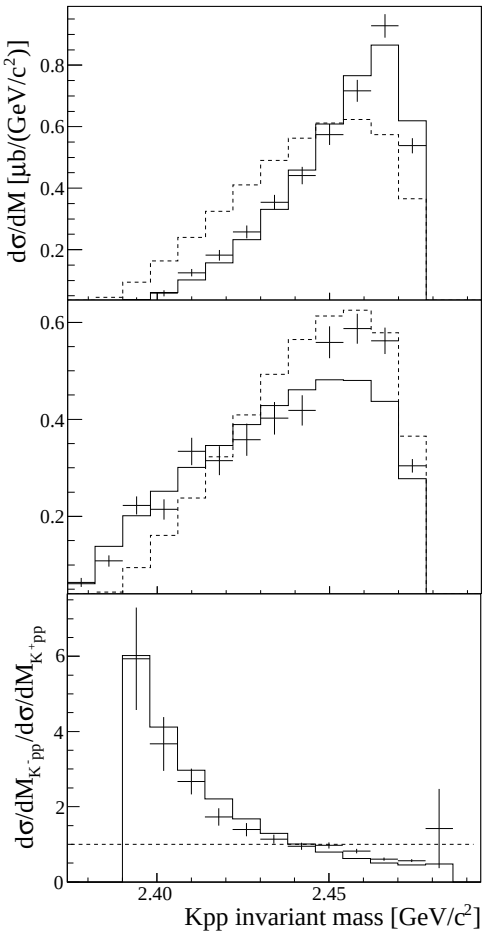

FIGURE 6.7: Differential cross sections for the $pp \to ppK^+K^-$ reaction in the non-ϕ region with respect to the invariant masses of K^+pp (upper panel) and K^-pp (middle panel), and their ratio R_{Kpp} (lower panel). The dashed histograms represent the four-body phase-space simulations, whereas the solid ones represent the theoretical calculations taking into account pp and K^-p final state interactions through Eq. 5.1.

6.2.3 Total cross sections

The acceptance-corrected K^+K^- invariant mass distributions shown in Fig. 6.1 and 6.14 were used to determine the value of the total cross section for ppK^+K^- production, details are discussed in Appendix A. The extracted total cross sections are given in Table. 6.1 for different energies measured at ANKE, where the first error is statistical and the second systematic. The systematic uncertainties considered here arise from the background subtraction, tracking efficiency corrections, luminosity

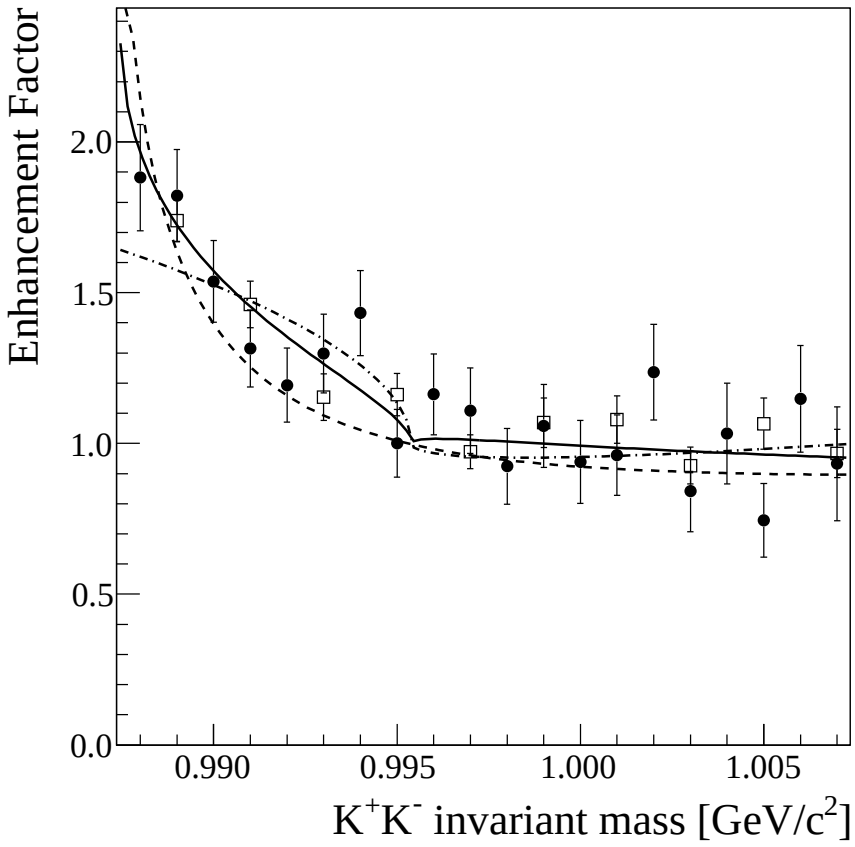

FIGURE 6.8: Ratio of the measured K^+K^- invariant mass in the $pp \to ppK^+K^-$ reaction to estimates based on Eq. 5.1. In addition to the current data (solid circles), the weighted averages of previous measurements (open squares) [63] are also presented. The solid curve represents the best fit in the model of Ref. [96], which includes charge-exchange and elastic K^+K^- FSI. The best fits neglecting charge exchange and including only this effect are shown by the dashed and the dot-dashed curve, respectively.

determination, and acceptance correction.

Our total cross section results are plotted in Fig. 6.9 along with previous measurements from DISTO [47], COSY-11 [83, 103, 104, 105], and ANKE [63]. The new data point at low energy seems high compared to the COSY-11 result at $\varepsilon = 28$ MeV but it should be noted that this value was already increased by 50% compared to that originally quoted [83]. This was achieved through a re-analysis of the data that

Table 6.1: Total cross section for the $pp \to ppK^+K^-$ reaction at different energies measured at ANKE. The uncertainties are, respectively, statistical and systematic. The results of previous measurements [48, 63] are also given.

T_p[GeV]	$\varepsilon_{K^+K^-}$[MeV]	σ[nb]
2.57 [183]	23.9	$6.66 \pm 0.08 \pm 0.67$
2.65 [48, 63]	51	$16 \pm 1 \pm 1$
2.70 [48, 63]	67	$30 \pm 2 \pm 3$
2.83 [48, 63]	108	$98 \pm 8 \pm 15$
2.83 [177]	108	$91 \pm 3 \pm 11.4$

included pp and K^-p final state interactions with $a_{K^-p} = 1.5i$ fm [103]. It is therefore possible that a further increase might follow if the K^+K^- final state interaction were included in the evaluation of the acceptance corrections as well as an effective scattering length of $a_{K^-p} = 2.45$ fm was used instead. There seems to be less sensitivity to the FSI assumptions at $\varepsilon = 10$ MeV, where the original re-analysis only increased the total cross section by 20%.

It is clear from Fig. 6.9 that the four-body phase space cannot reproduce the energy dependence of the total cross section. With the inclusion of the pp, K^+K^-, and K^-p FSI, with an effective scattering length of $a_{K^-p} = 1.5i$ fm, the data above the ϕ threshold can be described well but those at lower energy are significantly underestimated. An increase in the value of a_{K^-p} might help in this region but the coincidence of strong effects in different two- or even three-body channels must also bring the factorization assumption of Eq. 5.1 into question. The dashed line, which represents a calculation within a one-boson exchange model [94], also underestimates the near-threshold data. This model includes energy dependent input derived from fits to the $K^\pm p \to K^\pm p$ total cross sections, though it does not include the pp final state interaction.

The $K\bar{K}$ elastic and charge-exchange FSI both enhance the cross section at low masses ($0.9874 < IM_{KK} < 0.9953 GeV/c^2$) and, since this region represents a larger

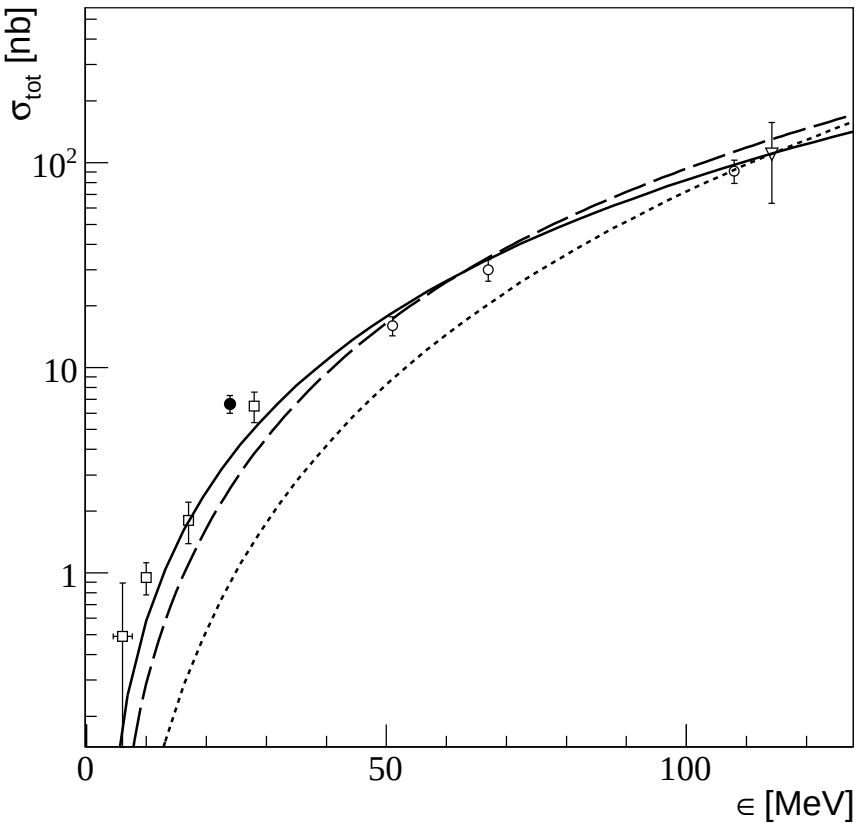

FIGURE 6.9: Total cross section for the $pp \to ppK^+K^-$ reaction as a function of excess energy ε. The present result (closed circle) is shown together with earlier experimental data taken from DISTO (triangle), ANKE (circles), COSY-11 (squares). The dotted line shows the four-body phase space simulation, whereas the solid line represent the simulations with $a_{K^-p} = 1.5i$ fm. The predictions of a one-boson exchange model are represented by the dashed line [94].

fraction of the total spectrum at low excess energies. It is clear that these will also affect the energy dependence of the total cross section. As described before, the $K\bar{K}$ final state interaction approach used here does not rely on knowing the basic production mechanism. Even if one assumed that the major contribution to the cross section came from a combination of a_0 and f_0 production, where these resonances are described by Flatte shapes [184], this would lead to a similar structure to that of the present work in the vicinty of the $K\bar{K}$ thresholds. Thus the observation of cusps

or smooth enhancements at low K^+K^- invariant mass may be due to the formation of these scalar resonances, but should not be taken as evidence.

A full treatment of the dynamics of the four-body ppK^+K^- channel is currently impractical. As a consequence, an energy dependence of a_{K^-p} is possible because this is merely an effective parameter within a very simplistic description of the four-body final state interaction. The strong K^-p final state interaction may be a reflection of the excitation of the $\Lambda(1405)$ in the production process, and it has been suggested [99] that the production of non-ϕ kaon pairs proceeds mainly through the associated production $pp \to K^+p\Lambda(1405)$. This would also lead to deviations from the simple product ansatz for the final state interactions, for example because an attraction between the $\Lambda(1405)$ and the proton would involve three final particles.

The effective K^-p scattering length extracted here can be compared with the scattering length extracted from other experiments. In earlier work, the data for $\bar{K}N$ interactions came from scattering experiments performed from the 1960s to the 1980s. However, the cross section data of K^-p did not constrain the scattering amplitude sufficiently well, so that the extraction of $\bar{K}N$ scattering still suffered from large uncertainties. While the energy shift ΔE and the width Γ of kaonic hydrogen is related to the K^-p scattering length a_{K^-p} via the modified Deser-type relation [81]:

$$\Delta E - i\Gamma/2 = -2\alpha^3\mu_c^2 a_{K^-p}[1 - 2a_{K^-p}\mu_c\alpha(1 - ln\alpha)], \tag{6.3}$$

where $\alpha \simeq 1/137$ is the fine-structure constant and μ_c is the reduced mass. A precise determination of a_{K^-p} is crucial for a reliable subthreshold extrapolation of the corresponding scattering amplitudes. Several previous kaonic hydrogen measurements extracted ΔE and Γ have been published. The data from KEK [78, 185] gives the K^-p scattering length a_{K^-p}:

$$a_{K^-p} = (-0.78 \pm 0.15 \pm 0.03) + i(0.49 \pm 0.25 \pm 0.12) \text{ fm}, \tag{6.4}$$

and the DEAR experiment at Frascati [79, 80].

$$a_{K^-p} = (-0.468 \pm 0.090(stat.) \pm 0.015(syst.)) + i(0.302 \pm 0.135(stat.) \pm 0.036(syst.))\ \text{fm}, \tag{6.5}$$

Taking the recent measurement from SIDDHARTA collaboration [186], which leads to much smaller errors, one obtains:

$$a_{K^-p} = (-0.65 \pm 0.15) + i(0.81 \pm 0.18)\ fm, \tag{6.6}$$

A combined analysis of antikaon-nucleon scattering cross sections and the SIDDHARTA kaonic hydrogen data [187] gives the scattering length for the elastic K^-p channel:

$$a_{K^-p} = (-0.68^{+0.18}_{-0.17}) + i(0.90^{+0.13}_{-0.13})\ fm, \tag{6.7}$$

and the resulting scattering lengths for isospin $I = 0$ and $I = 1$, i.e. a_0 and a_1 are displayed in Fig. 6.10. It should be noted that in our ansatz the neglect of K^+p interaction will cause an extra attraction in the K^-p system, which willcause our K^-p effective scattering length larger than the ones extracted from scattering experiments and kaonic hydrogen data.

6.3 The $pp \to pp\phi$ reaction

6.3.1 Differential cross sections at $T_p = 2.83\ GeV$

As described in sec. 2.2, the $pp\phi$ final state can be defined by two angular momenta, l_1 is the orbital angular momentum of the two nucleons relative to each other, l_2 is the orbital angular momentum of the ϕ meson relative to the two nucleon system. The definition of the threshold energy region is $l_1 = l_2 = 0$, which can be quite broad. In this case, the initial pp system should be in a spin triplet P wave state due to the Pauli principle. Thus the total angular momentum and parity of the system is $J^\pi = 1^-$. Due to parity conservation, the initial angular momentum L must be

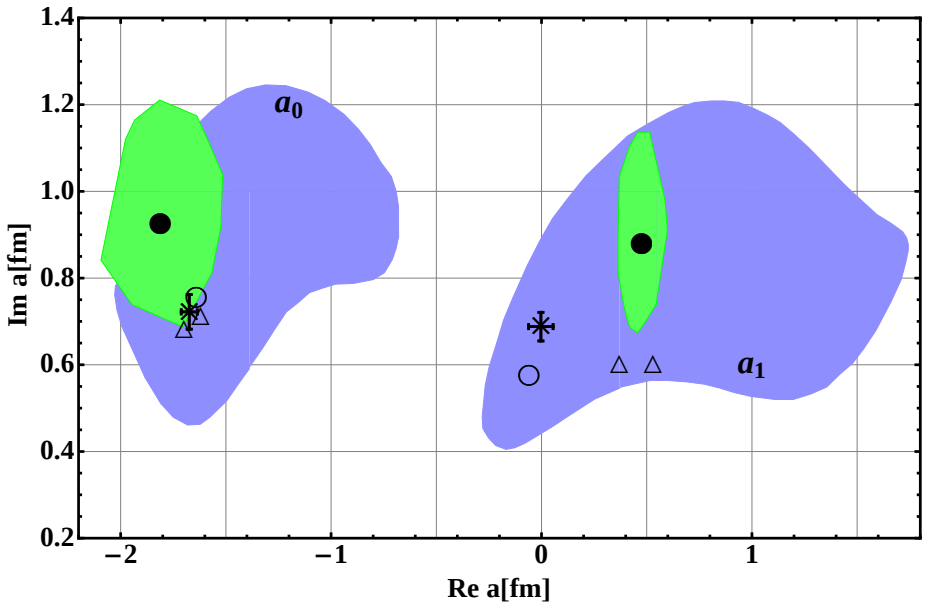

FIGURE 6.10: Real and imaginary part of isospin 0 and 1 $KN \to KN$ scattering lengths. The light shaded (green) areas correspond to the 1σ region of our approach around the central value (full circles). The darker (blue) areas correspond to the 1σ region around central value (empty circle) from Ref. [179]. the cross and empty triangles denote older experimental values from [180] and [181], respectively.

odd, thus the only allowed transition is from an initial state with $L = 1$ and parallel proton spins ($S_{pp} = 1$) to a final state with $S_{pp} = 0$. In this case, the ϕ meson spin must lie along the beam direction. The polar angular distribution of the decay kaons in the ϕ meson rest frame should then display a $\sin^2\theta_\phi^K$ distribution, where θ_ϕ^K is the angle of a daughter kaon from the ϕ decay in the ϕ rest frame. The data collected from ANKE at $\varepsilon_\phi = 18.5$ MeV [48] are consistent with such a dependence and any deviation from this behaviour is a sign of higher partial waves. The isotropic angular distribution of the ϕ meson in the center of mass (c.m.) frame indicates also that the ϕ meson is produced in S wave. While the flat distribution of the proton polar angle in the pp system [48] indicates the pp system $l_1 = 0$.

To test these expectations, the angular distributions for the $pp \to pp\phi$ reaction measured in this experiment and those of DISTO [47] are shown in Fig. 6.11. These

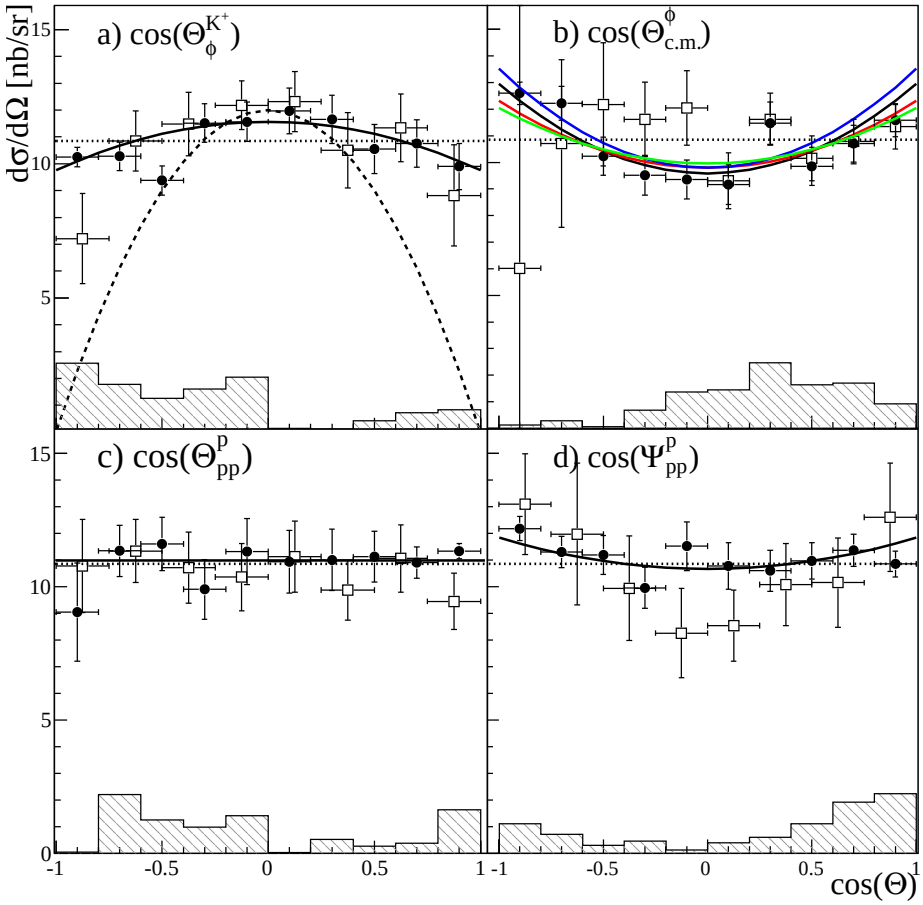

FIGURE 6.11: (Color online) Angular distributions for the $pp \to pp\phi$ reaction (solid circles) obtained in this experiment, where the systematic uncertainties are shown by the hatched histograms, compared with the scaled DISTO data (open squares) [47]. The dotted curves represent isotropic distributions whereas the solid ones show fits to the ANKE results. (a) The distribution with respect to the cosine of the K^+ polar angle in the ϕ rest frame (Decay angle). The dashed curve demonstrates a $\sin^2\theta_\phi^K$ behavior. (b) The distribution in the ϕ polar angle in the overall c.m. system. The blue, red and green curves are typical theoretical predictions from Refs. [182], [36] and [1], respectively. (c) The distribution in the proton polar angle in the pp reference frame relative to the incident proton direction (Jackson angle). (d) The distribution of the proton polar angle in the pp reference frame relative to the ϕ direction (Helicity angle).

distributions must be symmetric about $\cos\theta = 0$ and the data can be parametrized

in the form:

$$\frac{d\sigma}{d\Omega} = a\left[1 + b\,P_2(\cos\theta)\right]. \tag{6.8}$$

where P_2 is the second order of Legendre polynomial. The numerical values of the coefficients obtained from fitting the data are reported in Table 6.2.

Table 6.2: Values of the coefficients of Eq. 6.8 for the K^+ decay angle with respect to the beam direction, the c.m. production angle, and the helicity angle, deduced by fitting the data of ANKE and DISTO [47]. The DISTO data have been scaled by 0.7 in order to allow a direct comparison of the two sets of results.

	ANKE		DISTO (scaled by 0.7)	
	a [nb/sr]	b	a [nb/sr]	b
$\cos\,\theta^K_\phi$	10.96 ± 0.23	-0.11 ± 0.04	10.78 ± 0.50	-0.27 ± 0.08
$\cos\,\theta^\phi_{c.m.}$	10.71 ± 0.21	0.21 ± 0.04	10.81 ± 0.45	0.07 ± 0.07
$\cos\,\Psi^p_{pp}$	11.06 ± 0.22	0.07 ± 0.04	10.64 ± 0.64	0.30 ± 0.14

Quite generally, the differential cross section of the daughter of K^+ from ϕ decay is of the form:

$$\frac{d\sigma}{d\Omega} \propto \left[(1-\rho_{00})\sin^2\theta^K_\phi + 2\rho_{00}\cos^2\theta^K_\phi\right], \tag{6.9}$$

where $\rho_{00} = (1 + b_K)/3$ is a spin density matrix element. From the value of b_K given as b value of $\cos\,\theta^K_\phi$ in Table 6.2 one can see that the ANKE results correspond to $\rho_{00} = 0.30 \pm 0.01$, which is close to the unpolarized value of $\frac{1}{3}$. This is to be compared with the value of $\rho_{00} = 0.23 \pm 0.04$ reported by DISTO at the marginally higher $\varepsilon_\phi = 83$ MeV [47] where, in both cases, only statistical errors are quoted. These results indicate that the higher partial waves play an important role at even relatively modest excess energies. A similar conclusion is reached in a study of the available $pn \to d\phi$ data [102].

The angular distribution of the ϕ meson in the overall c.m. frame shown in Fig. 6.11b is symmetric within experimental uncertainties. The ANKE data show a

stronger anisotropy than those of DISTO, as evidenced by the larger b parameter in Table 6.2, but the error bars of the DISTO data are significant. Theoretical calculations [36, 182, 1] can describe a non-isotropy in the experimental data reasonably well, as shown in Fig. 6.11b. The angular distribution is expected to be isotropic when the mesonic current is dominant, whereas the nucleonic current leads to a $\cos^2\theta$ distribution. The angular distribution might therefore provide some information on the $NN\phi$ coupling constant [27, 36].

It could be interesting to compare our or the DISTO results of Table 6.2 with the analogous measurement at COSY-TOF of the $pp \to pp\omega$ reaction at an excess energy of 92 MeV [64]. Unfortunately, the error bars in the ω angular distribution, $1.0 + (0.23 \pm 0.26) P_2(\cos\theta)$, are too large to draw any useful conclusions as to whether the shapes are similar or not.

The distribution in the proton polar angle measured in the pp reference frame relative to the beam direction is nearly isotropic, as shown in Fig 6.11c. This is consistent with the DISTO results. On the other hand, the analogous observable relative to the ϕ direction shown in Fig 6.11d has some anisotropy. This feature, which was also seen in the DISTO data [47], is evidence for a contribution from a Pp final wave.

In neither the ANKE data at $\varepsilon_\phi = 76$ MeV nor those of DISTO at $\varepsilon_\phi = 83$ MeV is there an indication of any FSI enhancement in the proton-proton relative momentum spectrum. The lack of such an effect can be understood by looking at the momentum distributions of the ϕ meson in the c.m. system and relative momentum distribution of the final protons in the pp reference frame that are shown in Fig. 6.12. The contributions of the different partial waves obtained by fitting Eq. 5.8 to the ANKE data are also indicated. From these one sees that, within the given parametrization, the pp P-wave is completely dominant and this reduces considerably the influence of the $^1S_0$ pp FSI.

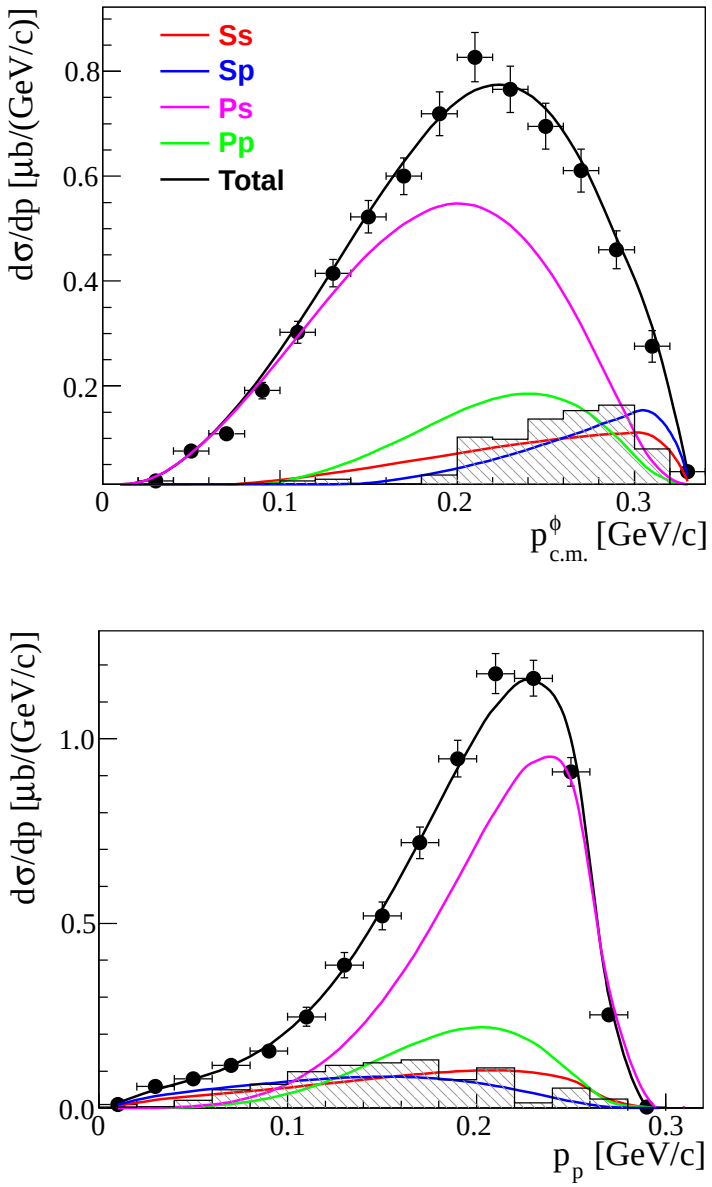

FIGURE 6.12: (Color online) (Upper panel) Differential cross section for the $pp \to pp\phi$ reaction as a function of the momentum of the ϕ meson in the c.m. system. (Lower panel) Differential cross section for the $pp \to pp\phi$ reaction as a function of the proton momentum in the pp rest frame. The systematic uncertainties are shown by the hatched histograms. The curves show the fitted contributions of different partial waves within the parametrization of Eq. 5.8.

The invariant mass distributions of the ϕp system obtained in this experiment and in the previous one at $\varepsilon_\phi = 18.5$ MeV are presented in Fig. 6.13. For both energies the data differ significantly from uniform phase-space predictions (dashed curve). Calculations that include in addition the pp final state interaction (dotted curve) can describe the data at $\varepsilon_\phi = 18.5$ MeV, but fail at $\varepsilon_\phi = 76$ MeV, where the higher partial waves of Eq. 5.8 are successful (solid curve).

6.3.2 Total cross section

Table 6.3: Total cross sections for the $pp \to pp\phi$ reaction at different excess energies. The data have been corrected for the $\phi \to K^+K^-$ branching ratio. The uncertainties are, respectively, statistical and systematic. The results of previous measurements [48, 63] are also given.

T_p[GeV]	ε_ϕ[MeV]	σ[nb]
2.65 [48, 63]	18.5	$33 \pm 2 \pm 4$
2.70 [48, 63]	34.5	$64 \pm 4 \pm 10$
2.83 [48, 63]	76	$133 \pm 12 \pm 27$
2.83 [177]	76	$142.2 \pm 2.1 \pm 17.9$

The acceptance-corrected invariant mass distribution of K^+K^- is shown in Fig. 6.14. This distribution has been used to determine the total cross sections for ϕ production measured in the $pp \to ppK^+K^-$ reaction at 2.83 GeV. The shape of the ϕ contribution is given by the natural line shape of the ϕ meson folded with a Gaussian distribution that takes into account the detector resolution. The total cross sections, together with our previous measurements at different energies at ANKE, are summarized in Table 6.3. The two data sets measured at $\varepsilon_\phi = 76$ MeV are consistent within statistical uncertainties, though the precision of the current one [177] is much higher. It should be noted that the total cross section for ϕ production has been corrected for the branching ratio $\Gamma_{K^+K^-}/\Gamma_{\rm tot} = 0.491$ [5].

The total cross section for the $pp \to pp\phi$ reaction is plotted in Fig. 6.15a alongside other existing near-threshold data [48, 47] as a function of excess energy ε_ϕ. The

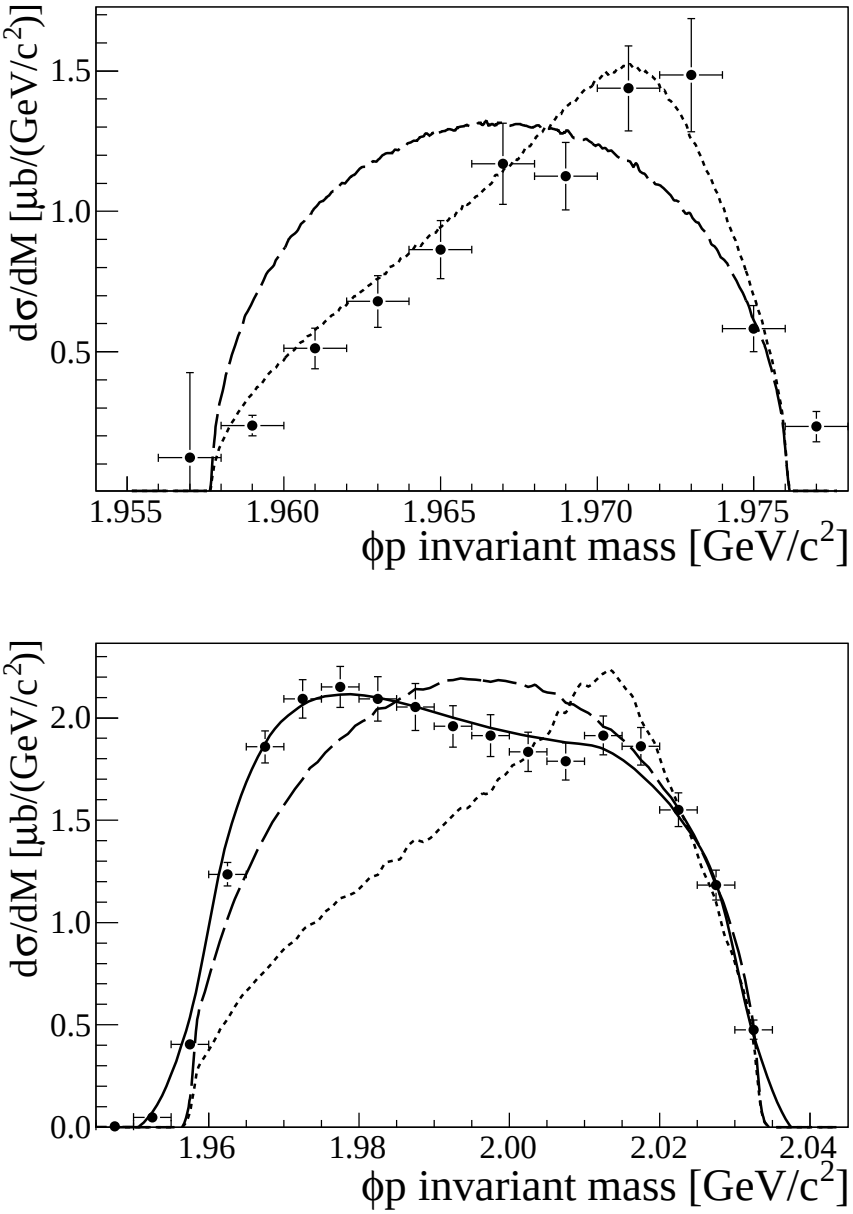

FIGURE 6.13: The acceptance-corrected differential cross section as a function of the ϕp invariant mass at excess energies (a) $\varepsilon_\phi = 18.5$ MeV and (b) $\varepsilon_\phi = 76$ MeV. The dashed curves show phase-space predictions, while the dotted cures include the pp FSI. The solid curve represents the description of Eq. 5.8, with parameters being taken from Table. 5.3.

error bars shown are quadratic sums of the systematic and statistical uncertainties.

If the coefficients $A_{L\ell}$ were constant, apart from the explicit momentum factors in

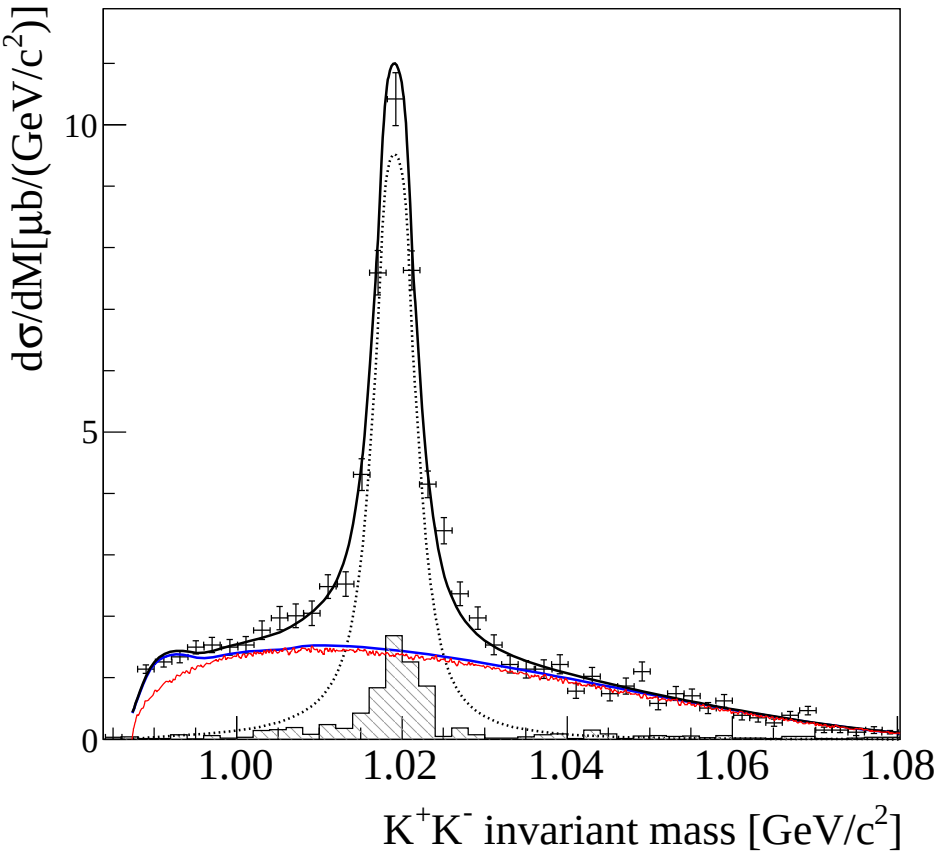

FIGURE 6.14: (Color online) The acceptance-corrected $pp \to ppK^+K^-$ differential cross section as a function of the K^+K^- invariant mass. The error bars indicate only the statistical uncertainties; systematic uncertainties are shown by the hatched histograms. The blue curve shows the non-ϕ contributions within the fitted parametrization, the red curve the four-body phase-space simulation of ppK^+K^-, and the dotted histogram the ϕ contributions. The solid line is the incoherent sum of the ϕ and non-ϕ contributions.

Eq. 5.8, then these could be used to predict the energy dependence of the total cross section. The resulting black solid curve, which by construction passes through the 76 MeV point, underestimates severely the low energy data. This behaviour comes about because at 76 MeV the fit indicates that only a small fraction of the total cross section corresponds to a Ss final state and, as seen in Fig. 6.15a, the contributions from the higher partial waves decrease faster as threshold is approached. It therefore

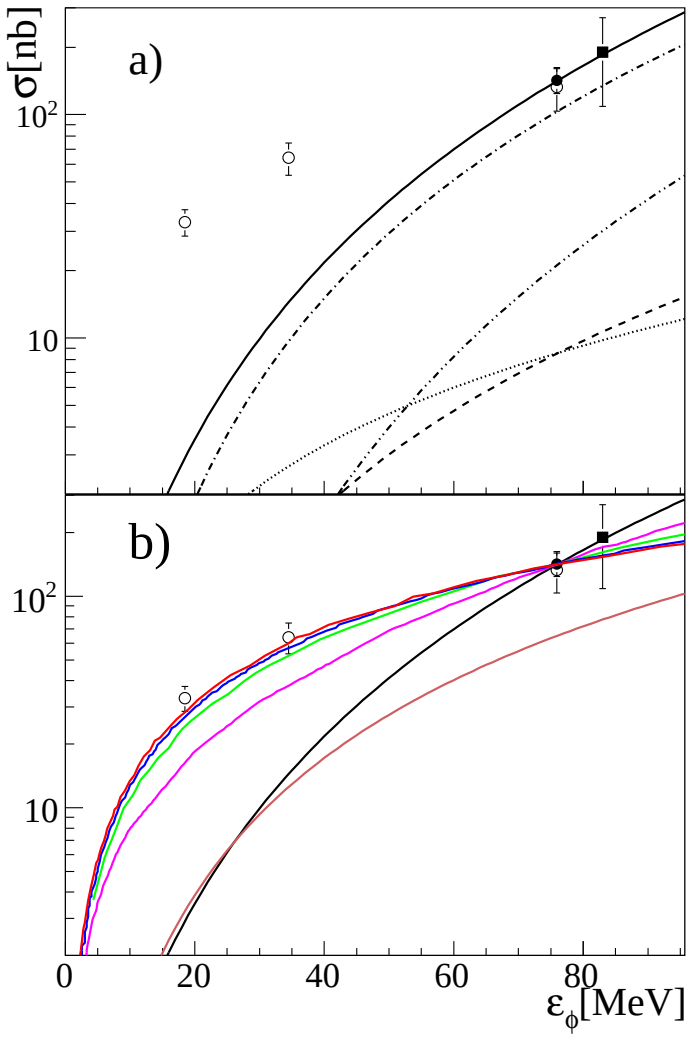

FIGURE 6.15: Total cross section for the $pp \to pp\phi$ reaction as a function of excess energy ε_ϕ. The present result (solid circle) is shown together with experimental data taken from DISTO [47] (solid square) and previous ANKE measurements [48] (open circles). (a) The data are compared to the black solid curve derived using Eq. with the parameters taken from Table. The individual contributions from the Ss (dotted curve), Sp (dashed curve), Ps (dashed-dotted curve), and Pp (double dotted-dashed) are normalized to their predicted values at 76 MeV. (b) The predictions of Tsushima and Nakayama [36] (magenta), scaled to pass through the 76 MeV point, underestimate the low energy data. Also shown are the predictions of Kaptari and Kampfer [182] (green), which are very similar to those of three-body phase-space with the inclusion of the pp FSI, the results within a resonance model Xie [1](blue), and a one-pion-exchange model of Sibirtsev [52] (brown), and this plus exotic baryons [22] (red).

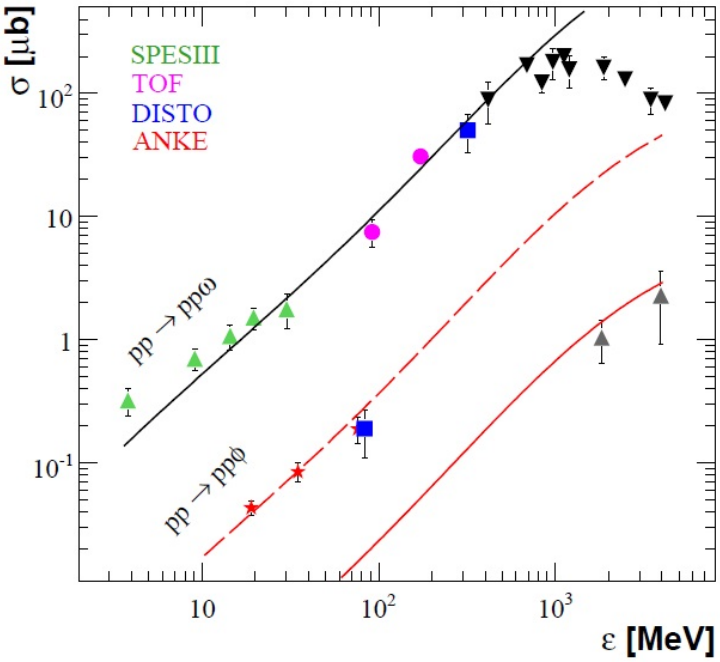

FIGURE 6.16: Total ϕ and ω production cross sections in pp collisions. The three lines show the energy dependence of three-body phase space including the effect of final state interaction normalized to the ω (top) and ϕ (middle and bottom) cross sections.

seems that there must be a strong energy variation in some of the $A_{L\ell}$, which might be driven by a ϕp near-threshold enhancement.

If one ignores the information from the differential distributions derived in this experiment, the energy dependence of the total cross section is close to the predictions from Kaptari and Kämpfer [182], which including mesonic and nuclenoic current contributions are very similar to those of three-body phase space modified by the effects of the pp FSI. This curve can fit most of the data in Fig. 6.15b because, unlike the Ss curve, it takes the full strength at 76 MeV. The model of Tsushima and Nakayama [36] includes also both nucleonic and mesonic current contributions but gives too steep an energy dependence. Both models did not consider contributions from nucleon resonances which, if they existed, would change the energy dependence of the $A_{L\ell}$. Also shown are the predictions of the resonance model of Xie *et al.* [1].

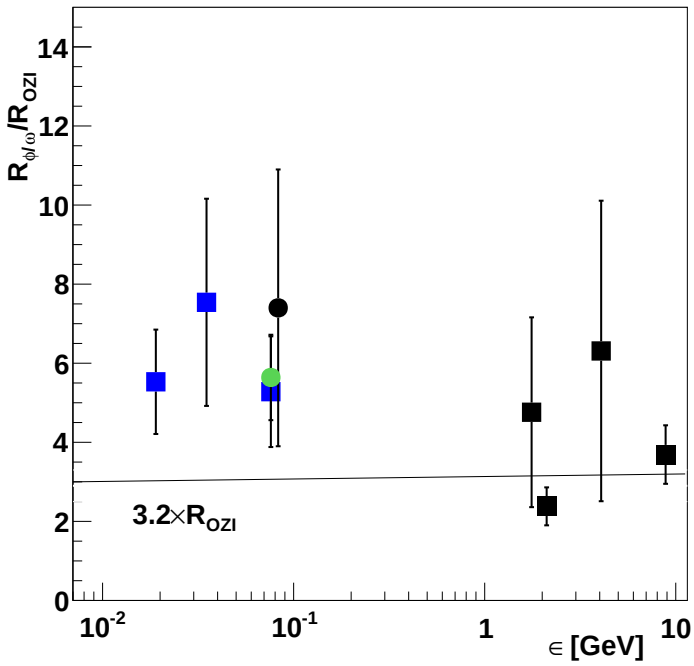

FIGURE 6.17: The ratio of the total cross section of ϕ to ω production in pp collisions.

For ease of comparison, these have all been scaled to pass through the 76 MeV point. On the other hand, the one-pion-exchange calculation [52], which fits the high energy ($\varepsilon_\phi > 1$ GeV) ϕ production results, fails to describe any of the near-threshold data. The model was subsequently extended through the inclusion of baryonic resonances with masses close to the ϕp threshold [22]. This achieves a better description at lower energies, as shown in Fig. 6.15b. It is clear from this discussion that the behaviour of the total cross sections is insufficient by itself to distinguish between different theoretical models; such calculations must be tested against differential spectra of the type presented here.

6.3.3 ϕ/ω ratio

The total cross sections for the $pp\phi$ and $pp\omega$ reactions presented in this thesis is plotted in comparison to the other existing data Fig. 6.16. With the new total cross

section of ϕ meson production, we can investigate further the ratio $R_{\phi/\omega}$ of the total cross sections for ϕ meson to ω meson production by:

$$R_{\phi/\omega} = \frac{\sigma(pp \to pp\phi)}{\sigma(pp \to pp\omega)} \tag{6.10}$$

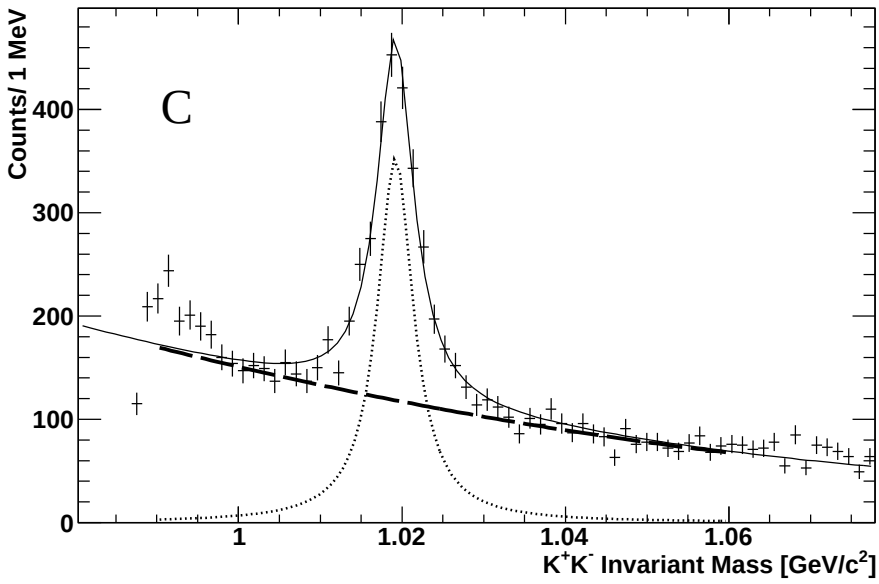

FIGURE 6.18: The K^+K^- invariant mass distributions in pC collision at T_p = 2.83 GeV, not corrected for acceptance. The dotted histogram and the dashed curve represent the ϕ events and the background, respectively.

Taking the recent measurement of the total cross section for ω production at $\epsilon = 92$ MeV with a proper extrapolation, one can get the ratio $R_{\phi/\omega}$ normalized by $R_{OZI} = 4.2 \times 10^{-3}$ to be 5.6±1.1. It is presented as the green circle in Fig. 6.17, together with the other existing data. In theoretical predictions, the coupling of the $\phi\rho\pi$ and $\omega\rho\pi$ ratio should also be equal to R_{OZI}. However, the experimental ratio deduced from πN interaction gives a value of $(3.2\pm0.8)\times R_{OZI}$ [53], which indicates that the decay of $\phi \to \rho\pi$ itself violates OZI rule. Thus, theoretical models based on these coupling constants should give a ratio of $R_{\phi/\omega} \approx 3 \times R_{OZI}$. The experimental

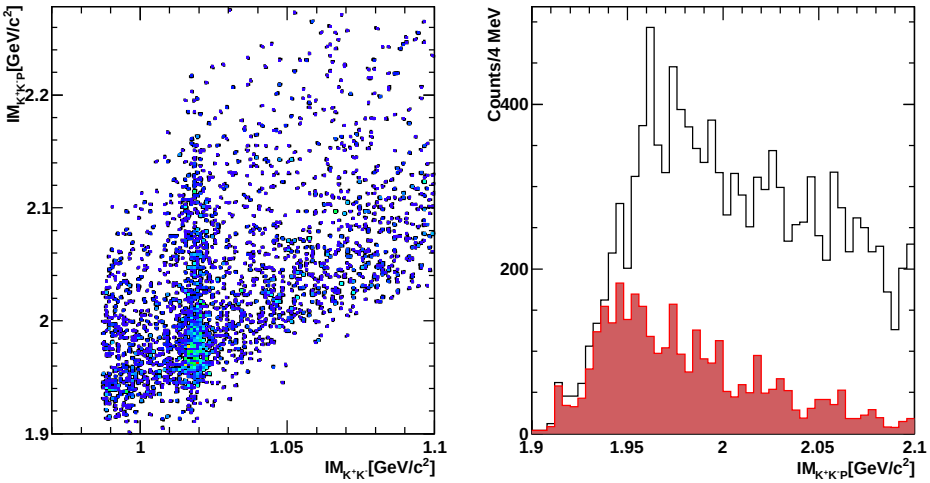

FIGURE 6.19: (Preliminary result) (Left) The plot of the invariant mass of K^+K^-p versus K^+K^- invariant mass. (Right) The invariant mass distribution of K^+K^-p with and without non-ϕ cut $IM_{K^+K^-} < 1.014$ GeV/c^2.

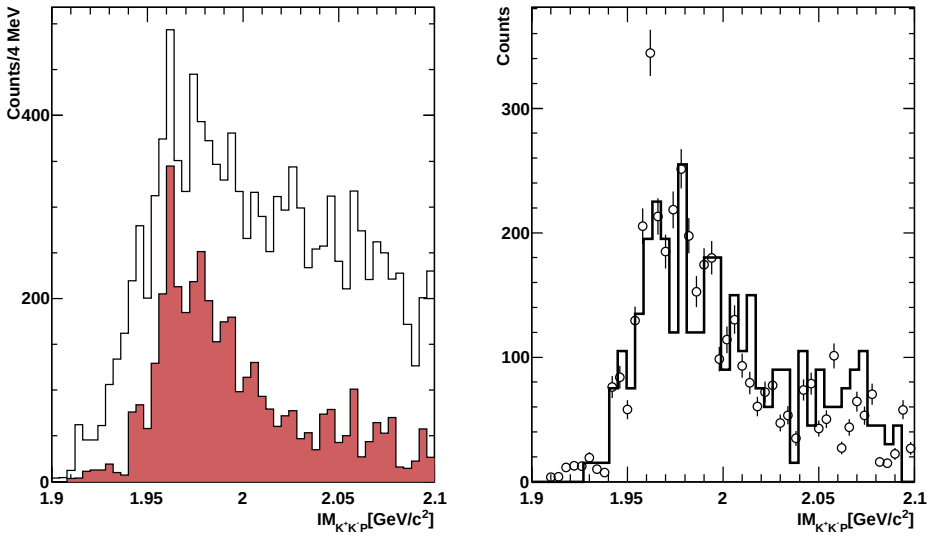

FIGURE 6.20: (Preliminary result) (Left) The invariant mass distribution of K^+K^-p with and without a ϕ cut. (Right) Contributions to ϕ production from two-step processes, no angular distribution taken into account.

measurements show that the ratio at high energies $\epsilon > 1$ GeV is consistent with $3.2 \times R_{OZI}$, whereas the near ϕ threshold R_{OZI} significantly exceeds this value.

The current estimate of the $pp \rightarrow pp\phi$ total cross section at 76 MeV given in Table 6.3 is only a little higher than our previous value [63]. The conclusion drawn there, that the ratio of this to the cross section for ω production is about a factor of six above the OZI limit, is therefore still valid.

6.4 Searching for ϕp bound state in pA reaction

The K^+K^- invariant mass spectra measured at $T_p = 2.83$ GeV in pA reaction look similar for the four targets and the result for ^{12}C target is presented in Fig. 6.18. A clear peak of the $\phi(1020)$ meson sitting on a background of K^+K^- together with a small amount of misidentified events has been observed.

If the produced ϕ meson has a slow velocity, it can interact with another proton and then form a ϕp bound state [15], which decays into a K^+K^-p final state. One can perform a triple coincidence detection of kinematically correlated K^+, K^- and proton using the same technique for pp collisions. In order to identify clearly the signal of a ϕ-N bound state, other possible background contributions to the K^+K^-p final state should be studied carefully. The study [20] shows that the dominant background contribution is the reaction channel, in which a ϕ meson decays into K^+K^- without the formation of a ϕ-N bound state. In order to remove such a background, a detailed Monte Carlo simulation has been carried out, which shows that additional cuts on the momentum correlation between proton and $K^{\pm}$, and the invariant mass of the K^+, K^- and proton system can clearly separate the signal of a ϕ-N bound state from the backgrounds.

Fig 6.19 shows the invariant mass of K^+K^-p versus K^+K^- invariant mass distributions, and the invariant mass distribution of K^+K^-p without and with a cut on the $IM_{K^+K^-} < 1.014$ GeV/c^2. Due to the loose binding, a ϕ-N bound state may directly decays into K^+K^-p which requires the K^+K^- pair stem from non-ϕ region. Moreover, if one assume that the binding energy of ϕ-N bound state is 1.8 MeV,

the corresponding ϕ-N mass should be around 1.956 GeV/c^2. However, no obvious evidence in current analysis indicates the existence of a ϕ-N bound state due to the low statistics. Anyhow, the corresponding invariant mass distribution of ϕp has also been investigated. A cut on the ϕ region (1.014<IM$_{K^+K^-}$ <1.024 GeV/c^2) is applied, the invariant mass of K^+K^-p is shown in Fig. 6.20, the shaded area represents ϕp events after cuts.

It should be noted that sizeable excesses have been observed in the numbers of ϕ mesons produced with momenta below 1 GeV/c [25]. These are not reproduced by the models employed and might suggest some enhancement in the low mass ϕN systems. In order to get a deeper insight about the ϕ-N bound state, more theoretical calculations and experimental data are required.

7

Summary and outlook

We have presented the differential and total cross sections for the ϕ meson and non-ϕ kaon pair production at a beam energy of T_p =2.83 GeV, as well as those for kaon pair production at T_p =2.57 GeV. All the reactions were identified through a triple coincident detection of a K^+K^- pair and a forward-going proton in the COSY-ANKE magnetic spectrometer, with an additional cut being placed on the missing mass spectrum.

The main feature of the non-ϕ data is the very strong distortion of both the K^-p and K^-pp spectra by the K^-p final state interaction. Such distortions are even stronger in the low energy data, and can be explained quantitatively within an effective K^-p scattering length $a_{K^-p} = 2.45i$ fm. This is to be compared with the $1.5i$ fm obtained from the analysis of data measured above the ϕ production threshold. A full treatment of the dynamics of the four-body ppK^+K^- channel is currently impractical. As a consequence, an energy dependence of a_{K^-p} is possible because this is merely an effective parameter within a very simplistic description of the four-body final state interaction. The strong K^-p final state interaction may be connected with the $\Lambda(1405)$ in the production process and it has been suggested [99]

that the production of non-ϕ kaon pairs proceeds mainly through the associated production $pp \to K^+p\Lambda(1405)$. This would also lead to deviations from the simple product ansatz for the final state interactions, not least because an attraction between the $\Lambda(1405)$ and the proton would involve three final particles.

Our results also show a very strong preference for low K^-pp masses and this effect seems to be even more pronounced than in the higher energy data [63, 177]. Although this might be connected with the ideas of a deeply bound K^-pp state [128, 109, 111, 129], it must be stressed that our data were measured far above threshold. They should not therefore be taken as necessarily implying that the K^- will bind with two protons.

There is strong evidence for a cusp effect arising from the $K^0\bar{K}^0 \rightleftharpoons K^+K^-$ transitions. Our analysis within a coupled-channel description suggests that, with the values of the $K\bar{K}$ scattering lengths used, the production of isospin-zero $K\bar{K}$ pairs dominates. Though this is consistent with results extracted from data taken above the ϕ threshold [96, 177], there is clearly room for some refinement in the model. On the other hand, the structure of the K^-p invariant mass spectrum in the 1437 MeV/c^2 region suggests that there might be important coupling also between the K^-p and $\bar{K}^0n$ systems.

It is evident that the interactions in the four-body ppK^+K^- final state are extremely complex. Nevertheless, the energy dependence of the total cross section can be well described above the ϕ threshold by introducing the effects of the pp, K^+K^- and K^-p final state interaction with an effective scattering length of $a_{K^-p} = 1.5i$ fm. This would, however, have to be increased to have any hope of fitting the lower energy data. Further theoretical work is required to clarify the reaction mechanisms.

Having a good description of the background, it was possible to derive detailed invariant mass and angular distributions for the $pp \to pp\phi$ reaction. Although the DISTO collaboration [47] showed the significance of higher partial waves at the

marginally higher excitation energy of $\varepsilon_\phi = 83$ MeV, they did this mainly on the basis of relative momentum spectra. Their conclusion is confirmed unambiguously by the angular distributions presented in this thesis. For example, at $\varepsilon_\phi = 18.5$ MeV the ϕ-meson is completely aligned, as it has to be in a Ss final state [48]. In contrast, in the present data the emerging ϕ is almost unpolarized and this clearly signals the presence of higher partial waves. This is consistent with the evidence from the momentum distributions, which also show the dominance of P waves in the final pp system. This explains why the $^1S_0$ pp FSI, which is so important at $\varepsilon_\phi = 18.5$ MeV [48], is not observed at 76 MeV. Furthermore, in contrast to the DISTO result [47], clear anisotropy was observed in the ϕ c.m. angular distribution and this can be ascribed to the contribution from p wave. This angular distribution might provide information on nucleonic current contributions and the $NN\phi$ coupling constant [27, 36].

Even if one considers only a few partial waves, there are simply too many parameters to perform useful fits and only typical Ss, Sp, Ps, and Pp contributions were considered in Eq. 5.8. The fitted data show that the contribution of the final Ss wave to the cross section represents only a small amount of the total at $\varepsilon_\phi = 76$ MeV. As a consequence, the extracted parameters predict a total cross section that grossly underestimates the measurements at lower energies.

The simplest way out of the total cross section dilemma would be to assume that a ϕp threshold enhancement leads to a significant energy dependence of some of the $A_{L\ell}$ coefficients. In this context it is interesting to note that the large contribution of the Pp wave to the $pp \to pp\eta$ cross section at an excess energy of 72 MeV was ascribed to a strong ηp FSI driven by the $N^*(1535)$ isobar [188]. Against the ϕp enhancement hypothesis is the fact that the large excess of events in the ϕp invariant mass distribution at low masses can be explained in the partial wave fitting of Eq. 5.8, without including any ϕp enhancement. We have not, however, shown that the fitting

of the data is unambiguous and there could be other truncated partial wave forms that might be equally successful. Furthermore, from the start we have not included any final state interaction between ϕ and protons in the parametrization. There could therefore be a possible trade-off between some of the partial wave parameters and an FSI in the ϕp system. Nevertheless, the phenomenological parametrization is sufficient for acceptance correction and it describes well most of the differential distributions.

In the parametrization of Eq. 5.8, the coefficients $A_{L\ell}$ were taken to be constant and no resonance effects were included. Recent theoretical studies have suggested that bound states or resonances might be formed in the near-threshold ϕp system [15, 129] and, if so, they would certainly influence the behaviour of some of the $A_{L\ell}$. In this context, it is interesting to note that a bump was observed in the near-threshold ϕ meson photoproduction from hydrogen by LEPS [189] and in the preliminary results of CLAS [190]. Furthermore, it seems that s-wave production of the ϕ in the $pd \to {}^3\mathrm{He}\,X$ reaction is anomalously large compared to the ω and η' mesons [191]. Such effects might even be part of the explanation for the violation of the OZI rule in the ratio of ϕ to ω production. Alternatively, it is possible that other strangeness production channels could influence the energy dependence of the $pp \to ppK^+K^-$ reaction [192, 193, 194].

Although some theoretical models have been able to describe *a posteori* the published total cross sections for ϕ production, calculations of differential distributions with which to compare our experimental data are rather limited. It is only when a model is tested against a range of differential distributions, as presented here, that some credence can be given to the model. Total cross sections are insufficient and more theoretical work is therefore required.

Appendix A

M_{inv}^{KK} distribution

The K^+K^- invariant mass distribution for the reaction $pp \rightarrow pp\phi \rightarrow ppK^+K^-$ is given based on the phase space model,

$$\begin{aligned}\frac{d\sigma}{dm_{KK}} &= \frac{1}{2^{14}\pi^8 p_i^{cm} S_i}\int_{2m_p}^{\sqrt{S}_i - m_{KK}} |\mathrm{M}|^2 P_{KK} P_p P_K \; dm_{pp} \; d\Omega_{KK} \; d\Omega_p \; d\Omega_K \\ &\times \frac{\Gamma_\phi}{2\pi}\frac{1}{(m_{KK}-m_\phi)^2 + \Gamma_\phi^2/4}, \end{aligned} \tag{A.1}$$

where M is the invariant ampitude.

P_{KK} P_p and P_K denotes the momentum of the KK system in the initial center of mass system, the relative momentum of final protons and the relative momentum of kaons, respectively, and is given by

$$\begin{aligned} P_{KK} &= f(\sqrt{S}_i, m_{pp}, m_{KK}), \\ P_p &= f(m_{pp}, m_p, m_p), \\ P_K &= f(m_{KK}, m_k, m_k), \end{aligned}$$

where $f(M, m_1, m_2) = [(M^2 - (m_1+m_2)^2)(M^2 - (m_1-m_2)^2)]^{1/2}/2M$.

The normalization of M to the invariant amplitude M_ϕ of the reaction $pp \to pp\phi$,

$$|M|^2 = \frac{4\pi^2}{P_K^\phi}|M_\phi|^2,$$

where P_K^ϕ denotes the momentum of decayed kaon in the rest frame of ϕ-meson.

Appendix B

Summary of non-thesis work

In addition to the subject of this thesis on experiments performed at COSY-ANKE, I was also involved in three experiments carried out at the High Intensity γ-Ray Source (HIγS) facility located at the Duke University Free Electron Laser Laboratory (FEL). The first one was a beam test of Compton scattering from ^3He, which was carried out in March 2013. The second was the three-body photodisintegration of ^3He with double polarizations. And the last one was a beam test of two-body photodisintegration of ^3He. The following sections provide a summary of these three experiments. This section focuses on the design and build of a solenoid target, which was mostly designed and built by me, as well as the beam test for Compton scattering from ^3He.

B.1 Polarized ^3He Targets

Naively, one would use a neutron target to study the structure of the neutron. However, due to the short lifetime (less than 15 minutes), no stable free neutron targets exist in nature. Instead, a polarized ^3He target has been used as an effective po-

larized neutron target because of its unique ground state spin structure (two proton spins cancel each other). In the ground state, the spin of polarized ^3He is carried mostly by the neutron.

The polarized ^3He target is based on the principle of spin exchange between optically pumped alkali-metal vapor and noble-gas nuclei [195, 196, 197]. The polarized ^3He target is a glass cell that contains 6-7 atmospheres of ^3He gas. To improve the optical pumping efficiency, a small quantity of N_2 was used as a buffer gas. The cell is separated into two chambers: a pumping chamber and a target chamber. The cylindrical target chamber has a length of 40 cm. The ^3He target has to be placed in a homogeneous holding magnetic field during the optical pumping. The magnetic fields gradients can contribute to the depolarization of polarized ^3He.

In our labs, there are two different methods to provide the uniform magnetic field: one method is using Helmholtz coils, the other one is via solenoid. The Helmholtz coils were used in the experiments of Three- and Two body photodisintegration of ^3He, while the solenoid was designed for Compton scattering from ^3He.

B.2 Compton Scattering on ^3He

B.2.1 Motivation

Understanding the nucleon structure is one of the major goals of nuclear physics. Electric and magnetic polarizabilities of the nucleon are quantities which describe the response of the nucleon to an external electromagnetic field. These two polarizabilities are named α_E and β_M, indicating the ability of the nucleon to produce induced dipole moments under the external electric and magnetic field. Another set of fundamental quantities related to the nucleons structure are nucleon spin polarizabilities, which characterize the stiffness of the nucleon spin. These quantities can be studied by polarized Compton Scattering on nucleons. Especially, double polarized Compton Scattering from ^3He provide a tool to extract the neutron polarizabili-

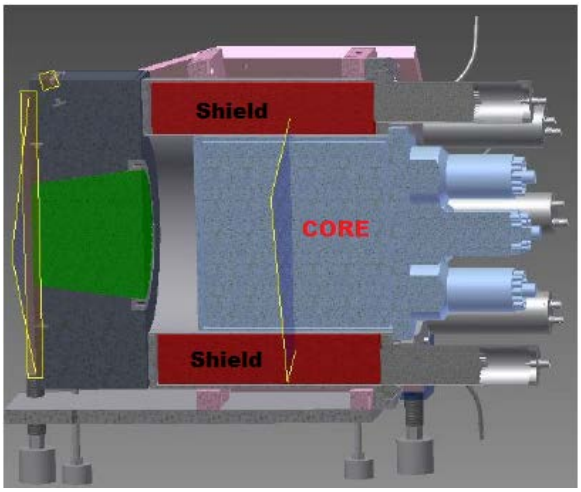

FIGURE B.1: (Color online) One NaI detector with core-and-threshold structure for rejecting comsimic events.

ties [198]. Such an experiment has been proposed at a photon energy of 125 MeV at HIγS with circularly polarized photons on a high-pressure polarized ^3He target. The scattered photons were detected by the HIγS NaI Detector Array (HINDA), which consists of eight NaI detectors (16.25 in.(diameter) and 12 in. (length)). One NaI detector is shown in Fig. B.1

B.2.2 Experimental apparatus

The Helmholtz coils will not be used in this experiment in order to position the NaI detectors near the polarized ^{3}He target. A single layer solenoid is therefore developed to provide the holding field for the polarized ^{3}He target.

The solenoid is in a single layer configuration and wound around 106 cm long PVC pipe (40.64 cm in diameter) by using 1.02 mm copper wire (AWG 18). The number of turns of the solenoid is 1000. The coil winding system is established in the machine shop of Physics department. After the winding, we applied epoxy to glue the wire together.

For mapping the magnetic field (Bx, By, Bz) inside the solenoid, a magnetic field mapper is designed by using a motor-system, a Gaussmeter, two different probes

(one is for Bz, the other for Bx (By)) and a data acquisition system, see details in [199]. The probes are placed on an non-magnetic arm, and the arm is capable of incremental three-axis motion by using a three-axis motor. With the motor, the probes can scan different points in space by step of 0.5 in. Inside the solenoid, the cylindrical axis of the target chamber is not the same as the axis of the solenoid, the offset is about 6.12 cm. A cuboid which includes the target chamber and pumping chamber is scanned as region of interest (ROI). The whole system is controlled by a PC which can store the magnetic field values and position coordinates (x, y, z) into a file for future analysis.

A pair of Tungsten collimators was employed in the experiment. The goal of the target collimators is to shield photons generated from the target windows, which are major background contributions to the elastic Compton scattering events. Each collimator is a 9.5 cm long tube with 7.2 cm (2.83 in.) outer and 3.2 cm (1.26 in.) inner diameter. The inner diameter is 0.2 cm larger than the diameter of the target chamber, so that we can move the collimators without scratching the cells.

Considering the limited space inside the solenoid, a careful and feasible design of the target system is developed. Fig B.2 shows the conceptual design of the ^{3}He target system. The support design for this target system is not shown here since it depends on the design of the table for the HINDA system. During the experiment, a ^{3}He target cell and a N_2 reference cell (a cell used for background measurement, has the same dimension of the target cell but filled with N_2 instead of ^{3}He) can move up and down together with the solenoid, in and out of the γ-ray beam by a motor-controlled support.

A combination of rails and bearing balls are used to move each collimator along the target chamber axis in the horizontal plane by using another motor system. In this way, we can switch between two different sets of target cell with collimators and reference cell with collimators to study the signal and background. The collimator

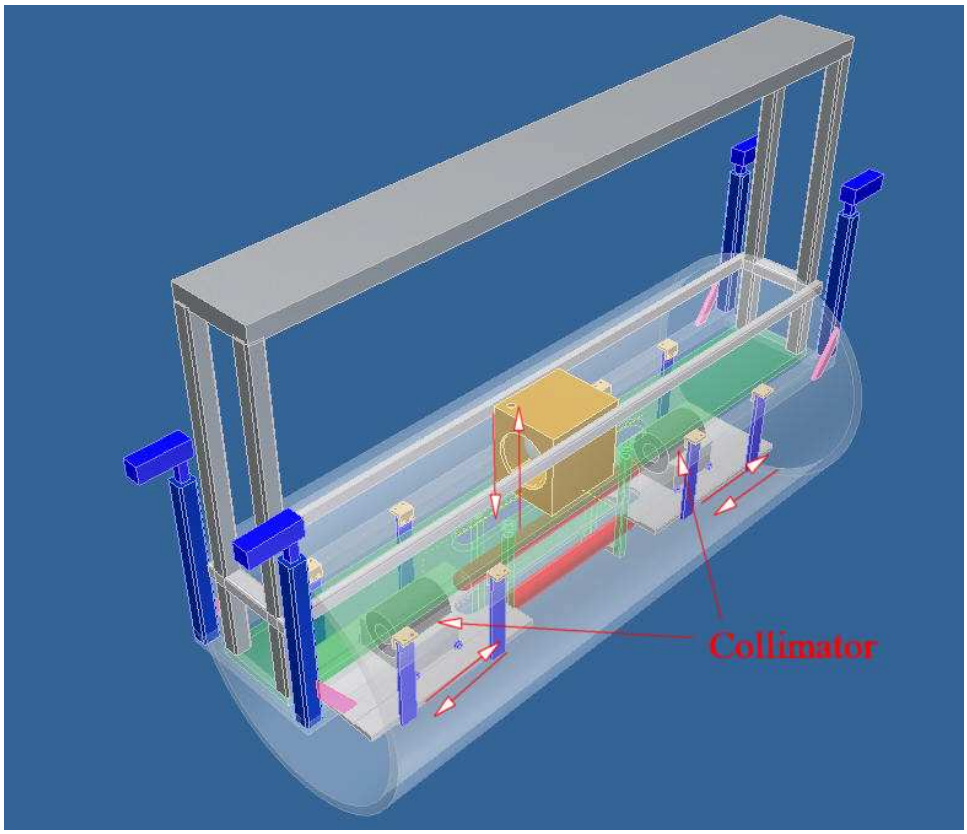

FIGURE B.2: (Color online) The design of ^3He target system for the Compton Scattering experiment.

movements are labeled as arrows shown in Fig. B.2. In order to make the alignment simple, we plan to align the target cell, reference cell and collimators without the solenoid with lasers first. After the alignment, the solenoid is in to the designed position with the target system inside, instead of moving the aligned cells and the collimators.

The new target system has been built in our lab, as shown in Fig. B.3.

B.2.3 Beam test

In the experiment, background contributions need to be taken care of, such as the cosmic radiation, scattering photons from the air and the target windows, and scattered photons from N_2 in the target cell and so on. In order to understand the

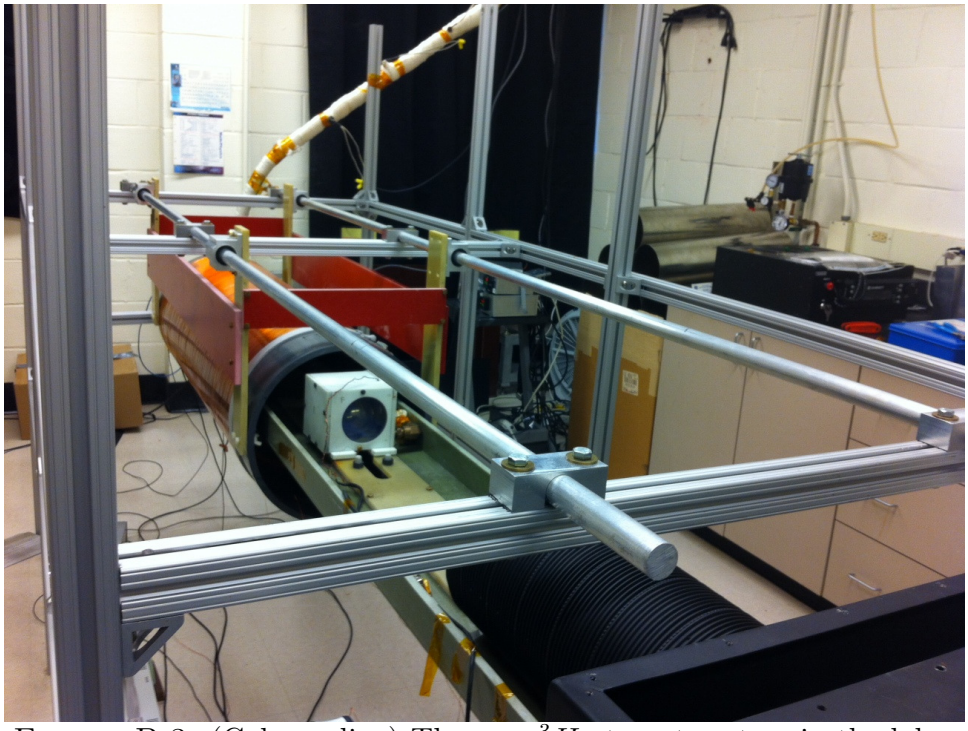

FIGURE B.3: (Color online) The new ^3He target system in the lab.

background contributions, a 60 hours beam test was performed at 87±4 MeV in March 2013. In the beam test, an unpolarized ^3He target cell was used. The average beam flux was $6.7 \times 10^6 \gamma/s$. Six NaI detectors were positioned at three angles (40°, 87°, and 130°).

In order to suppress backgrounds, several apparatus were installed. Tungsten collimators were placed around both ends of the target chamber in order to reject the scattered photons from the target windows. Lead walls were positioned upstream of the target to suppress the beam induced background. Vacuum pipes were used to reduce the scattered photons from the air. The pulse-nature of the beam time structure and anti-coincident measurements between NaI core and shield were used to remove the cosmic events. The beam test data were analyzed by X. Yan and S. Jawalkar. The result is shown in Fig. B.4.

The Compton events are expected between 80 and 90 MeV in the NaI core.

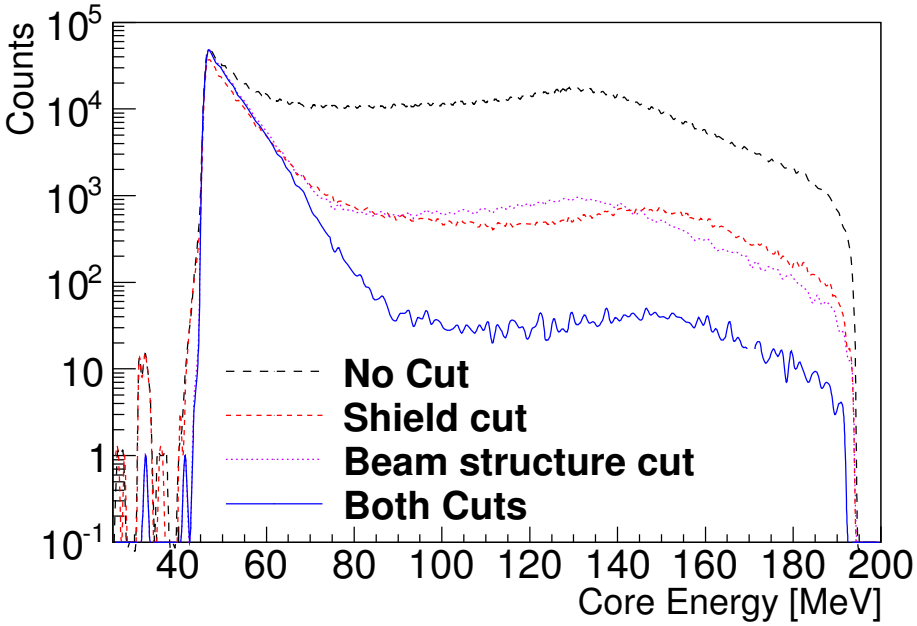

FIGURE B.4: (Color online) ^3He run data in one NaI detector at 40°. Blac line: no cut applied. Red line: only an anti-coincidence-shield cut applied. Magenta line: a cut of beam-time-stucture applied. Blue line: with both cuts [202].

Considering the low cross section of Compton scattering, eight events are expected in the test configuration. Therefore, the result is consistent with our expectation, and indicates that we have a good control of the background. Further study [202] shows that the major contribution comes from cosmic radiation.

Therefore, additional criteria are required to reject cosmic background in order to observe Compton events. Moreover, high photon flux is crucial and necessary for perform the double polarized experiments.

B.3 Three-body photodisintegration of ^3He

The three-and two body photodisintegration of ^3He experiments are the thesis projects of G. Laskaris. I have wrote the basic codes for Geant4 simulations of both Three-body and two-body reactions. Moreover, I also involved in the data analysis of three-body experiment, and took shifts for the beam test of two-body experiment.

All the data and figures shown in this and next section are from G. Laskaris.

B.3.1 Motivation

The three- and two body photondisintegration of ^3He with double polarizations are important in testing state-of-the-art three-body calculations [203]. The spin-dependent total cross sections from the photodisintegration of ^3He below pion production threshold are of further importance for investigating the Gerasimov-Drell-Heam (GDH) sum rule [200, 201].

B.3.2 The Experiment

The measurements of three-body photodisintegration of ^3He using a longitudinally polarized ^3He target and a circularly polarized γ-ray beam with beam energies of 12.8 and 14.7 MeV. A schematic view of the experimental apparatus including the ^3He target and detector system is shown in Fig. B.5. A high-pressure ^3He cell was employed as a target. The target cell was a one-piece glassware made of Pyrex glass. The Helmholtz coils were used to providing the holding field for the target system. Sixteen liquid scintillator detectors were used to detect the neutrons generated from the three-body photodisintegration of ^3He. These detectors were positioned 1 m away from the center of target at angles of 30°, 45°, 75°, 90°, 105°, 135°, 150°, and 165°. μ-metal tubes were used around the photomultiplier tubes to shield the outside magnetic field. A cylindrical D_2O cell along with two neutron detectors was employed to monitor the flux of γ-ray [203].

The selection of the neutron events from ^3He was based on cuts on the Pulse Height (PH), time-of-flight (TOF), and Pulse shape discrimination (PSD) values. A PSD cut was first applied to the ^3He target data to remove photon events. Then, a PH cut was applied to determine the detector efficiency. The same cuts were applied to the data taken with the N_2 reference cell to subtract the background. The neutron

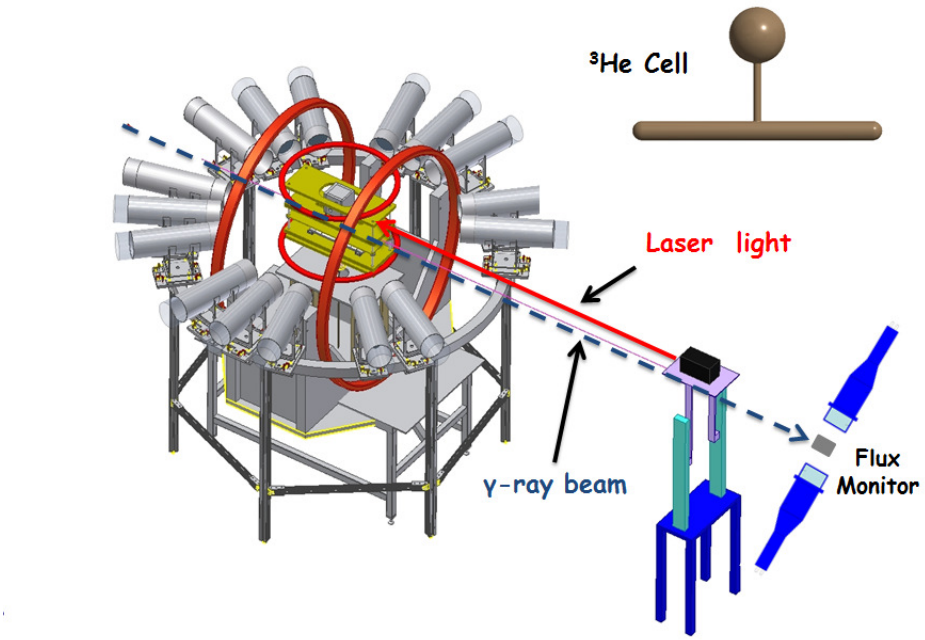

FIGURE B.5: (Color online) Shematic view of the experimental apparatus.

detection efficiency varies rapidly as a function of neutron energy below 1.5 MeV. Therefore, we report cross sections only for neutrons with energies above 1.5 MeV as defined by the TOF cut [203].

B.3.3 Results

Figs. B.6 shows the spin-dependent double-differential cross sections at an incident photon energy of 12.8 MeV as a function of the neutron energy at lab angles of 75 °, 90 °, and 105 °. The dashed and solid curves are the GEANT4 simulation results using as cross section inputs the calculations provided by Deltuva *et al.* and Skibiński *et al.*, respectively. The band in each panel shows the overall systematic uncertainties combined in quadrature. The spin-dependent double differential cross sections for the rest of the scattering angles will be presented in a future publication. The results for a photon energy of 14.7 MeV can be found in [203].

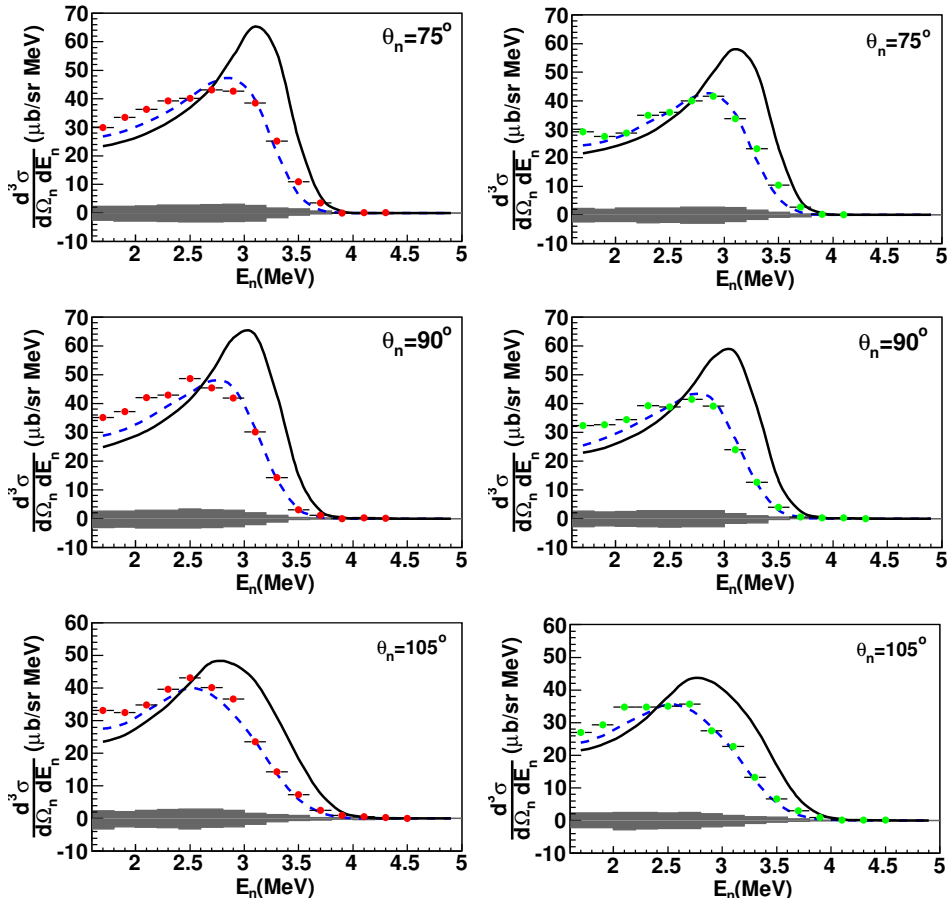

FIGURE B.6: (Color online) Experimental spin-dependent double-differential cross sections for parallel (left panel) and antiparallel (right panel) states as a function of the neutron energy E_n at ν=12.8 MeV compared with the calculations of Deltuva *et al.* (dashed curve) and Skibiński *et al.* (solid curve). The bin width is 0.2 MeV. The band shows the combined systematic uncertainties [203].

The overall shape, magnitude, and location of the neutron peak in the experimental results are described better by the calculations of Deltuva *et al.* Further, studies show that the differences between Deltuva *et al.* and Skibiński *et al.* are dominated by the proton-proton Coulomb force that is included only in the calculations by Deltuva *et al.* with all other ingredients playing a minor role in these differences. Therefore, one can conclude that the inclusion of the proton-proton Coulomb repulsion in the calculations is important for this process.

Fig. B.7 shows the contributions from three-body photodisintegration to the ^{3}He

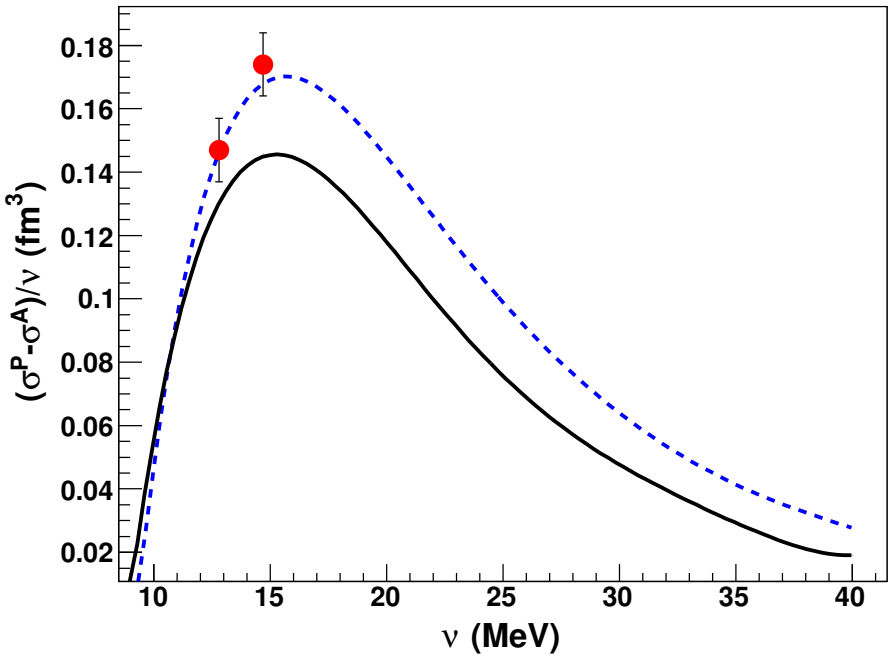

FIGURE B.7: (Color online) GDH integrand results with statistical uncertainties only compared with the theoretical predictions from Deltuva *al.* (dashed curve) and Skibiński *et al.* (solid curve).

GDH integrand together with the predictions based on the calculations of Deltuva *et al.* and Skibiński *et al.* as a function of the incident photon energy. Our data are in very good agreement with predictions of Deltuva *et al.* Both predictions show that the GDH integrand maximizes at 16 MeV and decreases significantly after 40 MeV. As such, extending these measurements to higher photon energies and carrying out measurements on two-body breakup channel will provide crucial tests of the differential cross sections, the energy dependence of the predictions, and whether the contribution to the GDH integral is indeed dominated by the three-body channel below the pion threshold. These measurements, when combined with data above pion threshold from other laboratories, will directly test the ^{3}He GDH sum rule prediction. They will also provide a unique test of how effective a polarized ^{3}He target is a polarized neutron target.

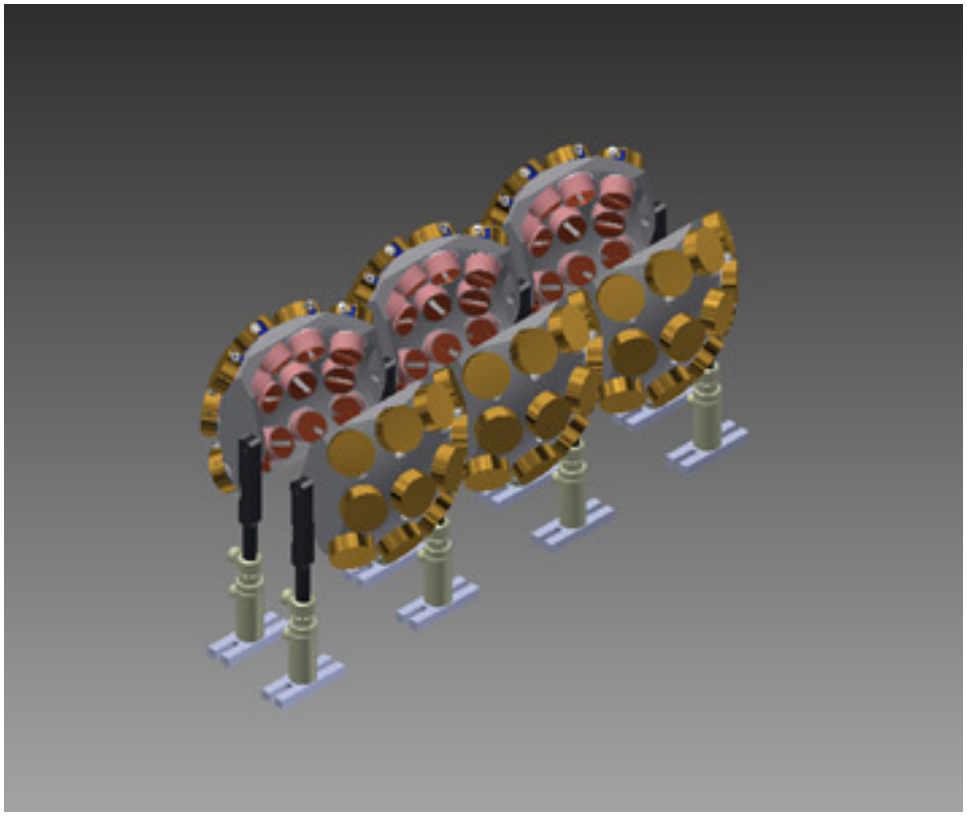

FIGURE B.8: (Color online) The proposed SSB detection system for two-body measurements [204].

B.4 Two body photodisintegration of ^3He

In the following sections, I would like to present the beam test results from the two-body photodisintegration of ^3He. The results were analyzed by G. Laskaris [204].

B.4.1 The Experiment

A cell similar to the ^3He cell used in the three-body breakup experiment will be employed in the two-body experiment. The main difference is that the wall thickness of the chamber will be a uniform 700 μm. The ^3He density of the new cell will be about 4 amg. The protons from the two-body photodisintegration of ^3He are detected by 72 fully depleted Silicon Surface Barrier detectors (SSB). Fig. B.8 shows the schematic of the proposed experimental layout.

B.4.2 Beam test

The beam test was performed in April 2013 at an incident photon energy of 30 MeV with an energy spread of $\Delta E/E \sim 3\%$. The protons from the two-body photodisintegration of unpolarized ^{3}He were detected by sixteen fully depleted Silicon Surface Barrier detectors (SSB). The detectors were positioned at scattering angles of 45 °, 70 °, 95 ° and 120 ° (four detectors at each angle), and ∼11 cm away from the center of the ^{3}He target cell.

The photon flux was monitored using a 5-paddle system that was calibrated using a NaI(Tl) detector. Additionally, a D_2O cell along with two liquid scintillator detectors, positioned downstream of the target served as a second flux monitor. The detectors were placed at 90 ° with respect to the beam axis and counted the neutrons coming from the d(γ,n) and O(γ,n) reactions. The γ-ray beam was collimated using a 12 mm collimator and the photon flux was estimated to be $\sim 3 \times 10^7 \gamma/s$. Fig. B.9 shows the acquired spectra from the April 2013 beam test.

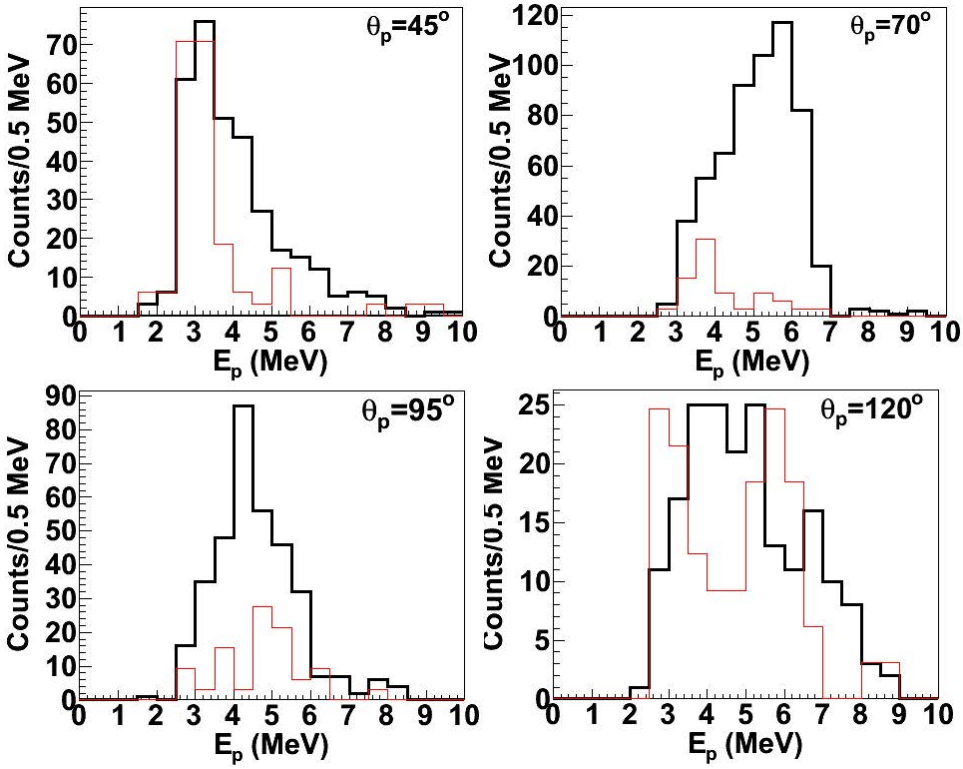

FIGURE B.9: The proton energy spectra from 2-body ^{3}He photodisintegration (black line) in comparison with the reference cell background (red line) normalized to the same integrated flux [204].

Bibliography

[1] Ju-Jun Xie, Bing-Song Zou, and Huan-Ching Chiang. *Phys. Rev. C*, 77:015206, 2008.

[2] M. Alberg. *Prog. Part. Nucl. Phys.*, 36:217, 1996.

[3] Johann Rafelski and Berndt Müller. *Phys. Rev. Lett.*, 48:1066–1069, 1982.

[4] J. Knoll H. W. Barz, B. L. Friman and H. Schul. *Nucl. Phys. A.*, 485:685, 1988.

[5] Particle Data Group. *Phys. Rev. D*, 86:010001, 2012.

[6] S. Okubo. *Phys. Lett. B*, 5:165, 1965.

[7] I.Iizuka. *Prog. Theor. Phys. Suppl*, 21:37, 1966.

[8] G. Zweig. *Cern report no. 8419/th*, page 412, 1996.

[9] S. Okubo. *Phys. Rev. D*, 16:2336, 1977.

[10] M. Gell-Mann. California Institute of Technology Synchrotron Laboratory Report CTSL-20, 1961.

[11] S. Okubo. *Prog. Theor. Phys.*, 27, 1962.

[12] C. Caso et al. *Eur. Phys. J. C*, 3:1, 1998.

[13] Y. Nambu and J.Sakurai. *Phys. Rev. Lett*, 8:79, 1962.

[14] T. Mibe et al. *Phys. Rev. C*, 76:052202r, 2007.

[15] T.-S. H. Lee H. Gao and V. Marinov. *Phys. Rev. C*, 63:022201(R), 2001.

[16] I. A. Schmidt S. J. Brodsky and G. F. de Taramond. *Phys. Rev. Lett*, 64:1011, 1990.

[17] Z.Y. Zhang F. Huang and Y.W. Yu. *Phys. Rev. C*, 73:025207, 2006.

[18] Z.Y. Zhang F. Huang and Y.W. Yu. *Phys. Rev. C*, 71:064001, 2006.

[19] F. Huang and Z.Y. Zhang. *Phys. Rev. C*, 72:068201, 2005.

[20] S. Lisa et al. *Phys. Rev. C*, 75:058201, 2007.

[21] H. J. Behrend et al. *Nucl. Phys. B*, 144:22, 1978.

[22] U. G. Meissner A. Sibirtsev, H.W. Hammer and A.W. Thomas. *Eur. Phys. J. A*, 29:209, 2006.

[23] H. J. Lipkin. *Phys. Rev. Lett*, 16:1015, 1966.

[24] T. Ishikawa et al. *Phys. Lett. B*, 608:215, 2005.

[25] M. Hartmann et al. *Phys. Rev. C*, 85:035206, 2012.

[26] M. H. Wood et al. *Phys. Rev. Lett*, 105:112301, 2010.

[27] K. Nakayama et al. *Phys. Rev. C*, 60:055209, 1999.

[28] P. Muehlich and U. Mosel. *Nucl. Phys. A*, 765:188, 2006.

[29] X. Qian et al. *Phys. Lett. B*, 680:417, 2009.

[30] L. Roca V. K. Magas and E. Oset. *Phys. Rev. C*, 71:065202, 2005.

[31] E. Ya. Paryev. *J. Phys. G*, 36:015103, 2009.

[32] H. Schade. University of Dresden, PhD thesis, 2010.

[33] C. Hanhart. *Phys. Rept.*, 397:155, 2004.

[34] P. Moskal et al. *Prog. Part. Nucl. Phys*, 49:1, 2002.

[35] H. Machner and J. Haidenbauer. *J. Phys. G*, 25:231, 1999.

[36] K. Tsushima and K. Nakayama. *Phys. Rev. C*, 68:034612, 2003.

[37] S. Barsov et al. *Eur. Phys. J. A*, 31:95, 2007.

[38] H. J. Lipkin. *Phys. Lett. B*, 60:371, 1976.

[39] S. Eidelmann et al. *Phys. Lett. B*, 592:1, 2004.

[40] E. Gabathuler J. Ellis and M. Karliner. *Phys. Lett. B*, 217:173, 1989.

[41] G. Krein E. M. Henley and A. G. Williams. *Phys. Lett. B*, 281:178, 1992.

[42] C. Amsler et al. *Rev. Mod. Phys.*, 70:1293, 1998.

[43] U. G. Meissner et al. *Phys. Lett. B*, 408:381, 1997.

[44] M. P. Locher and Yang Lu. *Z. Phys. A*, 351:83, 1995.

[45] R. Wurzinger et al. *Phys. Rev. C*, 51:443, 1995.

[46] R. Wurzinger et al. *Phys. Lett. B*, 374:283, 1996.

[47] F. Balestra et al. *Phys. Rev. C*, 63:024004, 2001.

[48] M. Hartmann et al. *Phys. Rev. Lett.*, 96:242301, 2006.

[49] A. Ferrer et al. *Phys. Lett. B*, 394:395, 1997.

[50] U. G. Meissner A. Sibirtsev and A.W. Thomas. *Phys. Rev. D*, 71:094001, 2005.

[51] A. Sibirtsev et al. *Eur. Phys. J. A*, 27:269, 2006.

[52] A. Sibirtsev. *Eur. Phys. J. A*, 604:455, 1996.

[53] A. Sibirtsev and W. Cassing. *Eur. Phys. J. A*, 7:407, 2000.

[54] R. Machleidt. *Adv. Nucl. Phys.*, 19:189, 1989.

[55] B. Kaṁpfer A .I .Titov and V. V. Shklyar. *Phys. Rev. C*, 59:2, 1998.

[56] D. E. Kharzeev J. Ellis, M. Karliner and M.G. Sapozhnikov. *Nucl. Phys. A*, 673:256, 2000.

[57] J. Arvieux M. P. Rekalo and E. T. Gustafsson. *Z. Phys. A*, 357:133, 1997.

[58] A. Faessler et al. *Phys. Rev. C*, 70:035211, 2004.

[59] A. Svarc M. Batinic and T.S.H. Lee. *Physica Scripta*, 56:321, 1997.

[60] A. Moalem G. Gedalin and L. Razdolskaja. *Nucl. Phys. A*, 634:368, 1998.

[61] M. GellMann and K.M. Watson. *Ann. Rev. Nucl. Sci.*, 4:219, 1954.

[62] Y. Maeda. private communication.

[63] Y. Maeda et al. *Phys. Rev. C*, 77:015204, 2008.

[64] S. Abd El-Samad et al. *Phys. Lett. B*, 688:142, 2010.

[65] W. Oelert. *Proceedings of the Workshop on Meson Production, Interaction and Decay, Cracow*, page 199, 1991.

[66] T. Yao. *Phys. Rev.*, 125:1048, 1962.

[67] D. Morgan and M. R. Pennington. *Phys. Rev. D*, 48:1185, 1993.

[68] J. Smyrski. Report IFJ No 1808/PH, 1998.

[69] R. L. Jaffe. *Phys. Rev. D*, 15:267, 1977.

[70] D. Morgan K. L. Au and M. Pennington. *Phys. Rev. D*, 35:1633, 1987.

[71] E. Van Beveren et al. *Z. Phys. C*, 30:615, 1986.

[72] J. D. Weinstein and N. Isgur. *Phys. Rev. D*, 41:2236, 1990.

[73] D. Lohse et al. *Nucl. Phys. A*, 516:513, 1990.

[74] P. B. Siegel N. Kaiser and W. Weise. *Nucl. Phys. A*, 594:325, 1995.

[75] J. D. Davies et al. *Phys. Lett. B*, 83:55, 1979.

[76] M. Izycki et al. *Z. Phys. A*, 297:11, 1980.

[77] P. M. Bird et al. *Nucl. Phys. A*, 404:482, 1983.

[78] T. M. Ito et al. *Phys. Rev. C*, 58:2366, 1998.

[79] C. Guaraldo et al. *Eur. Phys. J. A*, 19:185, 2004.

[80] G. Beer et al. *Phys. Rev. Lett.*, 94:212302, 2005.

[81] A. Rusetsky U. G. Meissner, U. Raha. *Eur. Phys. J. C*, 35:349, 2004.

[82] U. G. Meissner B. Borasoy and R. Nibler. *Phys. Rev. C*, 74:055201, 2006.

[83] P. Winter et al. *Phys. Lett. B*, 635:23, 2006.

[84] C. H. Lee G. Q. Li and G. E. Brown. *Nucl. Phys. A*, 625:372, 1997.

[85] P. Senger. *Prog. Part. Nucl. Phys.*, 42:209, 1999.

[86] P. Senger et al. *Phys. Rev. C*, 75:024906, 2007.

[87] F. Laue et al. *Phys. Rev. Lett*, 82:1640, 1999.

[88] R. Barth et al. *Phys. Rev. Lett*, 78:4007, 1997.

[89] M. Menzel et al. *Phys. Lett B*, 495:26, 2000.

[90] W. Oelert. *Nucl.Phys. A*, 639:13, 1998.

[91] S. Nagamiya. *Nucl. Phys. A*, 544:5, 1992.

[92] E. L. Bratkovskaya et al. *Eur. Phys. J. A*, 4:165, 1999.

[93] W. M. Yao et al. *J. Phys. G*, 33:1, 2006.

[94] W. Cassing A. Sibirtsev and C. M. Ko. *Z. Phys. A*, 358:101, 1997.

[95] A. Baldini et al. Total cross-sections for reactions of high-energy particles, Vol. I/12 of LandoltBornstein, New Series, Springer, Berlin, 1988.

[96] A. Dzyuba et al. *Phys. Lett. B*, 668:315, 2008.

[97] T. H. Tan. *Phys. Rev. Lett.*, 23:395, 1969.

[98] R. H. Dalitz and S. F. Tuan. *Ann. Phys.*, 10:307, 1960.

[99] Ju-Jun Xie and Colin Wilkin. *Phys. Rev. C*, 82:025210, 2010.

[100] M. L. Goldberger and K. M. Watson. *Collision Theory.* John Wiley and Sons, New York, 1964.

[101] N. Kaiser V. Bernard and U. G. Meissner. *Eur. Phys. J. A*, 4:259, 1999.

[102] Y. Maeda et al. *Phys. Rev. Lett.*, 97:142301, 2006.

[103] M. Silarski et al. *Phys. Rev. C*, 80:045202, 2009.

[104] M. Wolke. Dissertayion, Westfa̤lische Wilhelms-Universita̤t Mu̇ister, Germany, 1998.

[105] C. Quentmeier et al. *Phys. Lett. B*, 515:276, 2001.

[106] T. Hyodo and W. Weise. *Phys. Rev. C*, 77:044005, 2008.

[107] C. Fuchs. *Prog. Part. Nucl. Phys*, 56, 2006.

[108] Y. Akaishi and T. Yamazaki. *Phys. Rev. C*, 65:044005, 2002.

[109] T. Yamazaki and Y. Akaishi. *Phys. Rev. Lett*, 98:082301, 2007.

[110] Y. Ikeda and T. Sato. *Phys. Rev. C*, 76:035203, 2007.

[111] A. Gal N. V. Shevchenko and J. Mares. *Phys. Rev. C*, 76:044004, 2007.

[112] H. Kamano Y. Ikeda and T. Sato. *Progr. Theoret. Phys.*, 124:53339, 2010.

[113] T. Hyodo T. Uchino and M. Oka. *Nucl. Phys. A*, 868:53, 2011.

[114] T. Hyodo A. Dote and W. Weise. *Phys. Rev. C*, 79:014003, 2009.

[115] T. Yamazaki and Y. Akaishi. *Phys. Lett. B, volume = 535, pages = 70, year = 2002.*

[116] L. Fabbietti et al. *Nucl. Phys. A*, 914:60, 2013.

[117] J. Marton A. N. Ivanov, P. Kienle and J. Widmann. arXiv:nucl-th/0512037v2, 2008.

[118] J. M. Laget. *Phys. Lett. B.*, 259:24, 1991.

[119] E. Ferrari. *Phys. Rev.*, 120:988, 1960.

[120] J. Q. Wu and C. M. Ko. *Nucl. Phys. A*, 499:810, 1989.

[121] S. W. Huang K. Tsushima and A. Faessler. *Phys. Lett. B*, 337:245, 1994.

[122] A. Sibirtsev. *Phys. Lett. B*, 359:29, 1995.

[123] A. Sibirtsev K. Tsushima and A. W. Thomas. *Phys. Lett. B*, 390:29, 1997.

[124] G. Fäldt and C. Wilkin. *Z. Phys. A*, 357:241, 1997.

[125] K. Tsushima A. Sibirtsev and A. W. Thomas. *Phys. Lett. B*, 421:59, 1998.

[126] R. Shyam. *Phys. Rev. C*, 60:055213, 1999.

[127] K. Holinde A. Reuber and J. Speth. *Nucl. Phys. A*, 570:543, 1994.

[128] M. Agnello et al. *Phys. Rev. Lett.*, 94:212303, 2005.

[129] T. Yamazaki et al. *Phys. Rev. Lett.*, 104:132502, 2010.

[130] A. O. Tokiyasu et al. arXiv:1306.5320v1, 2013.

[131] V. K. Magas et al. *Phys. Rev. C*, 74:025206, 2006.

[132] S. Barsov et al. *Nucl. Instr. and Meth. A*, 462:364, 2001.

[133] R. Maier et al. *Nucl. Instr. and Meth. A*, 390:1, 1997.

[134] S. Brauksiepe et al. *Nucl. Instr. and Meth.*, 376:397, 1996.

[135] M. Hartmann. IKP annual report, 2002.

[136] R. Bilger et al. *Phys. Lett. B*, 420:217, 1998.

[137] M. Büscher et al. *Eur. Phys. J. A*, 22:301, 2004.

[138] S. Dymov et al. *Part. Nucl. Lett.*, 119:40, 2004.

[139] A. Khoukaz et al. *Eur. Phys. J. D*, 5:275, 1999.

[140] R. Schleichert. Ph.D. Thesis, Technische Hochschule Aachen, Germany, 1996.

[141] W. Erven et al. *IEEE Trans. Nucl. Sci. NS-45*, page 852, 1998.

[142] P. Wstner M. Drochner, W. Erven and K. Zwoll. *IEEE Trans. Nucl. Sci. NS-45*, page 1882, 1998.

[143] V. Hejny et al. IKP Annual Report, 2002.

[144] R. Brun et al. http://root.cern.ch/root, 2003.

[145] M. Büscher et al. *Eur. Phys. J. A*, 22:301, 2004.

[146] V. Kleber. Ph.D. Thesis, University of Kol̈n, Germany, 2003.

[147] S. Agostinelli et al. *Nucl. Instr. and Meth.*, 506:250, 2003.

[148] W. J. Briscoe R. A. Arndt and R. L. Workman. *Phys. Rev. C*, 62:034005, 2000.

[149] I. I. Strakovsky R. A. Arndt, W. J. Briscoe and R. L. Workman. *ibid*, 76:025209, 2007.

[150] R. L. Workman R. A. Arndt, W. J. Briscoe and I. I. Strakovsky. http://gwdac.phys.gwu.edu.

[151] R.D. Albers et al. *Eur. Phys. J. A*, 22:125, 2007.

[152] R. C. Kammerud et al. *Phys. Rev. D*, 4:1309, 1971.

[153] S. A. Azimov et al. *Sov. Phys. JETP*, 15:299, 1962.

[154] I. Ambats et al. *Phys. Rev. D*, 9:1179, 1974.

[155] T. Fujii et al. *Phys. Rev.*, 128:1836, 1962.

[156] R. Wilson W. M. Preston and J. C. Street. *ibid*, 118:579, 1960.

[157] R. A. Arndt. private communication.

[158] H. J. Stein et al. *Phys. Rev. St-AB*, 11:052801, 2008.

[159] Y. Valdau. Ph.D. Thesis, Forschungszentrum Jul̈ich, Germany, 2009.

[160] A. Mussgiller. IKP Annual Report, 2004.

[161] U. G. Meissner B. Borasoy and R. Nibler. *Phys. Rev. C*, 74:055201, 2006.

[162] I. Frohlich. Pos A CAT2007, 2007.

[163] A. Sarantsev D.V. Bugg, V.V. Anisovich and B.S. Zou. *Phys. Rev. D*, 50:4412, 1994.

[164] S. Teige et al. *Phys. Rev. D*, 59:012001, 1999.

[165] A.N. Kiselev N.N. Achasov. *Phys. Rev. D*, 68:014006, 2003.

[166] A. Antonelli. *hep-ex/0209069*, 2002.

[167] M. N. Achasov et al. *Phys. Lett. B*, 485:349, 2000.

[168] R. R. Akhmetshin et al. *Phys. Lett. B*, 462:380, 1999.

[169] R. Kaminski and L. Lesniak. *Phys. Rev. C*, 51:2264, 1995.

[170] M. Ablikim et al. *Phys. Lett. B*, 607:243, 2005.

[171] K. Nakamura et al. *J. Phys. G*, 37:075021, 2010.

[172] F. James and M. Roos. *Comput. Phys. Commun.*, 10:343, 1975.

[173] V. V. Sarantsev et al. *Eur. Phys. J. A*, 43:11, 2010.

[174] A. V. Anisovich et al. *Eur. Phys. J. A*, 34:129, 2007.

[175] G. Agakichiev et al. *Phys. Rev. C*, 85:035203, 2012.

[176] Y. Maeda et al. *Phys. Rev. C*, 79:018201, 2009.

[177] Q. J. Ye et al. *Phys. Rev. C*, 85:035211, 2012.

[178] C. Wilkin. *Acta Phys. Polon. Suppl.*, 89:2, 2009.

[179] U. G. Meissner B. Borasoy and R. Nibler. *Phys. Rev. C*, 74:055201, 2006.

[180] J. K. Kim. *Phys. Rev. Lett.*, 14:29, 1965.

[181] A. D. Martin. *Nucl. Phys. B*, 179:33, 1981.

[182] L. P. Kaptari and B. KAm̈pfer. *Eur. Phys. J. A*, 23:291, 2005.

[183] Q. J. Ye et al. *Phys. Rev. C*, 87:065203, 2013.

[184] S. Flatte. *Phys. Lett. B*, 63:224, 1976.

[185] M. Iwasaki et al. *Phys. Rev. Lett.*, 78:3067, 1997.

[186] M. Bazzi et al. *Phys. Lett. B*, 704:113, 2011.

[187] U. G. Meissner M. Mai. *Nucl. Phys. A*, 900:51, 2013.

[188] H. Petr et al. *Phys. Rev. C*, 82:055206, 2010.

[189] T. Mibe et al. *Phys. Rev. Lett.*, 95:182001, 2005.

[190] B. Dey et al. *Acta Conf. Proc.*, 1388:242, 2011.

[191] G. Fäldt and C. Wilkin. *Phys. Lett. B*, 354:20, 1995.

[192] B. Dey et al. *Phys. Rev. C*, 82:025202, 2010.

[193] S. A. Pereira et al. *Phys. Lett. B*, 688:289, 2010.

[194] H. Kohri et al. *Phys. Rev. Lett.*, 104:172001, 2010.

[195] T. R. Carver M. A. Bouchiat and C. M. Varnum. *Phys. Rev. Lett.*, 5:373, 1960.

[196] W. Happer N. D. Bhaskar and T. McClelland. *Phys. Rev. Lett.*, 49:25, 1982.

[197] W. Happer et al. *Phys. Rev. A*, 29:3092, 1984.

[198] D. Choudhury et al. *Phys. Rev. Lett.*, 98:232303, 2007.

[199] Q. J. Ye. www.phy.duke.edu/∼qy4, 2010.

[200] S. D. Drell and A. Hearn. *Phys. Rev. Lett.*, 16:908, 1966.

[201] S. B. Gerasimov. *Sov. J. Nucl. Phys.*, 1:430, 1966.

[202] X. Yan. Preliminary report, Duke University, 2013.

[203] G. Laskaris et al. *Phys. Rev. Lett.*, 110:202501, 2013.

[204] G. Laskaris. Private Communication, 2013.

Biography

Qiujian Ye was born in Jianou, China in December, 1985.

Education:

- 08.2008 - 12.2013 Ph.D candidate in Nuclear Physics, Duke University, USA
- 09.2004 - 06.2008 B.S. in Applied Physics, University of Science & Technology of China, China

Publication:

- First Measurements of Spin-Dependent Double-Differential Cross Sections and the GDH Integrand from $^3\vec{H}e(\vec{,}n)pp$ at Incident Photon Energies of 12.8 and 14.7 M, G. Laskaris *et al.*, Phys. Rev. Lett. **110**, 202501 (2013).
- Measurement of spin observables in the quasi-free $np \to pp_s pi^-$ reaction at 353 MeV, S. Dymov *et al.*, S. Dymove *et al.*, Phys. Rev. C **88**, 014001 (2013).
- The production of K^+K^- pairs in proton-proton collisions below the ϕ meson threshold, Q. J. Ye *et al.*, Phys. Rev. C **87**, 065203 (2013).
- The production of K^+K^- pairs in proton-proton collisions at 2.83 GeV, Q. J. Ye *et al.*, Phys. Rev. C **85**, 035211 (2012).
- Momentum dependence of the ϕ meson nuclear transparency, M. Hartmann *et al.*, Phys. Rev. C **85**, 035206 (2012).